THESIS

Probing the observational signatures of cosmological phase transitions

(天文観測で探る宇宙論的相転移の歴史の解明に向けて)

Koichiro Horiguchi

Department of Physics, Nagoya university

January 5, 2018

Abstract

In the early universe, a number of cosmological phase transitions are expected to have taken place. These cosmological phase transitions could leave features in the early universe, which are called cosmic defects. These defects are caused by the symmetry breaking and live longer than the time scale of their phase transitions. In this study, we focus on two of them. One is the cosmic string which is a string like high energy region, and the other is the texture which is the self-ordering scalar fields. These defects induce scalar, vector, and tensor mode cosmological perturbations in the universe, and these perturbations produce observational signatures. We expect that we can probe the phase transitions observing such signatures. Here we will see the signatures caused by the vector and tensor perturbations which are not contaminated by the standard cosmological perturbations.

In this study, we will investigate the generation process of the observational signatures of cosmic defects in vector and tensor perturbations according to the four papers [1, 2, 3, 4]. Here we review the generation of the primordial magnetic fields from cosmic strings and textures [1, 2], the primordial gravitational waves from cosmic strings [3] and the gravitational lensing signals from textures [4].

The energy momentum tensors of cosmic strings and textures have anisotropic stresses so that they produce vector and tensor perturbations. In the early universe, the vector-mode perturbation from defects induces the relative velocity between photon and baryon fluids and it leads the generation of primordial magnetic fields, the tensor-mode perturbation from defects generates primordial gravitational waves, and both of vector and tensor perturbations induce weak gravitational lensing effects on the cosmic microwave background fluctuations (CMB lensing) and the shape of galaxies (cosmic shear).

We find that the resulting magnetic fields are $B_{\rm string} \sim 10^{-25}(G\mu/10^{-6})$ Gauss and $B_{\rm texture} \sim 10^{-19}\epsilon_v$ Gauss at about 100Mpc scale for cosmic strings and textures, respectively, where $\epsilon_v^2 = N^{-1}(Gv^2)^2$ is the combined parameter for texture, G is the gravitational constant, N is the number of scalar fields constituting the texture, v is their vacuum expectation value, and μ is the tension of the strings. The strength of gravitational waves from infinite string network is given as $\Omega_{\rm gw}^{\rm string} \sim 10^{-8}(G\mu/10^{-6})^2$ at 10^{-8}Hz. Assuming a CMB ideal lensing observation without instrumental noise, we can obtain an upper limit of ϵ_v as 2.7×10^{-6}.

CONTENTS

Part.I

Introduction

In recent years, various precise observations of the universe enable us to reveal the evolution of the universe. One of the most important observational signatures, which has a stock of information, is the cosmic microwave background (CMB) discovered by [5]. It is the afterglow of the epoch of "big bang", in which the universe was in a very high density and high temperature state. CMB is the black body radiation whose mean temperature and its fluctuation are $T = 2.725\text{K}$ and $\Delta T/T \sim 10^{-5}$, respectively. Because of its high density, we can not see earlier than the CMB epoch. CMB is the oldest observational signature which we can see by elecromagnetic waves.

From a viewpoint of a grand unified theory (GUT) [6, 7], there were many fields in the early universe and they have experienced a number of phase transitions due to decrease of temperature. Observing these phase transitions themselves is difficult because most of them have occurred before the era of CMB and we can not see them by electromagnetic waves. Here we would like to mention the fact that, however, these phase transitions could leave some features called cosmic defects, such as cosmic strings and textures [8]. They can live longer than the time of the phase transition, and it may have more chance to observe the features induced by them than observing the phase transitions themselves. Cosmological features left by defects can be estimated by structures of the universe at present, which can be evaluated by cosmological perturbations. It is interesting that we can probe such high energy phenomena by observing the cosmological signatures in the late universe.

In this thesis, we describe observational signatures of cosmic defects, cosmic strings and texture, according to the cosmological perturbation theory. In part I, we will review the standard cosmology where we introduce cosmological perturbation theory (chapeter 1), and physics of cosmological phase transitions (chapter 2). We will discuss the cosmic defects, especially cosmic strings and textures and their effects on cosmological vector and tensor perturbations. In part II, we represent the generation of magnetic fields from cosmic strings (chapter 4) and textures (chapter 5). In part III, we give accounts of the generation of gravitational waves from the sharp structures called kinks on cosmic strings (chapter 7). In part IV we will see the weak gravitational lensing effects of textures on galaxies shapes (chapter 8) and CMB angular power spectra. Finally, we summarize the each signature in part V. Here we adopt natural units $c = \hbar = k_B = 1$, where c is the light speed, $\hbar$ is the reduced Planck constant and k_B is the Boltzmann constant.

Chapter.1

Standard cosmology

The underlying concept of the standard big bang cosmology is that the universe began as a high density and high temperature region called 'fire ball', and such the universe is expanding until now with decreasing temperature. This concept of expanding universe was suggested by Friedmann and Lemaître independently [9, 10], considering the general relativity (GR) [11] under the condition of the homogeneous and isotropic space. Solving Einstein's field equation, they obtained the solution of the expanding or contracting universe. ¥Hubble found almost all distant galaxies were moving away from us and their recession velocities were proportional to the distances [14]. This observational relation between distance and velocity of galaxies provides a firm basis of expansion of the universe. Moreover, it turns out the expansion is actually accelerating due to recent observations of type-Ia Supernovae [15, 16]. These observational facts strongly support the idea of the globally homogeneous and isotropic expanding universe. According to the concept of the expanding universe, the universe started as a high density and high temperature point in the ancient era [12, 13], and this era is called the 'big bang' era.

On the contrary to homogeneity and isotropy, we can see local inhomogeneity of the universe via local structures in the universe like galaxies clusters and cosmic webs. These local structures are originated from tiny density fluctuations of the early universe which we can see in the cosmic microwave background [17, 18, 19] as temperature fluctuations. These results suggest that the universe is globally homogeneous but it has seed fluctuations for the structure formation. Evolution of these fluctuations is described by the theoretically well established cosmological perturbations. The cosmological perturbation theory can represent not only the structures but also magnetic fields, gravitational waves and so on. Using the cosmological perturbation theory, we can calculate these cosmological signatures directly.

1.1 Evolution of the universe

In this section, we will review the expanding homogeneous and isotropic universe based on the GR. The structure of the spacetime is represented using the world distance ds and the metric $g_{\mu\nu}$ as,

$$ds^2 = g_{\mu\nu}dx^\mu dx^\nu, \tag{1.1.1}$$

where dx^μ is the infinitesimal displacement in four dimensional spacetime and we sum up the indices μ and ν from 0 to 3 (Einstein's notation). Because we consider the homogeneous and isotropic universe, the world distance and the metric can be written as

$$ds^2 = g_{\mu\nu}dx^\mu dx^\nu = -dt^2 + a^2(t)d^2\vec{x} = a^2(\eta)(-d\eta^2 + d^2\vec{x}), \tag{1.1.2}$$

$$= a^2(\eta)\eta_{\mu\nu}dx^\mu dx^\nu, \tag{1.1.3}$$

$$\eta_{\mu\nu} = \begin{pmatrix} -1 & 0 & 0 & 0 \\ 0 & 1 & 0 & 0 \\ 0 & 0 & 1 & 0 \\ 0 & 0 & 0 & 1 \end{pmatrix}, \tag{1.1.4}$$

where t is the physical time, $\eta = \int dt/a(t)$ is the conformal time, a is the scale factor of the universe which represents the homogeneous and isotropic evolution (expansion and contraction) of space, and $\eta_{\mu\nu}$ is the Minkovski metric. The Einstein field equation that denotes the relation between the energy momentum tensor of matters and spacetime is given as,

$$G_{\mu\nu} = R_{\mu\nu} - \frac{1}{2}g_{\mu\nu}R = 8\pi G T_{\mu\nu} - \Lambda g_{\mu\nu}, \tag{1.1.5}$$

where $G_{\mu\nu}$ is the Einstein tensor, $R_{\mu\nu}$ is the Riemann tensor, R is the Ricci scalar, G is the gravitational constant, $T_{\mu\nu}$ is the energy momentum tensor, and Λ is the cosmological constant. Using the metric $g_{\mu\nu}$, the Riemann tensor and Ricci scalar are defined as the following equations,

$$R = R^\mu{}_\mu, \tag{1.1.6}$$

$$R_{\mu\nu} = R^\rho{}_{\mu\rho\nu}, \tag{1.1.7}$$

$$R^\rho{}_{\sigma\mu\nu} = \frac{\partial}{\partial x^\mu}\Gamma^\rho_{\nu\sigma} - \frac{\partial}{\partial x^\nu}\Gamma^\rho_{\mu\sigma} + \Gamma^\rho_{\mu\lambda}\Gamma^\lambda_{\nu\sigma} - \Gamma^\rho_{\nu\lambda}\Gamma^\lambda_{\mu\sigma}, \tag{1.1.8}$$

$$\Gamma^\rho_{\mu\nu} = g^{\rho\lambda}\left(\frac{\partial g_{\lambda\nu}}{\partial x^\mu} + \frac{\partial g_{\mu\lambda}}{\partial x^\nu} - \frac{\partial g_{\mu\nu}}{\partial x^\lambda}\right), \tag{1.1.9}$$

where $\Gamma^{\rho}_{\mu\nu}$ the Christoffel symbol. Assuming the components of the universe to be perfect fluids, we can describe the energy momentum tensor as

$$T^{\mu}_{\ \nu} = \begin{pmatrix} -\rho & 0 & 0 & 0 \\ 0 & P & 0 & 0 \\ 0 & 0 & P & 0 \\ 0 & 0 & 0 & P \end{pmatrix}, \tag{1.1.10}$$

where ρ is the energy density and P is the pressure of the fluids. In case of the homogeneous and isotropic universe described by equations (1.1.2) and (1.1.10) (hereafter we assumed the curvature of the universe K as zero), we can obtain the evolution of the scale factor by calculating (1.1.5) as,

$$\left(\frac{1}{a}\frac{da}{dt}\right)^2 = H^2 = \frac{8\pi G}{3}\rho + \frac{\Lambda}{3}, \tag{1.1.11}$$

$$\frac{1}{a}\frac{d^2a}{dt^2} = -\frac{4\pi G}{3}\left(\rho + 3P - \frac{\Lambda}{4\pi G}\right), \tag{1.1.12}$$

where H is the Hubble parameter. These are simultaneous equations called the Friedmann equations. Here we introduce the other notation for these equations as

$$\mathcal{H}^2 = \frac{8\pi G}{3}\rho a^2 + \frac{\Lambda}{3}a^2, \tag{1.1.13}$$

$$\dot{\mathcal{H}} = -\frac{4\pi G}{3}\left(\rho + 3P - \frac{\Lambda}{4\pi G}\right)a^2, \tag{1.1.14}$$

where $\mathcal{H} = Ha$ is the conformal Hubble parameter, and dot $\dot{}$ represents the conformal time derivative $d/d\eta$.

Here we review the evolution of the universe and the scale factor according to the Friedmann equations (1.1.11) and (1.1.13). In the early universe, at the epoch of inflation, the evolution of the universe is driven by the potential energy of the inflation field and the energy density of the universe can be written as $\rho_{inf} \sim V(\phi) \sim$ constant, where V is the potential of the inflation field ϕ, and we obtain the evolution of the scale factor as $a(t) \propto \exp(\sqrt{8\pi G\rho_{inf}/3}t)$. After the inflation epoch, the inflation field was thermalized and it produced particles. This process is called reheating. After the reheating epoch, the universe had become hot and been filled with relativistic particles. At that epoch (i.e., the radiation dominated epoch), the evolution of energy density of the universe can be written as $\rho_{\rm rad} \propto a^{-4}$, where the a^{-3} is from the expansion of space and the other a^{-1} is from the redshift of frequency of relativistic particles. In this case, we can describe the evolution of the scale factor as $a_{\rm rad} \propto t^{1/2}$ ($\propto \eta$). The temperature of the universe decreases according to expansion of the universe ($T \propto a^{-1}$) and when the temperature became lower than the mass of

massive particles ($m > T$), they could not be relativistic any longer, the massive particles became none-relativistic. Then we can express the energy density of such particles as $\rho_{\rm mat} \propto a^{-3}$. Because $\rho_{mat} \propto a^{-3}$ decreases slower than $\rho_{\rm rad} \propto a^{-4}$, they would dominate the universe later (the matter dominated epoch). In that epoch, the time dependence of scale factor is $a \propto t^{2/3} \propto \eta^2$. Afterward, the decrease of $\rho_{\rm mat}$ is caused by the evolution of the scale factor, and the cosmological constant term in (1.1.11) and (1.1.13) will dominate the universe. Then the expansion law of the universe has an accelerating form ($a \propto \exp(\sqrt{\Lambda/3}t)$) again.

Here we redefine the Friedmann equation using non-dimensional quantities. Let us first define the critical density of the universe,

$$\rho_{\rm crit} \equiv \frac{3H^2}{8\pi G}, \tag{1.1.15}$$

as a unit of energy density. When we consider the standard cosmology called the ΛCDM model, in which the evolution of the universe is almost driven by dark energy and cold dark matter nowadays, we can describe density components in the unit of the critical density as

$$\frac{\rho}{\rho_{\rm crit,0}} = \frac{\rho_{\rm r}}{\rho_{\rm crit,0}} + \frac{\rho_{\rm m}}{\rho_{\rm crit,0}} + \frac{\rho_\Lambda}{\rho_{\rm crit,0}} = \Omega_{\rm r} a^{-4} + \Omega_{\rm m} a^{-3} + \Omega_\Lambda, \tag{1.1.16}$$

where subscript zero $_0$ represents quantities at present time, $\rho_\Lambda = \Lambda/8\pi G$ is the energy density of the dark energy, $\Omega_{\rm r} \equiv \rho_{\rm r,0}/\rho_{\rm crit,0}$, $\Omega_{\rm m} \equiv \rho_{\rm m,0}/\rho_{\rm crit,0}$ and $\Omega_\Lambda \equiv \rho_\Lambda/\rho_{\rm crit,0}$ are density parameters for radiation, matter and dark energy components of the universe, respectively, and they satisfy the relation $\Omega_{\rm r} + \Omega_{\rm m} + \Omega_\Lambda = 1$. Then we can rewrite the Friedmann equation using the density parameters as

$$\mathcal{H}^2 = H_0^2(\Omega_r a^{-2} + \Omega_m a^{-1} + \Omega_\Lambda a^2). \tag{1.1.17}$$

where H_0 is the Hubble parameter at present time. One can see that the ratio of each parameter decides when each epoch starts. The matter dominated epoch starts at the matter-radiation equality time $a_{\rm mr} = \Omega_{\rm r}/\Omega_{\rm m}$, and the dark energy dominated epoch starts at dark energy-matter equality time $a_{\rm d} = (\Omega_{\rm m}/\Omega_\Lambda)^{1/3}$. Thanks to precise cosmological observations in recent years [20], these cosmological parameters are determined as $H_0 \sim 70$[km/s/Mpc], $\Omega_m \sim 0.3$, $\Omega_m/\Omega_r \sim 3000$, and $\Omega_\Lambda \sim 0.7$. Let us review the history of the universe with these parameters. Here we define the another notation of the scale factor namely redshift using the elongation of electromagnetic waves due to cosmic expansion. We can denote the elongation of the wavelength as

$$\frac{\lambda_{\rm obs}}{\lambda_{\rm emit}} = \frac{a_{\rm obs}}{a_{\rm emit}} \equiv 1 + z \tag{1.1.18}$$

where $\lambda_{\rm obs}$ is the observed wavelength, $\lambda_{\rm emit}$ is the emitted wavelength, $a_{\rm obs} = a_0$ is the scale factor at observation time (here we assume present time), $a_{\rm emit}$ is the scale factor at emission time and z is called redshift which represents the extension of wavelength. We can see the radiation dominated epoch continues until matter-radiation equality at redshift about $z_{\rm m} = a_{\rm mr}^{-1} - 1 = \Omega_{\rm m}/\Omega_{\rm r} - 1 \sim 3000$. After that, the matter dominated epoch starts and it lasts until the epoch when dark energy density coinside with that of matter density, at redshift about $z = a_{\rm d}^{-1} - 1 = (\Omega_\Lambda/\Omega_{\rm m})^{1/3} - 1 \sim 0.3$. Then dark energy dominated epoch starts and now the universe is driven by dark energy.

Finally we introduce the baryonic component. We divide the matter component into two terms,

$$\Omega_m = \Omega_c + \Omega_b, \tag{1.1.19}$$

where Ω_c is the contribution from cold dark matter which interacts only via gravity, and Ω_b is the contribution from usual matter. As long as we consider the evolution of the universe as a whole, we do not need to consider individual components. However, if we need to treat perturbations from the homogeneous and isotropic universe to handle structure formation, the difference between cold dark matter and baryon becomes significant due to the electromagnetic interactions of the baryonic components.

1.2 Cosmological perturbation theory

In this section, we review the cosmological perturbation theory according to the Einstein equation (1.1.5). We consider the metric perturbations in the universe with the isotropic and homogeneous background. We decompose the perturbations into three independent modes, i.e., scalar, vector, tensor mode [21, 22, 23]. In this thesis, we focus on vector and tensor modes in particular, because these modes have only decaying solutions in the standard cosmology, and they are useful to see the effects of external sources like cosmic defects on metric perturbations.

We define the metric perturbation as,

$$g_{\mu\nu}dx^\mu dx^\nu = a^2(\eta)(-d\eta^2 + (\delta_{ij} + h_{ij})dx^i dx^j), \tag{1.2.20}$$

in the synchronous gauge, where h_{ij} is the metric perturbation. Here we decompose h_{ij} into a trace part $h = h^i{}_i$ and three traceless parts $h_{ij}^{\parallel}$, $h_{ij}^{\perp}$ and h_{ij}^{T} in Fourier space as

$$h_{ij} = \frac{h}{3}\delta_{ij} + h_{ij}^{\parallel} + h_{ij}^{\perp} + h_{ij}^{T}, \tag{1.2.21}$$

where

$$\epsilon^{ijk}k_i k_j h^{\parallel}_{kl} = 0,\ k_i k_j h^{\perp}_{ij} = 0,\ k_i h^{T}_{ij} = 0, \tag{1.2.22}$$

k_i is wavenumber vector and ϵ^{ijk} is the Levi-Civita tensor. Here we can denote these terms using the projection functions $\mathcal{O}(\hat{k})$. At first, we rewrite the parallel mode $h^{\parallel}_{ij}$ as

$$h^{\parallel}_{ij} = \mathcal{O}^{(0)}_{ij}(\hat{k})h^S, \quad \mathcal{O}^{(0)}_{ij}(\hat{k}) = \sqrt{\frac{3}{2}}\left(\hat{k}_i\hat{k}_j - \frac{\delta_{ij}}{3}\right) \tag{1.2.23}$$

where h^S is the scalar perturbation, $\mathcal{O}^{(0)}_{ij}(\hat{k})$ is the projection to the scalar mode and $\hat{k}_i$ is the unit wavenumber vector. Next we decompose $h^{\perp}_{ij}$ as

$$h^{\perp}_{ij} = \frac{i\hat{k}_i h_j + i\hat{k}_j h_i}{\sqrt{2}}, \tag{1.2.24}$$

where h_i is a divergenceless vector. Using the vector basis,

$$\hat{e}^{(\pm 1)}(\hat{k}) = \frac{(\hat{e}_1(\hat{k}) \pm i\hat{e}_2(\hat{k}))}{\sqrt{2}}, \tag{1.2.25}$$

where $\hat{k}\cdot\hat{e}_1(\hat{k}) = \hat{k}\cdot\hat{e}_2(\hat{k}) = \hat{e}_1(\hat{k})\cdot\hat{e}_2(\hat{k}) = 0,\ \hat{e}_1(\hat{k})\cdot\hat{e}_1(\hat{k}) = \hat{e}_2(\hat{k})\cdot\hat{e}_2(\hat{k}) = 1$ and $k_i\hat{e}^{\pm}_i(\hat{k}) = 0$, we can represent h_i as

$$h_i = \sum_{\lambda=\pm 1} \lambda h^{(\lambda)}_V e^{(\lambda)}_i(\hat{k}). \tag{1.2.26}$$

From equations (1.2.24) and (1.2.26), we can obtain $h^{\perp}_{ij}$ directly as

$$h^{\perp}_{ij} = \sum_{\lambda=\pm 1} h^{(\lambda)}_V \mathcal{O}^{(\lambda)}_{ij}(\hat{k}), \qquad \mathcal{O}^{(\lambda)}_{ij}(\hat{k}) = \frac{i\lambda}{\sqrt{2}}(\hat{k}_i\hat{e}^{(\lambda)}_j(\hat{k}) + \hat{k}_j\hat{e}^{(\lambda)}_i(\hat{k})), \tag{1.2.27}$$

where $h^{(\lambda)}_V$ is the amplitude of the vector perturbation. In the same way as the vector mode, using the tensor basis (polarization tensor),

$$\hat{e}^{\pm 2}_{ij}(\hat{k}) = \hat{e}^{\pm}_i(\hat{k})\hat{e}^{\pm}_j(\hat{k}), \tag{1.2.28}$$

we can denote the tensor mode h^T_{ij} directly as

$$h^T_{ij} = \sum_{\sigma=\pm 2} h^{(\sigma)}_T \mathcal{O}^{(\sigma)}_{ij}(\hat{k}), \qquad \mathcal{O}^{(\sigma)}_{ij}(\hat{k}) = \hat{e}^{\pm 2}_{ij}(\hat{k}), \tag{1.2.29}$$

where h_T is the amplitude of tensor perturbation. Here scalar mode perturbations h and h^S correspond to scalar quantities such as gravitational potential, vector mode perturbations $h^{(\lambda)}_V$ represent vector quantities such as vorticity or vector fields, and tensor mode perturbations $h^{(\sigma)}_T$ are equivalent to gravitational waves. Multiplying

$\mathcal{O}^{(0)}_{ij}$, $\mathcal{O}^{(\lambda)}_{ij}$ or $\mathcal{O}^{(\sigma)}_{ij}$ in eqs.(1.2.23), (1.2.27) and (1.2.29) by the metric perturbation h_{ij}, we can obtain each perturbation as

$$\mathcal{O}^{(0)}_{ij}(\hat{k})h_{ij} = h^S, \quad \mathcal{O}^{(\lambda)}_{ij}(\hat{k})h_{ij} = h_V^{(-\lambda)}, \quad \mathcal{O}^{(\sigma)}_{ij}(\hat{k})h_{ij} = h_T^{(-\sigma)}. \tag{1.2.30}$$

Note that these projections are orthonormal each other,

$$\mathcal{O}^{(0)}_{ij}(\hat{k})\mathcal{O}^{(\lambda)}_{ij}(\hat{k}) = \mathcal{O}^{(\lambda)}_{ij}(\hat{k})\mathcal{O}^{(\sigma)}_{ij}(\hat{k}) = \mathcal{O}^{(\sigma)}_{ij}(\hat{k})\mathcal{O}^{(0)}_{ij}(\hat{k}) = 0, \tag{1.2.31}$$

and we defined them as a normalized system,

$$\mathcal{O}^{(0)}_{ij}(\hat{k})\mathcal{O}^{(0)}_{ij}(\hat{k}) = \mathcal{O}^{(\lambda)}_{ij}(\hat{k})\mathcal{O}^{(-\lambda)}_{ij}(\hat{k}) = \mathcal{O}^{(\sigma)}_{ij}(\hat{k})\mathcal{O}^{(-\sigma)}_{ij}(\hat{k}) = 1. \tag{1.2.32}$$

Now we can see scalar, vector, tensor mode are independent from each other and this decomposition is called the scalar vector tensor (SVT) decomposition. Hereafter, we will focus on vector and tensor modes perturbations, and we will see their evolutions briefly.

Substituting eq.(1.2.20) into eq.(1.1.5), we obtain the equation of motion for the scale factor a as eq.(1.1.11) in the zero-th (background) order, and decomposing vector and tensor modes, we obtain the equations of motions for each mode in first (linear) order approximation as,

$$\dot{\sigma}_V + 2\mathcal{H}\sigma_V = 8\pi G\Pi_V/k, \tag{1.2.33}$$

$$\ddot{h}_T + 2\mathcal{H}\dot{h} + k^2 h = 16\pi G\Pi_T, \tag{1.2.34}$$

where $\sigma_V = \sigma_V^{(\lambda)} = \dot{h}_V^{(\lambda)}/k$ is the vorticity, $\Pi_V = \Pi_V^{(\lambda)} = \mathcal{O}^{(\lambda)}_{ij}T_{ij}$ is the anisotropic stress in vector mode, and $\Pi_T = \Pi_T^{(\sigma)} = T_{ij}\mathcal{O}^{(\sigma)}_{ij}$ is the anisotropic stress in tensor mode. Here we omit subscripts λ and σ for simplicity because of independency of each mode shown in eq.(1.2.31). In other words individual modes do not mix in first order perturbations.

In the standard cosmological perturbation theory, the vector and tensor modes anisotropic stress Π_V, Π_T do not appear at cosmological scales, because all (perturbed) source terms induced by the energy momentum tensor $T_{\mu\nu}$ at cosmological scale are originated in the density perturbation $\delta\rho$ and it can only induce scalar modes. In such a situation, the equations of motions for vector and tensor modes, eqs.(1.2.33) and (1.2.34) have only free streaming solutions and only propagate the initial values. Then solving eq.(1.2.33) assuming $\Pi_V = 0$, we obtain the vorticity σ_V as a decreasing function,

$$\sigma_V = \sigma_{V0}(\vec{k})a^{-2} \tag{1.2.35}$$

where $\sigma_{V0}(\vec{k})$ is the initial value of vorticity. In the same way, we consider the case of tensor mode assuming $\Pi_T = 0$. We can solve (1.2.34) as

$$h_T(\vec{k},\eta) = \frac{k\eta}{a(\eta)}\left(h_1(\vec{k})j_{\nu-1}(k\eta) + h_2(\vec{k})n_{\nu-1}(k\eta)\right) \to h_{\rm ini}(\vec{k})\frac{k\eta}{a(\eta)}j_{\nu-1}(k\eta), \quad (1.2.36)$$

where ν is the power law index of conformal time at that time,

$$\nu \equiv \frac{d\ln a}{d\ln \eta}. \quad (1.2.37)$$

$\nu_{\rm rad} = 1$ and $\nu_{\rm mat} = 2$ are the indices at the radiation and matter dominated epochs, respectively, $j_\nu(x)$ is the spherical Bessel function, $n_\nu(x)$ is the spherical Neumann function, $h_1(= h_{\rm ini})$ and h_2 are the arbitrary functions corresponding to initial conditions. Here we assume there is no divergence at $\eta = 0$ and we adopt only the spherical Bessel term. These modes are only propagating initial values and they are decreasing functions in time.

The above discussion is true only when we assume both the first order cosmological perturbation theory and the energy momentum tensor from the standard matters. When we consider the second order perturbation terms or external sources, vector and tensor modes arise. In the case of the second order perturbations, coupling of scalar-mode perturbations (second order terms) can induce vector or tensor mode. In the case of external sources, vector and tensor modes are produced by kinetic terms or other contributions. Here let us show a case of an external source which is originated from a scalar field, for example. The energy momentum tensor of a scalar field can be written as

$$T^\phi_{\mu\nu} = \nabla_\mu\phi\nabla_\nu\phi^* - g_{\mu\nu}\left(\frac{1}{2}\nabla_\alpha\phi\nabla^\alpha\phi^* + V(\phi)\right), \quad (1.2.38)$$

and in Fourier space as

$$\begin{aligned} T^\phi_{ij}(\vec{k}) = &\int d^3q\ q_i(q_j - k_j)\tilde{\phi}(q,\eta)\tilde{\phi}(|\vec{q}-\vec{k}|,\eta)\phi_{\rm ini}(\vec{q})\phi_{\rm ini}(\vec{q}-\vec{k}) \\ &-\frac{1}{2}g_{ij}\int d^3q\ q_\alpha(q^\alpha - k^\alpha)\tilde{\phi}(q,\eta)\tilde{\phi}(|\vec{q}-\vec{k}|,\eta)\phi_{\rm ini}(\vec{q})\phi_{\rm ini}(\vec{q}-\vec{k}) \\ &-\int g_{\mu\nu}V(\phi)e^{-i\vec{k}\cdot\vec{x}}\frac{d^3x}{(2\pi)^3}, \end{aligned} \quad (1.2.39)$$

where $\tilde{\phi}(q,t)$ is the transfer function, and $\phi_{\rm ini}(\vec{q})$ is the initial value of the scalar field. Considering the vector projection,

$$q_i(q_j - k_j)\mathcal{O}^{(\lambda)}_{ij}(\hat{k}) = \frac{\lambda}{2}\sqrt{1-\mu^2}(k - 2q\mu)qe^{-i\psi(\hat{k},\hat{q},\lambda)}, \quad (1.2.40)$$

$$g_{ij}\mathcal{O}_{ij}^{(\lambda)}(\hat{k}) = 0, \tag{1.2.41}$$

where $\mu = \hat{k} \cdot \hat{q} = \cos\theta$, $\hat{q}$ is the unit vector of $\vec{q}$, θ is the angle between $\hat{k}$ and $\hat{q}$, and $\psi(\hat{k}, \hat{q}, \lambda)$ is the angle defined by $\hat{k}$ and $\hat{q}$, we obtain the vector mode anisotropic stress from a scalar field as

$$\begin{aligned}\Pi_V^{(\lambda)} = \frac{\lambda}{2}\int d^3q\ \sqrt{1-\mu^2}(k - 2q\mu)q\tilde{\phi}(q,\eta)\tilde{\phi}(|\vec{q}-\vec{k}|,\eta) \\ \times\phi_{\rm ini}(\vec{q})\phi_{\rm ini}(\vec{q}-\vec{k})e^{-i\psi(\hat{k},\hat{q},\lambda)}.\end{aligned} \tag{1.2.42}$$

Then let us see the tensor mode. We can represent the projections as

$$q_i(q_j - k_j)\mathcal{O}_{ij}^{(\sigma)}(\hat{k}) = \frac{1}{2}(1-\mu^2)q^2 e^{-2i\psi(\hat{k},\hat{q},\sigma)}, \tag{1.2.43}$$

$$g_{ij}\mathcal{O}_{ij}^{(\sigma)}(\hat{k}) = 0, \tag{1.2.44}$$

and therefore the tensor mode anisotropic stress is given as

$$\begin{aligned}\Pi_T^{(\sigma)} = \frac{1}{2}\int d^3q\ (1-\mu^2)q^2\tilde{\phi}(q,\eta)\tilde{\phi}(|\vec{q}-\vec{k}|,\eta) \\ \times\phi_{\rm ini}(\vec{q})\phi_{\rm ini}(\vec{q}-\vec{k})e^{-2i\psi(\hat{k},\hat{q},\sigma)}.\end{aligned} \tag{1.2.45}$$

Now we can see that kinetic terms of a scalar field can produce the vector and tensor modes anisotropic stresses. This means that external sources which have kinetic terms can produce the vector and tensor modes anisotropic stress generally.

Chapter.2

Phase transition and cosmic defects generation

In this chapter, we explain a phase transition of a scalar field due to decreasing temperature of the universe [24, 25, 26, 27] and how defects are configured in the phase transition [8, 28] according to [29]. Here we in particular focus on defects called cosmic strings and textures, and we will discuss their effects on vector and tensor perturbations.

2.1 Phase transition of a scalar field

Phase transitions are phenomena in which fields or particles change their features or states. In case of scalar fields, phase transitions occur due to decrease of temperature of the universe. In the early very hot and dense universe, their mass or vacuum energy were negligible (they were in free states), but now they seem to have mass or vacuum expected values and in stable states (they are in bound states). This means that they have experienced phase transitions. One major indicator of phase transitions is symmetry. Phase transitions which go from free states to bound states correspond to symmetry breaking, and which go from bound states to free states are called symmetry restoration. In case of scalar fields, these phase transitions are characterized by the effective potential of scalar fields. Here we introduce the effective potential of a scalar field and its temperature dependence at first. Next we include a vector field with $U(1)$ (rotation) symmetry in addition to the scalar field, and we confirm that a symmetry breaking of the effective potential and a phase transition of a scalar field could take place. In this section, we consider the homogeneous and

isotropic universe,

$$g_{\mu\nu}dx^\mu dx^\nu = -dt^2 + d\vec{x}^2, \tag{2.1.1}$$

where we ignore the cosmic expansion for simplification.

Effective potential of a scalar field

Here we introduce the physics of a self-ordering scalar field and its fluctuation $\chi(t,\vec{x}) = \bar{\chi}(t) + \phi(t,\vec{x})$. After derivation of the equation of motion of the scalar field χ, we see the effects of fluctuation $\phi(t,\vec{x})$ on the homogeneous component of the scalar field $\bar{\chi}(t)$ by considering quantization of the fluctuation $\phi(t,\vec{x})$ and its thermal effects.

At first, let us consider the Lagrangian density of the self-ordering scalar field χ,

$$\mathcal{L} = -\frac{1}{2}\partial^\mu\chi\partial_\mu\chi - V(\chi), \tag{2.1.2}$$

where $V(\chi)$ is the potential of the scalar field. Taking the variations of the Lagrangian, we obtain the equation of motion of the scalar field as,

$$-\partial^\mu\partial_\mu\chi + V'(\chi) = 0, \tag{2.1.3}$$

where we define derivation of the potential V as $V'(\chi) \equiv \partial V/\partial\chi$. Decomposing the scalar field $\chi(t,\vec{x})$ into the homogeneous part and the inhomogeneous fluctuation, $\chi(t,\vec{x}) = \bar{\chi}(t)+\phi(t,\vec{x})$, and taking ensemble average, we obtain the equation of motion of $\bar{\chi}$ as

$$-\partial^\mu\partial_\mu\bar{\chi} + V'(\bar{\chi}) + \frac{1}{2}V'''(\bar{\chi})\left\langle\phi^2\right\rangle = 0, \tag{2.1.4}$$

where $V'''(\bar{\chi}) \equiv \partial^3 V(\bar{\chi})/\partial\bar{\chi}^3$ and $\left\langle\phi^2\right\rangle$ is the ensemble average of the squared fluctuation of the scalar field. Here we have to take the term $V'''(\bar{\chi})\left\langle\phi^2\right\rangle$ into account when considering the effective potential for the homogeneous scalar field $\bar{\chi}$. Then we need to solve the equation of motion for $\phi(t,\vec{x})$ and estimate the value of $\left\langle\phi^2\right\rangle$. From the first order perturbation of eq.(2.1.3), the equation of motion of the fluctuation $\phi(t,\vec{x})$ is written as,

$$-\partial^\mu\partial_\mu\phi + m_\phi^2(\bar{\chi})\phi = 0, \tag{2.1.5}$$

where we define and assume,

$$m_\phi^2(\bar{\chi}) \equiv V''(\bar{\chi}) = \frac{\partial^2 V}{\partial\bar{\chi}^2} \geq 0, \tag{2.1.6}$$

and the time variation of $m_\phi^2(\bar{\chi})$ is slower than that of ϕ itself. Then the solution of $\phi(t,\vec{x})$ is given by,

$$\phi(t,\vec{x}) = \int \frac{d^3k}{(2\pi)^{3/2}}\frac{1}{\sqrt{2\omega_k}}\left(e^{-i\omega_k t+i\vec{k}\cdot x}a_k^+ + e^{i\omega_k t-i\vec{k}\cdot x}a_k^-\right), \tag{2.1.7}$$

where,

$$\omega_k = \sqrt{k^2 + m_\phi^2(\bar{\chi})}, \tag{2.1.8}$$

is the angular velocity and $a_k^+ = (a_k^-)^*$ is the integration constant. To obtain the ensemble average $\langle\phi^2\rangle$, we quantize the field $\phi(t,\vec{x}) \to \hat{\phi}_x(t)$ and its conjugate momentum $\partial\mathcal{L}/\partial\dot{\hat{\phi}}_x = \partial\phi_x/\partial t \to \partial\hat{\phi}_x/\partial t = \hat{\pi}_x$. Their commutation relation is denoted as,

$$\left[\hat{\phi}_x(t), \hat{\pi}_y(t)\right] = \hat{\phi}_x(t)\hat{\pi}_y(t) - \hat{\pi}_y(t)\hat{\phi}_x(t) = i\delta(\vec{x} - \vec{y}), \tag{2.1.9}$$

where $\hat{\phi}_x(t)$ and $\hat{\pi}_x(t)$ are the operators of the field, and this relation is called the Heisenberg's commutation relation. Then, the integration constants $a_k^+ = (a_k^-)^*$ also become operators as, $a_k^+ \to \hat{a}_k^+$, $a_k^- \to \hat{a}_k^-$, and we obtain their commutation relations as,

$$\left[\hat{a}_k^-(t), \hat{a}_{k'}^+(t)\right] = \delta(\vec{k} - \vec{k}'), \quad \left[\hat{a}_k^-(t), \hat{a}_{k'}^-(t)\right] = \left[\hat{a}_k^+(t), \hat{a}_{k'}^+(t)\right] = 0. \tag{2.1.10}$$

where $\hat{a}_k^+$ and $\hat{a}_k^-$ are called the creation and annihilation operators. These commutation relations correspond to those of a harmonic oscillator, and we can write it in the Hilbert space. First we define the vacuum state as,

$$\hat{a}_k^-(t)\,|0\rangle = 0, \tag{2.1.11}$$

where $|0\rangle$ is the ground (vacuum) state and this state is defined for all wavenumbers k. Then we can denote the n_k particles state as

$$|n_k\rangle = \frac{(\hat{a}_k^+)^{n_k}}{\sqrt{n_k!}}\,|0\rangle\,, \tag{2.1.12}$$

and its average as

$$\left\langle \hat{a}_k^+ \hat{a}_{k'}^- \right\rangle_Q = \frac{\langle n_k|\,\hat{a}_k^+ \hat{a}_{k'}^-\,|n_k\rangle}{\langle n_k|n_k\rangle} = n_k\delta(\vec{k} - \vec{k}'), \tag{2.1.13}$$

$$\left\langle \hat{a}_k^+ \hat{a}_{k'}^+ \right\rangle_Q = \left\langle \hat{a}_k^- \hat{a}_{k'}^- \right\rangle_Q = 0. \tag{2.1.14}$$

Substituting the creation and annihilation operators into (2.1.7) and using the commutation relations eqs.(2.1.13) and (2.1.14), we can calculate the ensemble average of $\langle\phi^2\rangle$ as

$$\langle\phi^2\rangle = \frac{1}{2\pi^2}\int \frac{dk\ k^2}{\omega_k}\left(n_k + \frac{1}{2}\right) = \langle\phi^2\rangle_T + \langle\phi^2\rangle_V\,, \tag{2.1.15}$$

where $\langle\phi^2\rangle_T$ is the thermal contribution from n_k term and $\langle\phi^2\rangle_V$ is the vacuum contribution from the other term. We will see each term below.

Vacuum contribution

The vacuum contribution can be written as [29],

$$\frac{1}{2}V'''(\bar{\chi})\left\langle\phi^2\right\rangle_V = \frac{1}{8\pi^2}\frac{\partial m_\phi^2(\bar{\chi})}{\partial\bar{\chi}}\int^{k_c=M}\frac{dk\ k^2}{\sqrt{k^2+m_\phi^2(\bar{\chi})}} = \frac{\partial V_\phi^{\rm vac}}{\partial\bar{\chi}}, \tag{2.1.16}$$

$$V_\phi^{vac} = \frac{1}{4\pi^2}\int^M dk\ k^2\sqrt{k^2+m_\phi^2(\bar{\chi})} = \frac{I(m_\phi(\bar{\chi}))}{4\pi^2}, \tag{2.1.17}$$

$$I(m) = \frac{1}{8}\left[M(2M^2+m^2)\sqrt{M^2+m^2}+m^4\ln\frac{m}{M+\sqrt{M^2+m^2}}\right] \tag{2.1.18}$$

where we introduce the cutoff scale $k_c = M \gg m_\phi$ to see the characteristics of the vacuum and its divergence. Then we obtain the equation of motion of the averaged field $\bar{\chi}$ using the effective potential $V_{\rm eff}$ as

$$-\partial^\mu\partial_\mu\bar{\chi}+V'_{\rm eff}(\bar{\chi})=0, \tag{2.1.19}$$

where the effective potential $V_{\rm eff}$ including the vacuum contribution $V_\phi^{\rm vac}$ is given by

$$\begin{aligned} V_{\rm eff}(\bar{\chi}) &= V + V_\phi^{\rm vac} \\ &= V + V_\infty + \frac{m_\phi^2}{64\pi^2}\ln\frac{m_\phi^2}{\mu^2}, \end{aligned} \tag{2.1.20}$$

$$V_\infty = \frac{M^4}{16\pi^2}+\frac{M^2}{16\pi^2}m_\phi^2-\frac{m_\phi^4}{32\pi^2}\ln\frac{2M}{e^{1/4}\mu}, \tag{2.1.21}$$

and μ is arbitrary energy scale. Here we assume a simple renormalizable potential V as

$$V=\frac{\lambda_0}{4}\bar{\chi}^4+\frac{m_0^2}{2}\bar{\chi}^2+\Lambda_0, \tag{2.1.22}$$

where $\lambda_0,\ m_0^2$ and Λ_0 are naked constants. Then we can renormalize the effective potential as

$$V_{\rm eff}=\frac{\lambda_R}{4}\bar{\chi}^4+\frac{m_R^2}{2}\bar{\chi}^2+\Lambda_R+\frac{m_\phi^2}{64\pi^2}\ln\frac{m_\phi^2}{\mu^2}, \tag{2.1.23}$$

where we can connect renormalized constants $\lambda_R,\ m_R^2,\ \Lambda_R$ with the naked constants $\lambda_0,\ m_0^2,\ \Lambda_0$ as

$$\frac{\lambda_R}{4}=\frac{\lambda_0}{4}-\frac{9\lambda_0^2}{32\pi^2}\ln\frac{2M}{e^{1/4}\mu} \tag{2.1.24}$$

$$\frac{m_R^2}{2}=\frac{m_0^2}{2}+\frac{3\lambda_0}{16\pi^2}\left(M^2-m_0^2\ln\frac{2M}{e^{1/4}\mu}\right) \tag{2.1.25}$$

$$\Lambda_R=\Lambda_0+\frac{M^4}{16\pi^2}+\frac{M^2m_0^2}{16\pi^2}-\frac{m_0^4}{32\pi^2}\ln\frac{2M}{e^{1/4}\mu}. \tag{2.1.26}$$

These renormalizations enable us to remove divergence of terms including the cutoff scale M.

Thermal contribution

We consider the contribution from the thermal term originated in n_k. Here n_k is the occupancy of excited states and we can represent it by using the Bose-Einstein distribution as

$$n_k = \frac{1}{e^{\omega_k/T} - 1}. \tag{2.1.27}$$

Then, the thermal contribution is given by

$$\frac{1}{2}V'''(\bar{\chi})\left\langle\phi^2\right\rangle_T = \frac{1}{4\pi^2}\frac{\partial m_\phi^2}{\partial\bar{\chi}}\int\frac{dk\ k^2}{\omega_k(e^{\omega_k/T}-1)} = \frac{1}{8\pi^2}\frac{\partial m_\phi^2}{\partial\bar{\chi}}J_-^{(1)}\left(\frac{m_\phi}{T},0\right) \equiv \frac{\partial V^T}{\partial\bar{\chi}} \tag{2.1.28}$$

where

$$J_\pm^{(\nu)}(\alpha,\beta) = \int_\alpha^\infty dx\left(\frac{(x^2-\alpha^2)^{\nu/2}}{e^{x+\beta}\pm 1} + \frac{(x^2-\alpha^2)^{\nu/2}}{e^{x-\beta}\pm 1}\right), \tag{2.1.29}$$

$$V^T(\bar{\chi}) = \frac{T^4}{4\pi^2}\int_0^{m_\phi/T} d\alpha\ \alpha J_-^{(1)}(\alpha,0) = \frac{T^4}{4\pi^2}F\left(\frac{m_\phi}{T}\right). \tag{2.1.30}$$

Putting this thermal contribution into the effective potential (2.1.23), we can describe the whole shape of the effective potential from the fluctuation of the scalar field as

$$\begin{aligned} V_{\text{eff}} &= V + V_\phi^{\text{vac}} + V^T \\ &= \frac{\lambda_R}{4}\bar{\chi}^4 + \frac{m_R^2}{2}\bar{\chi}^2 + \Lambda_R + \frac{m_\phi^2}{64\pi^2}\ln\frac{m_\phi^2}{\mu^2} + \frac{T^4}{4\pi^2}F\left(\frac{m_\phi}{T}\right). \end{aligned} \tag{2.1.31}$$

$U(1)$ model

Here we consider the interaction between a scalar field χ and a $U(1)$ gauge field G_μ, and derive the effective potential for the scalar field. The Lagrangian density of such a model can be written as

$$\mathcal{L} = -\frac{1}{2}\partial^\mu\chi\partial_\mu\chi - V(\chi) + \frac{1}{4}F_{\mu\nu}F^{\mu\nu} - \frac{e^2\chi^2}{2}G_\mu G^\mu, \tag{2.1.32}$$

where

$$F_{\mu\nu} = \partial_\mu G_\nu - \partial_\nu G_\mu, \tag{2.1.33}$$

and e is the coupling constant between the scalar field and the gauge field. We consider the tight coupling case $e^2 \gg \lambda_0$ and ignore the fluctuation of the scalar field. Then the equation of motion for the averaged scalar field is given as

$$-\partial_\mu\partial^\mu\bar{\chi} + V'(\bar{\chi}) + e^2\bar{\chi}\left\langle G_\mu G^\mu\right\rangle = 0. \tag{2.1.34}$$

The feature of the effective potential V_{eff} for the scalar field depends on the ensemble average $\langle G_\mu G^\mu \rangle$. To obtain $\langle G_\mu G^\mu \rangle$, we will investigate the behavior of the gauge field G_μ in the same way as the case of the fluctuation of a scalar field. We describe the equation of motion for G_μ taking variation of the Lagrangian (2.1.32) as,

$$-\partial_\nu \partial^\nu G_\mu + e^2 \bar{\chi}^2 G_\mu = 0, \tag{2.1.35}$$

in the coulomb gauge $\delta^\mu G_\mu = 0$. Treating $e\bar{\chi}$ as $m_G(\bar{\chi})$, the form of the equation of motion is the same as the case of scalar field (2.1.5), and therefore we can represent the contribution of $\langle G_\mu G^\mu \rangle$ by decomposing into the vacuum and thermal contributions as,

$$e^2 \bar{\chi} \langle G_\mu G^\mu \rangle_V = \frac{\partial}{\partial \bar{\chi}} \left(\frac{3I(m_G)}{4\pi^2} \right) = \frac{\partial V_G^{\text{vac}}}{\partial \bar{\chi}}, \tag{2.1.36}$$

$$e^2 \bar{\chi} \langle G_\mu G^\mu \rangle_T = \frac{\partial}{\partial \bar{\chi}} \left(\frac{3T^4}{4\pi^2} F\left(\frac{m_G}{T} \right) \right) = \frac{\partial V_G^T}{\partial \bar{\chi}}, \tag{2.1.37}$$

where the factor of three in front of the potential comes from the degree of freedom of the gauge field G_μ in the coulomb gauge. Now we can calculate the effective potential as,

$$\begin{aligned} V_{\text{eff}} &= V + V_G^{\text{vac}} + V_G^T \\ &= \frac{\lambda_R}{4} \bar{\chi}^4 + \frac{m_R^2}{2} \bar{\chi}^2 + \Lambda_R + \frac{3m_G^2}{64\pi^2} \ln \frac{m_G^2}{\mu^2} + \frac{3T^4}{4\pi^2} F\left(\frac{m_G}{T} \right). \end{aligned} \tag{2.1.38}$$

The condition for phase transitions

To find the condition for phase transitions, we will see the shape of the effective potential at $T = 0$ K. Assuming $\mu = e\chi_0$, we obtain the effective potential at $T = 0$ K as

$$V_{\text{eff}} = \frac{\lambda_R}{4} \bar{\chi}^4 + \frac{m_R^2}{2} \bar{\chi}^2 + \Lambda_R + \frac{3e^4 \bar{\chi}^4}{32\pi^2} \ln \left| \frac{\bar{\chi}}{\chi_0} \right|, \tag{2.1.39}$$

Here we assume that the effective potential has a minimum at $\bar{\chi} = \chi_0,\ V_{\text{eff}}(\chi_0) = 0$, which means $V'_{\text{eff}}(\chi_0) = 0$ and $V''_{\text{eff}}(\chi_0) = m_H^2 > 0$, with m_H being the Higgs mass. Then, using χ_0 and m_H^2, the values of renormalized constants $\lambda_R,\ m_R^2$ and Λ_R can be written as

$$\lambda_R = \frac{m_H^2}{2\chi_0^2} - \frac{9e^4}{32\pi^2}, \tag{2.1.40}$$

$$m_R^2 = -\frac{m_H^2}{2} + \frac{3e^4 \chi_0^2}{16\pi^2}, \tag{2.1.41}$$

$$\Lambda_R = \frac{\chi_0^2}{8} \left(m_H^2 - \frac{e^4 \chi_0^2}{16\pi^2} \right). \tag{2.1.42}$$

We can see that there is a minimum or maximum at $\bar{\chi} = 0$ in this potential eq.(2.1.39). In case $m_H^2 < 3e^4\chi_0^2/8\pi^2$ ($m_R^2 > 0$), the point $\bar{\chi} = 0$ becomes a minimum too, and if in case $m_H^2 < 3e^4\chi_0^2/16\pi^2$ ($\Lambda_R < 0$), the minimum at $\bar{\chi} = 0$ becomes stabler than that of $\bar{\chi} = \chi_0$ ($V_{\rm eff}(0) < V_{\rm eff}(\chi_0)$). This means that the symmetry breaking state at $\bar{\chi} = \chi_0$ is not favored in such a case. If we consider the phase transition caused by the decrease of temperature of the universe, the mean value of $\bar{\chi}$ corresponds to zero (see eq.(2.1.48)) in the early hot universe, and the condition ($V_{\rm eff}(0) > V_{\rm eff}(\chi_0)$) is needed to trigger off the phase transition. Thus the condition of the phase transition is given by

$$m_H^2 > \frac{3e^4\chi_0^2}{16\pi^2}, \tag{2.1.43}$$

and this is called as the Linde-Weinberg condition.

Feature of the effective potential at high temperature

Here we consider the high temperature ($T \gg m_G(\bar{\chi})$) case. In such a situation, the temperature dependent term in eq.(2.1.38), $3T^4F(m_G/T)/4\pi^2$, becomes important. We can expand the function F(x) for $x \ll 1$ as,

$$F(x) \approx \frac{\pi^2}{6}x^2 - \frac{\pi}{3}x^3 - \frac{1}{8}x^4\ln x + \frac{3}{32}x^4 + \frac{x^4}{16}\ln b, \tag{2.1.44}$$

where $\ln b = 2\ln 4\pi - 2\gamma$ and γ is the Euler constant. Then we can describe the effective potential as

$$V_{\rm eff}(\bar{\chi}) = \frac{\lambda_T}{4}\bar{\chi}^4 - \frac{e^3T}{4\pi}\bar{\chi}^3 + \frac{m_T^2}{2}\bar{\chi}^2 + \Lambda_R, \tag{2.1.45}$$

where

$$\lambda_T = \frac{m_H^2}{2\chi_0^2} + \frac{3e^4}{16\pi^2}\ln\frac{bT^2}{(e\chi_0)^2}, \tag{2.1.46}$$

$$m_T^2 = \frac{e^2}{4}(T^2 - T_0^2), \quad T_0^2 = \frac{2m_H^2}{e^2} - \frac{3e^2\chi_0^2}{4\pi^2}. \tag{2.1.47}$$

In enough high temperature, $T \gg T_0$, the effective potential is given by

$$V_{\rm eff}(\bar{\chi}) = \frac{e^2}{8}T^2\bar{\chi}^2, \tag{2.1.48}$$

and the stable point of the scalar field $\bar{\chi}$ becomes symmetric ($\bar{\chi} = 0$).

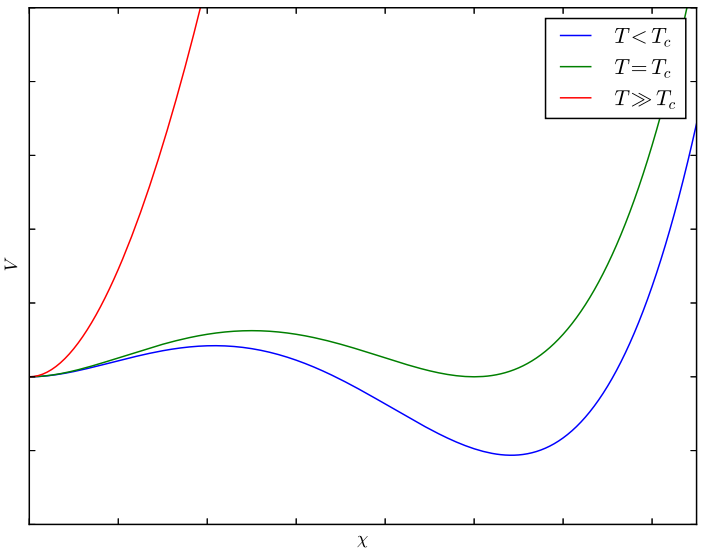

Figure.2.1 The shape of the potential at the temperature $T < T_c$ (blue line), $T = T_c$ (green line) and $T \gg T_c$.

Phase transition of a scalar field

Here we focus on how the shape of the effective potential changes according to the decrease of temperature (i.e. see fig.2.1), and how the scalar field travels in such a potential.

At very high temperature, the shape of effective potential is given by eq.(2.1.48) and the only stable point is $\bar{\chi} = 0$ in such a potential. When the temperature of the universe becomes lower than

$$T_1 = \frac{T_0}{\sqrt{1 - (9e^4/16\pi^2\lambda_{T_1})}}, \tag{2.1.49}$$

the other minimum appears at $\bar{\chi} = 3e^3 T_1/8\pi\lambda_{T_1}$, and that minimum goes to larger value. If the temperature becomes lower than

$$T_c = \frac{T_0}{\sqrt{1 - (e^4/2\pi^2\lambda_{T_c})}}, \tag{2.1.50}$$

where T_c is called the critical temperature, the minimum at $\bar{\chi} \neq 0$ take lower potential value than that of the minimum at $\bar{\chi} = 0$. At that time, the location of the minimum

at $\bar{\chi} \neq 0$ is

$$\bar{\chi}_c = \frac{e^3 T_c}{2\pi \lambda_{T_c}}, \tag{2.1.51}$$

and the potential barrier between the two minima at $\bar{\chi} = \bar{\chi}_c/2$ is given by

$$V_{\text{eff}}(\bar{\chi}_c/2) = \frac{e^{12} T_c^4}{4(4\pi)^4 \lambda_{T_c}^3}. \tag{2.1.52}$$

Then the minimum at $\bar{\chi} = 0$ becomes the false stable minimum and the minimum at $\bar{\chi} \neq 0$ becomes the true stable minimum in the effective potential. This means the stable point goes from $\bar{\chi} = 0$ to $\bar{\chi} \neq 0$ (symmetry breaking) and a phase transition takes place. We represent the typical shape of the potential in fig.2.1.

The way how the phase transition proceeds depends on the relation between the value of the fluctuation of the scalar field and the width of the potential barrier. Substituting the expression of $J_-^{(1)}(\alpha, \beta)$ for $\alpha, \beta \ll 1$,

$$J_-^{(1)}(\alpha, \beta) = \frac{\pi^2}{3} - \frac{1}{2}\beta^2 - \pi\sqrt{\alpha^2 - \beta^2} - \frac{1}{2}\alpha^2 \left(\ln \frac{\alpha}{4\pi} + \gamma - \frac{1}{2} \right) \tag{2.1.53}$$

into eq.(2.1.28), we obtain the magnitude of the fluctuation as

$$\delta\chi \sim \sqrt{\langle \phi^2 \rangle_T} \approx \frac{T}{\sqrt{12}}. \tag{2.1.54}$$

The scalar field in smaller width than $\delta\chi$ (2.1.54) is never localized, and we can recognize whether or not the scalar field feels the potential barrier (2.1.52) by comparing the fluctuation $\delta\chi$ (2.1.54) with the width of the potential $\Delta\chi \sim \bar{\chi}_c/2$ which is about magnitude of the position of the potential exists, $\bar{\chi}_c/2$.
Let us consider the case that the scalar field feels the barrier first. When the temperature is high $T \gg e\bar{\chi}$ and the barrier width $\Delta\chi$ is larger than the fluctuation of the scalar field, the relation between the width of the potential and the critical temperature is written as

$$\frac{T_c}{e} > \frac{\bar{\chi}_c}{2} > \frac{T_c}{\sqrt{12}}. \tag{2.1.55}$$

Adapting it for λ_{T_c}, we obtain

$$\frac{e^4}{4\pi} < \lambda_{T_c} < \frac{\sqrt{3}}{2\pi} e^3. \tag{2.1.56}$$

In this case, the scalar field feels the potential barrier and it needs to go through the potential via the tunnel effect or thermal excitation, to the true minimum. At that time the phase transition is the first order phase transition and it creates bubbles of the true vacuum.

Next let us consider the case that the scalar field does not feel the potential barrier. In that case, the relation between the width of the barrier and fluctuation is given by

$$\frac{\bar{\chi}_c}{2} < \delta\chi \sim \frac{T_c}{\sqrt{12}}. \tag{2.1.57}$$

Considering the condition that the tight coupling is valid, $e^2 \gg \lambda$, we can limit λ_{T_c} as

$$e^2 > \lambda_{T_c} > \frac{\sqrt{3}}{2\pi} e^3. \tag{2.1.58}$$

In this case, the scalar field does not feel the potential barrier and it goes to the true minimum gradually.

2.2 Cosmic defects

The grand unified theory indicates existence of various scalar fields in the early universe [6, 30]. As we saw in previous sections, these scalar fields should have experienced phase transitions as the temperature of the universe decreases and the fields have broken their symmetries. However, in some cases, there are regions in which their symmetries remain restored, and such regions are called 'cosmic defects' [8, 29, 31]. These symmetry restorations take place because of the continuity of scalar fields values in the universe (real space) and in the field space. Hereafter we introduce cosmic defects which originated from symmetry breaking of N scalar fields called $\mathcal{O}(N)$ symmetry breaking and the nature of defects depends on the number of scalar fields N [8]. The produced defects are called 'domain wall' ($N = 1$), 'cosmic string' ($N = 2$), 'monopole' ($N = 3$) and 'texture' ($N \geq 4$).

Here we consider the self-ordering scalar fields whose Lagrangian density is given by

$$\mathcal{L}_\Phi = -\frac{1}{2}\nabla_\mu \Phi^t \nabla_\mu \Phi - \frac{\lambda}{4}(\Phi^t\Phi - v^2)^2 + \mathcal{L}_T, \tag{2.2.59}$$

where $\Phi = (\phi_1, \phi_2, ..., \phi_N)$ is the scalar fields, λ is the coupling constant, v is the vacuum expected value (VEV) of the scalar fields (which corresponds to the energy scale of the phase transition), and $\mathcal{L}_T$ is the thermal contribution which is written as $\mathcal{L}_T \sim -T^2\Phi^t\Phi$ at high temperature. Taking variation of the Lagrangian (2.2.59), we obtain the equation of motion for the self-ordering scalar fields as

$$-\nabla_\mu \nabla^\mu \phi_i + \frac{\partial}{\partial \phi_i} V(\phi, T) = 0, \tag{2.2.60}$$

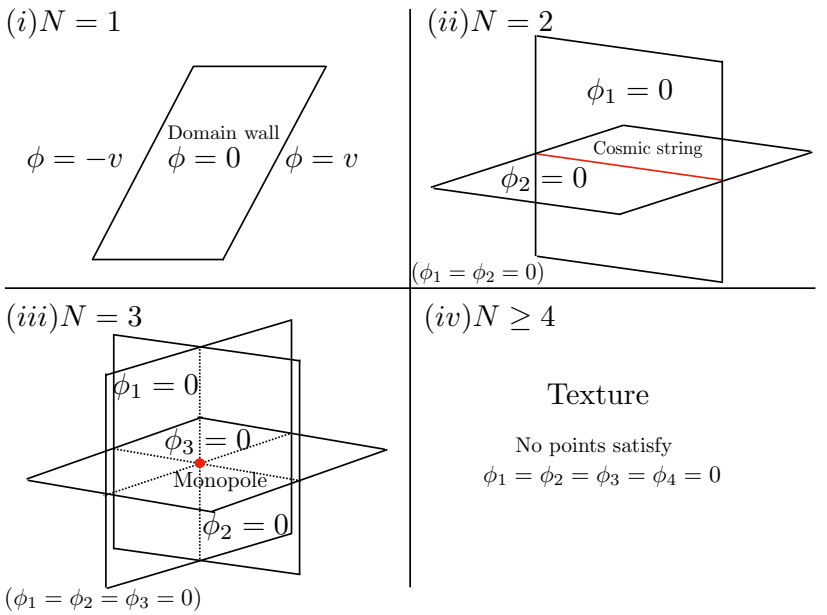

Figure.2.2 Rough illustrations of cosmic defects. There are no high energy regions for the case $N \geq 4$: textures.

where the potential $V(\phi, T)$ is written as

$$V(\phi, T) = \frac{\lambda}{4}(\Phi^t\Phi - v^2)^2 + \alpha T^2 \Phi^t \Phi, \quad (\alpha > 0). \tag{2.2.61}$$

In the early hot universe, the potential is driven by the thermal term $\alpha T^2 \Phi^t \Phi$ and the only stable minimum is located at $\Phi^t\Phi = 0$. After temperature has become lower than the critical temperature T_c, the other stable minima appear. The shapes or minima location depend on the number of the scalar fields N. We shall see the shapes of minima location and consider their resulting cosmic defects in each case below.

(i) $N = 1$

The positions of minima are distributed discrete values in the field space at $\phi = \pm v$. At the time of the phase transition, the scalar field goes to the either minima $\phi = v$ or $\phi = -v$ correlating each other within the horizon scale at that time. However in larger scale it goes randomly. Then VEVs can differ in each place at larger scales than the horizon size at the phase transition time. Here the field value of the scalar field has to satisfy continuity in the three dimensional space in the universe and in the field space as well. This means that there should be a wall like region which satisfies $\phi = 0$ between the regions whose field values are $\phi = v$ and $\phi = -v$ (see fig.2.2).

In such regions, the symmetry of the scalar field is restored ($\phi = 0$), and the energy density is large because of the potential barrier of the scalar field $V(0) = \lambda v^4/4$. The length scale of the high energy region can be calculated as $\ell \sim (\lambda/2)^{-1/2} v^{-1}$ and the surface density of domain wall is $\sigma \lambda^{1/2} v^3$ [29]. This wall like potential barrier is called domain walls [8, 29, 31].

(ii)$N = 2$

The minima draw a circle in the two dimensional field space $\Phi^t \Phi = \phi_1^2 + \phi_2^2 = v^2$. In the same way as the domain wall creation, the scalar fields go to the minima where $\phi_1^2 + \phi_2^2 = v^2$ in the field space at the time of the phase transition. They distribute on the circle randomly at large scales and the field value can be written as $\phi_1 = v \sin\theta$ and $\phi_2 = v \cos\theta$. Then, from the same reason with the case of $N = 1$, there are symmetry restored regions, which are surrounded by the scalar fields which satisfy the continuous phase of $\theta : 0 \to 2\pi$. In this case, the symmetry restored regions, whose field values are $\phi_1 = \phi_2 = 0$, are string like high energy regions (see fig.2.2) and these are called cosmic strings [8, 29, 31]. Here the thickness of strings can be estimated as $r_s \sim \lambda^{-1/2} v^{-1}$ and its linear density is given as $\mu \sim v^2$ [29].

You can see that the dimension of the cosmic defects is given as $\dim = d - N$, where d is the spacial dimension of the universe. The projection of the field space on the space of the universe leads such a relation [29].

(iii)$N = 3$

As with the case of cosmic string, the minima draw a two dimensional spherical surface in the three dimensional field space $\Phi^t \Phi = \phi_1^2 + \phi_2^2 + \phi_3^2 = v^2$ and the field values distribute randomly on the two dimensional spherical surface at large scales. In this case, considering the projection of the spherical surface in the field space on the three dimensional universe, we can find points which should restore the symmetry in the two dimensional spherical surfaces. These are the zero dimensional ($\dim = 3 - 3 = 0$) point like defects (see fig.2.2), called monopoles [8, 29, 31]. The size of the monopole is approximately $r_m \sim \lambda^{-1/2} v^{-1}$ and its mass is $m_m \sim \lambda^{-1/2} v$ [29].

(iv) $N \geq 4$

In this case, the stable minima of scalar fields draw a $N - 1$ dimensional spherical surface in a N dimensional field space, $\Phi^t \Phi = \phi_1^2 + \phi_2^2 + ... + \phi_{N \geq 4}^2 = v^2$, and we can project this surface onto the three dimensional universe without having any symmetry

restored points. Then, we have no high energy region in the universe caused by the potential barrier of these scalar fields, but the configuration of the scalar fields evolves according to the evolution of the universe under the constraint of $\Phi^t\Phi = v^2$. At the time of the phase transition, the scalar fields distribute randomly on a $N-1$ spherical surface at larger scales than that of the horizon scale at that time. As the universe evolves, the horizon evolves larger and the scalar fields which come into the horizon scale start to affect each other. Then the scalar fields move on the $N-1$ dimensional spherical surface in the field space and their motion can affect on the spacetime of the universe via their energy momentum tensor. These self-ordering scalar fields are called textures [29, 31].

These defects are generated a few in the horizon scale at the time of the phase transition. According to the evolution of the universe, the horizon scale of the universe takes in amount of ancient horizon scales. This means that many defects can exist in the horizon scale at the late time and they can interact each other. We know that if we assume the energy scale of phase transitions as the GUT scales, the created domain walls have too large mass in the horizon scale, more than the total mass of galaxies, and it can change the evolution history of the universe. We expect there is no such a remnant from recent cosmological observations. Considering monopoles, in the same consideration with the domain wall, we expect they should have too large energy density, larger than the critical density of the universe, in the horizon scale at present. However if we consider an inflationary epoch after the creation of monopoles, they are diluted and only a few monopoles can exist in the horizon scale at present and the number of monopoles should be small not to affect the cosmological quantities.

Hereafter we consider cosmic strings, textures and their effects on cosmological observables as realistic cosmic defects.

2.3 Cosmic strings and their network evolution

In this section, we review the evolution of individual strings and the string network according to [1]. We first introduce the energy momentum tensor of the individual strings. Moreover, by considering the evolution of the separations, motions, and decays of the strings, we calculate the energy momentum tensor of the string network. Here we assume a homogeneous and isotropic expanding universe described by the FLRW metric given by

$$ds^2 = a(\eta^2)(-d\eta^2 + d\vec{x}^2). \tag{2.3.62}$$

2.3.1 Wiggly string

Here we introduce the action and the energy stress tensor of a wiggly cosmic string on the string worldsheet following [32]. We define the string worldsheet (ζ_1, ζ_2) in four dimensional space-time, where $\zeta_1 = \eta$ is the conformal time defined in (2.3.62). Using these conditions, we can calculate the action density as

$$S = -\mu \int_\Sigma dA \tag{2.3.63}$$

$$= -\mu \int_\Sigma d^2\zeta \left[-\det_{ab}\left(\gamma^{ab}\right)\right]^{\frac{1}{2}}, \tag{2.3.64}$$

where

$$\gamma^{ab} = g_{\mu\nu}\frac{\partial x^\mu}{\partial \zeta_a}\frac{\partial x^\nu}{\partial \zeta_b} \tag{2.3.65}$$

is the metric on the string worldsheet. Here μ is the string energy density per unit length. From the definition, we can write the energy stress tensor of the string as

$$T^{\mu\nu} = \frac{\mu}{\sqrt{-g}}\int_\Sigma d^2\zeta \ \left\{\epsilon \dot{x}^\mu \dot{x}^\nu - \epsilon^{-1} x'^\mu x'^\nu\right\}\delta^{(4)}(y - x(\zeta)), \tag{2.3.66}$$

with

$$\epsilon = \sqrt{\frac{\vec{x}'^2}{1-\dot{\vec{x}}^2}}, \tag{2.3.67}$$

where dots and primes represent derivatives with respect to the conformal time and ζ_2, respectively, and we have chosen the gauge as $\dot{x}^\mu x'_\mu = 0$. Following [33], the string tension T and the linear energy density U can be defined by

$$\sqrt{-g}T^{\mu\nu}(y) = \int_\Sigma d^2\zeta \ \sqrt{-\gamma}\left\{U u^\mu u^\nu - T v^\mu v^\nu\right\}\delta^{(4)}(y - x(\zeta)), \tag{2.3.68}$$

where

$$u^\mu u_\mu = -v^\mu v_\mu = 1, \quad u^\mu v_\mu = 0, \tag{2.3.69}$$

$$(u^\mu v^\rho - v^\mu u^\rho)(u_\rho v_\nu - v_\rho u_\nu) = u^\mu u_\nu - v^\mu v_\nu = \eta^\mu_\nu, \tag{2.3.70}$$

$$\eta^{\mu\nu} = \gamma^{ab} x^\mu_{,a} x^\nu_{,b}, \tag{2.3.71}$$

and

$$u^\mu = \frac{\sqrt{\epsilon}\dot{x}^\mu}{(-\gamma)^{1/4}}, \quad v^\mu = \frac{x'^\mu}{\sqrt{\epsilon}(-\gamma)^{1/4}}. \tag{2.3.72}$$

We can easily check that u^μ and v^μ satisfy (2.3.69) $\sim$ (2.3.71). Substituting (2.3.72) into (2.3.68) and comparing with (2.3.66), we can see that

$$U = T = \mu. \tag{2.3.73}$$

This is the equation of state for a Nambu–Goto string. In practice, in lattice simulations of cosmic strings, the strings are macroscopically straight, but they have wiggles from a microscopic viewpoint [34, 35]. Even though the cosmic strings are macroscopic and straight on the cosmological scale ($\sim$ Mpc), their macroscopic equations of state are affected by the microscopic wigglinesses. The equation of state for the wiggly string, smoothing out the small scale structures, is shown in [33, 36]. In this case, we employ effective values of the string tension $\tilde{T}$ and the linear energy density $\tilde{U}$, with which the equations of states for the wiggly string are denoted as

$$\tilde{T} = \frac{\mu}{\alpha}, \quad \tilde{U} = \alpha\mu. \tag{2.3.74}$$

Here α is the "wiggliness parameter", which is a function of time and the string coordinate ζ. The evolution of α is estimated in [32, 34, 37], which show that $\alpha \sim 1.9$ in the radiation dominated era and $\alpha \sim 1.5$ in the matter dominated era. In the late time universe, when the cosmological constant dominates, wiggliness is smoothed out by the exponential expansion of the universe and α becomes equal to unity. Substituting the effective values of (2.3.74) into (2.3.68), we can write the effective energy momentum tensor of a wiggly string $\tilde{T}^{\mu\nu}$ as

$$\tilde{T}^{\mu\nu}(y) = \frac{1}{\sqrt{-g}} \int_\Sigma d^2\zeta \, \sqrt{-\gamma} \left\{ \tilde{U} u^\mu u^\nu - \tilde{T} v^\mu v^\nu \right\} \delta^{(4)}(y - x(\zeta)) \tag{2.3.75}$$

$$= \frac{\mu}{\sqrt{-g}} \int_\Sigma d^2\zeta \, \left\{ \epsilon\alpha \dot{x}^\mu \dot{x}^\nu - \frac{x'^\mu x'^\nu}{\epsilon\alpha} \right\} \delta^{(4)}(y - x(\zeta)). \tag{2.3.76}$$

If we consider magnetic field generation by the string network, the wiggliness affects the magnetic field spectrum only through a constant factor α^2. Here we set $\alpha = 1$ for simplicity, which represents straight strings and gives a conservative estimate of the amplitude of the magnetic fields.

2.3.2 Evolution of the string network

Following the one-scale model [38, 39, 40], the network of cosmic strings can be characterized by a single parameter, the correlation length L, which is defined as

$$L^2 = \frac{\mu}{\rho_{\rm string}}, \tag{2.3.77}$$

where $\rho_{\rm string}$ is the energy density of the cosmic string. To simplify the expressions, we introduce the comoving correlation length $l = L/a$. From the energy conservation law and the equation of motion of the string, we can obtain the evolution equations

of the string network as [38, 39, 40]:

$$\frac{dl}{d\eta} = \mathcal{H} l v^2 + \frac{1}{2}\tilde{c} v, \tag{2.3.78}$$

$$\frac{dv}{d\eta} = (1-v^2)\left(\frac{\tilde{k}}{l} - 2\mathcal{H} v\right), \tag{2.3.79}$$

where $\mathcal{H} = \dot{a}/a$ is the conformal Hubble parameter,

$$v = \sqrt{\frac{\int d\sigma \epsilon \vec{\dot{x}}^2}{\int d\sigma \epsilon}},$$

is the string's rms velocity, $\tilde{c}$ is the loop–chopping efficiency,

$$\tilde{k} = \frac{\int d\sigma \epsilon (1-\vec{\dot{x}}^2)\vec{\dot{x}} \cdot \hat{u}}{v(1-v^2)\int d\sigma \epsilon},$$

is the effective curvature of the strings, and $\hat{u}$ is the unit vector of the curvature radius vector of the string. In our calculation, we use an ansatz for relativistic strings as [41],

$$\tilde{k}(v) = \frac{2\sqrt{2}}{\pi}\frac{1-8v^6}{1+8v^6}.$$

Here we consider the reduction of the energy density by the expansion of the universe and the decrease of the total length of infinite strings in the Hubble horizon. The total length of infinite strings decreases because infinite strings are chopped due to their collisions, making string loops that immediately decay by radiating gravitational waves from their peakedness [42]. The loop–chopping efficiency $\tilde{c}$ represents the rate at which strings become loops. In general, $\tilde{c}$ is a function of time as shown in [32, 40]; however its value does not vary much. In the radiation dominated era, $\tilde{c} = c_r = 0.23$, and in the matter dominated era, $\tilde{c} = c_m = 0.18$.

We describe the Fourier transform of the energy momentum tensor of an individual string as

$$\begin{aligned}\Theta^{\mu\nu}(\vec{k},\eta) &= \int d^3x e^{i\vec{k}\cdot\vec{x}} T^{\mu\nu}(x) \\ &= \int_{-l/2}^{l/2} d\zeta e^{i\vec{k}\cdot\vec{X}}\left[\epsilon\alpha \dot{X}^\mu \dot{X}^\nu - \frac{X'^\mu X'^\nu}{\epsilon\alpha}\right],\end{aligned} \tag{2.3.80}$$

where the four vector $X^\mu(\zeta,\eta) = (\eta, \vec{X})$ denotes the coordinates in which the string segment exists. We can represent the vector as

$$X^0 = \eta, \quad \vec{X} = \vec{x}_0 + \zeta\hat{X}' + v\eta\hat{\dot{X}}, \tag{2.3.81}$$

where $\vec{x}_0$ is a random vector that denotes the initial position of the string's mass center, and $\hat{X}'$ and $\hat{\dot{X}}$ are random unit vectors that fulfill $\hat{X}' \cdot \hat{\dot{X}} = 0$. In the expression for the energy momentum tensor of the string, the initial position coordinate $\vec{x}_0$ appears only as a phase in the inner product with $\vec{k}$. We can therefore deal with $\vec{k} \cdot \vec{x}_0$ as a random initial phase $\phi_0 : [0, 2\pi]$. Because individual strings have their own initial positions, aligned directions, and velocity directions, we write those of the m-th string as $\vec{x}_0^m, \hat{X}'^m$ and $\hat{\dot{X}}^m$. Summing up our description of strings, we obtain the total energy momentum tensor of the string network. Fourier transform of the total energy momentum tensor of the string network $\Theta_{\mu\nu}(\vec{k}, \tau)$ is given by [32],

$$\Theta_{\mu\nu}(\vec{k}, \eta) = \sum_{m=1}^{N_0} \Theta_{\mu\nu}^m(\vec{k}, \eta) T^{\rm off}(\eta, \eta_m), \tag{2.3.82}$$

where N_0 is the initial number of the strings, $\Theta_{\mu\nu}^m(\vec{k}, \tau)$ is the energy momentum tensor of the individual strings, η_m is the time of decay for the m-th string, and $T^{\rm off}$ is the smoothing function of the decay. We adopt the functional form of $T^{\rm off}$ from [32, 43] that is given by

$$T^{\rm off}(\eta, \eta_m) = \begin{cases} 1, & (\eta < f\eta_m) \\ 1/2 + (x^3 - 3x)/4, & (f\eta_m < \eta < \eta_m) \\ 0, & (\eta_m < \eta), \end{cases} \tag{2.3.83}$$

$$x = 2\frac{\ln(f\eta_m/\eta)}{\ln f} - 1. \tag{2.3.84}$$

Here $0 < f < 1$ is a parameter which controls the speed of the strings decay. We fix this value to $f = 0.5$. Considering (2.3.83) for individual infinite strings, we take account of the decrease in the number of infinite strings by their decay into loops due to their intersections. Because of their random initial positions and directions of motion, the decay time for each string η_m is fixed randomly.

2.4 Textures with non-linear sigma model

We consider a model of N scalar fields with a global $O(N)$ symmetry, which undergoes symmetry breaking in the early universe according to [2]. The Lagrangian of the model is given by

$$\mathcal{L} = -\frac{1}{2}\nabla_\mu \Phi^t \nabla^\mu \Phi - \frac{\lambda}{4}(\Phi^t \Phi - v^2)^2 + \mathcal{L}_T. \tag{2.4.85}$$

Here $\Phi = (\phi_1, \phi_2, ..., \phi_N)$ is an array of N real scalar fields, v is the vacuum expectation value (VEV) of the scalar fields after symmetry breaking, λ is the self-coupling

constant, and $\mathcal{L}_T \sim T^2\Phi^t\Phi$ is the thermal term of the Lagrangian. Deep in the radiation-dominated universe, the thermal term is dominant in the Lagrangian of the scalar fields. As the temperature of the universe goes down, this thermal term gets smaller. When the term becomes negligible a spontaneous symmetry breaking occurs. At energy scales well below v, the field values are confined on the $N-1$ dimensional sphere in the N dimensional field space so that $\Phi^t(\vec{x},\eta)\Phi(\vec{x},\eta) = v^2$. Under this condition, in the large-N limit, the equation of motion for the scalar fields can be derived as

$$\nabla^\mu\nabla_\mu\beta_a + (\nabla_\mu\beta_b)\cdot(\nabla^\mu\beta_b)\,\beta_a = 0, \tag{2.4.86}$$

where the indices a and b run over $1,\ldots,N$ and summations with respect to deprecated indices are implicit. This is the equation of motion for the scalar fields in the NLSM. If $N \leq 3$, topological defects such as domain walls, cosmic strings and monopoles are produced, where the scalar fields can restore the $O(N)$ symmetry and possess the higher energy density.

In this paper we consider cases with $N \geq 4$, where non-topological defects, or textures, form. Let us consider the flat Friedmann-Lemaître-Robertson-Walker universe with the metric

$$ds^2 = g_{\mu\nu}dx^\mu dx^\nu = a^2(\eta)(-d\eta^2 + d\vec{x}^2)\ , \tag{2.4.87}$$

where $a(\eta)$ is the cosmic scale factor and η is the conformal time. In the large-N limit, making an ansatz that $\langle(\nabla_\mu\beta_a)\cdot(\nabla^\mu\beta_a)\rangle = T_0 a^{-2}\eta^{-2}$, we can obtain the analytic solution as [44] [45]

$$\beta_a(\vec{k},\eta) = \sqrt{A_\nu}\left(\frac{\eta}{\eta_*}\right)^{3/2}\frac{J_\nu(k\eta)}{(k\eta)^\nu}\beta_a(\vec{k},\eta_*) \equiv f(k,\eta,\eta_*)\beta_a(\vec{k},\eta_*), \tag{2.4.88}$$

where $\nu = \mathrm{d}\ln\mathrm{a}/\mathrm{d}\ln\eta + 1$, $A_\nu = 4\Gamma(2\nu-1/2)\Gamma(\nu-1/2)/3\Gamma(\nu-1)$ and $T_0 = 3\nu - 9/4$. In eq. (2.4.88), η_* is the time of phase transition and $\beta_a(\vec{k},\eta_*)$ is the initial value of scalar fields, whose two-point correlation function can be given as

$$\left\langle \beta_a(\vec{k}_1,\eta_*)\beta_b^*(\vec{k}_2,\eta_*)\right\rangle = \frac{6\pi^2\eta_*^3}{N}\delta_{ab}\ (2\pi)^3\delta(\vec{k}_1 - \vec{k}_2). \tag{2.4.89}$$

The above relation is only valid for $k \ll 1/\eta_*$, which follows, in the large-N limit, from the fact that the scalar fields take their VEV independently in each horizon at η_*.[*1] We also note that $\beta_a(\vec{k},\eta_*)$ is Gaussian at these scales.

[*1] On small scales $k \gtrsim 1/\eta_*$, initial scalar fields become homogenous and correlation function of eq. (2.4.89) should vanish. We however note that our argument does not depend on the correlation function on these scales.

We denote a correlation function of β_a as a product of the transfer function and the initial amplitude as

$$\left\langle \beta_a(\vec{k}_1,\eta)\beta_b^*(\vec{k}_2,\eta)\right\rangle = F(k_1,k_2,\eta,\eta_*)\left\langle \beta_a(\vec{k}_1,\eta_*)\beta_b^*(\vec{k}_2,\eta_*)\right\rangle \ , \tag{2.4.90}$$

where $F(k_1,k_2,\eta,\eta_*) \equiv f(k_1,\eta,\eta_*)f(k_2,\eta,\eta_*)$. From eq.(2.4.88) and eq.(2.4.89), we can see that the dependence of eq.(2.4.90) on η_* is canceled out. Therefore we omit η_* from the equations hereafter and write as $F(k_1,k_2,\eta,\eta_*) = F(k_1,k_2,\eta)$ and $\beta_a(\vec{k},\eta_*) = \beta_a(\vec{k})$. Finally the energy momentum tensor of the scalar fields is given by

$$T^{\phi}_{\mu\nu} = v^2\left[\partial_\mu\beta_a\partial_\nu\beta_a - \frac{1}{2}g_{\mu\nu}\partial_\lambda\beta_a\partial^\lambda\beta_a\right]. \tag{2.4.91}$$

2.4.1 Power spectrum in the NLSM

Let us consider the power spectrum of some variable $X(\vec{k})$ and $Y(\vec{k})$ which is generated by scalar fields following the NLSM. At first, let us write $X(\vec{k})$ using its transfer function $F_X(q,p)$ and $F_Y(q,p)$ as

$$X(\vec{k}) = \int \frac{\mathrm{d}^3p}{(2\pi)^3}\frac{\mathrm{d}^3q}{(2\pi)^3}F_X(q,p)\beta_s(\vec{p})\beta_s(\vec{q})(2\pi)^3\delta(\vec{k}-\vec{p}-\vec{q}), \tag{2.4.92}$$

and a similar expression for $Y(\vec{k})$. The (cross) power spectrum of X and Y is defined by

$$\left\langle X(\vec{k})Y^*(\vec{k}')\right\rangle \equiv (2\pi)^3\mathcal{P}_{XY}(k)\ \delta(\vec{k}-\vec{k}'). \tag{2.4.93}$$

To calculate the power spectrum, we need to calculate four point correlation function of scalar fields. This is given by

$$\begin{aligned}
\langle\beta_a(\vec{q}_1)\beta_a(\vec{p}_1)\beta_b^*(\vec{q}_2)\beta_b^*(\vec{p}_2)\rangle &= \langle\beta_a(\vec{q}_1)\beta_a(\vec{p}_1)\rangle\langle\beta_b^*(\vec{q}_2)\beta_b^*(\vec{p}_2)\rangle \\
&\quad + \langle\beta_a(\vec{q}_1)\beta_b^*(\vec{q}_2)\rangle\langle\beta_a(\vec{p}_1)\beta_b^*(\vec{p}_2)\rangle \\
&\quad + \langle\beta_a(\vec{q}_1)\beta_b^*(\vec{p}_2)\rangle\langle\beta_a(\vec{p}_1)\beta_b^*(\vec{q}_2)\rangle \\
&= (6\pi^2)^2\ (2\pi)^3\delta(\vec{p}_1+\vec{q}_1)\ (2\pi)^3\delta(\vec{p}_2+\vec{q}_2) \\
&\quad + \frac{(6\pi^2)^2}{N}\ (2\pi)^3\delta(\vec{q}_1-\vec{q}_2)\ (2\pi)^3\delta(\vec{p}_1-\vec{p}_2) \\
&\quad + \frac{(6\pi^2)^2}{N}\ (2\pi)^3\delta(\vec{q}_1-\vec{p}_2)\ (2\pi)^3\delta(\vec{p}_1-\vec{q}_2).
\end{aligned} \tag{2.4.94}$$

Here, $\frac{(6\pi^2)^2}{N} = \mathcal{P}^N_{\rm ini}$ is the initial power spectrum of the scalar fields. Substituting eq. (2.4.94) to eqs. (2.4.92) and (2.4.93), and using $F(q,p) = F(p,q)$, we calculate the

cross correlation as

$$\begin{aligned}
\left\langle X(\vec{k})Y^*(\vec{k}')\right\rangle &= \int \frac{d^3q_1}{(2\pi)^3}\frac{d^3p_1}{(2\pi)^3}\frac{d^3q_2}{(2\pi)^3}\frac{d^3p_2}{(2\pi)^3} \\
&\quad \times F_X(q1,p_1)F_Y^*(q_2,p_2)\left\langle \beta_a(\vec{q}_1)\beta_a(\vec{p}_1)\beta_b^*(\vec{q}_2)\beta_b^*(\vec{p}_2)\right\rangle \\
&\quad \times (2\pi)^3\delta(\vec{k}-\vec{p}_1-\vec{q}_1)\ (2\pi)^3\delta(\vec{k}'-\vec{p}_2-\vec{q}_2) \\
&= \int \frac{d^3q_1}{(2\pi)^3}\frac{d^3p_1}{(2\pi)^3}\frac{d^3q_2}{(2\pi)^3}\frac{d^3p_2}{(2\pi)^3}F_X(q_1,p_1)F_Y^*(q_2,p_2) \\
&\quad \left[\frac{(6\pi^2)^2}{N}\ (2\pi)^3\delta(\vec{q}_1-\vec{q}_2)\ (2\pi)^3\delta(\vec{p}_1-\vec{p}_2)\right. \\
&\quad \left. + \frac{(6\pi^2)^2}{N}\ (2\pi)^3\delta(\vec{q}_1-\vec{p}_2)\ (2\pi)^3\delta(\vec{p}_1-\vec{q}_2)\right] \\
&\quad \times (2\pi)^3\delta(\vec{k}-\vec{p}_1-\vec{q}_1)\ (2\pi)^3\delta(\vec{k}'-\vec{p}_2-\vec{q}_2) \\
&= \mathcal{P}_{\rm ini}^N(2\pi)^3\delta(\vec{k}-\vec{k}') \\
&\quad \times \int \frac{d^3q}{(2\pi)^3}\left[F_X(q,|\vec{k}-\vec{q}|)F_Y^*(q,|\vec{k}-\vec{q}|)+F_X(|\vec{k}-\vec{q}|,q)F_Y^*(q,|\vec{k}-\vec{q}|)\right] \\
&= 2\mathcal{P}_{\rm ini}^N(2\pi)^3\delta(\vec{k}-\vec{k}')\int \frac{d^3q}{(2\pi)^3}F_X(q,|\vec{k}-\vec{q}|)F_Y^*(q,|\vec{k}-\vec{q}|)\ . \qquad (2.4.95)
\end{aligned}$$

Therefore the power spectrum $\mathcal{P}_{XY}$ is read off as

$$\begin{aligned}
\mathcal{P}_{XY}(k) &= 2\mathcal{P}_{\rm ini}^N\int \frac{d^3q}{(2\pi)^3}F_X(q,|\vec{k}-\vec{q}|)F_Y^*(q,|\vec{k}-\vec{q}|) \\
&= \frac{\mathcal{P}_{\rm ini}^N}{2\pi^2}\int dq\ q^2\int d\mu\ F_X(q,|\vec{k}-\vec{q}|)F_Y^*(q,|\vec{k}-\vec{q}|), \qquad (2.4.96)
\end{aligned}$$

where $\mu=\hat{k}\cdot\hat{q}$.

Part.II

Magnetic fields generation from cosmic defects

In this part, we introduce the generation of the cosmological scale magnetic fields from cosmic string networks and textures. These defects induce the vector mode cosmological perturbations in the early universe and such perturbations lead magnetic fields at cosmological scales [1, 2]. Here we first discuss the generation mechanism of the magnetic fields, focusing on the tight coupling approximation (TCA) between the photon fluid and the baryon fluid in the early universe.

Chapter.3

Primordial magnetic fields generation

Here we explain how magnetic fields can generally be produced at cosmological scales in the universe. The most reasonable way to produce magnetic fields at cosmological scales is creating them through physical mechanisms at cosmological scales, such as second-order cosmological couplings of perturbations [46], cosmological phase transitions [1, 2] and so on. These events can generate vector mode perturbations at cosmological scales and they induce a relative velocity between photon and baryon fluids via a slight violation of the tight coupling between photon and baryon fluids. This relative velocity originates the magnetic fields in the early universe. Here we introduce the tight coupling approximation in the standard cosmological perturbation theory, and then derive the evolution equation for magnetic fields which is driven by the relative velocity between photon and baryon fluids.

3.1 The Euler equations

The vorticity of the spacetime plays an important role to generate magnetic fields in the vector mode perturbations. In the standard cosmological perturbation theory, there is no source term for the vorticity in the vector mode perturbations, and it has only a decaying solution (see section 1.2). However, when we consider external sources of the vector mode perturbations such as second order couplings of density perturbations or cosmic defects, the vorticity can be generated. Then the vorticity induces the anisotropic stress of the photon fluid and it gives rise to the velocity of the photon fluid in the vector mode. In the early universe, photons scatter with hot electrons frequently and the scattered electrons stuck together with baryons. In this phase, photon and baryon fluids move together and this state is called the tight coupling. Here we show the mechanism of the tight coupling and solve the relative

velocity between the photon and baryon fluid using the Euler equations.

We start with the Boltzmann equation for the distribution function of particles at position $\vec{x}$ and velocity $\vec{v}$

$$\frac{df}{dt} = \frac{\partial f}{\partial t} + \vec{v} \cdot \frac{\partial f}{\partial \vec{x}} + \vec{a} \cdot \frac{\partial f}{\partial \vec{v}} = \left(\frac{\partial f}{\partial t} \right)_C , \tag{3.1.1}$$

where $f(t, \vec{x}, \vec{v})$ is the distribution function in the six dimensional phase space, $\vec{a}$ is the acceleration which affects particles at position $\vec{x}$, and $(\partial f/\partial t)_C$ is the collision term which represents the interactions between particles. This equation describes the evolution of the distribution function of particles in the phase space. Taking velocity moments, we can obtain the equations of motions for velocity, anisotropic stress, and so on. Let us show a simple example in case there are no any external forces $\vec{a} = 0$ in collisionless system. Integrating eq.(3.1.1) by d^3v, and multiplying $\vec{v}$ with eq.(3.1.1) and integrating by d^3v, we obtain the zero-th and primary moments of the Boltzmann equation as

$$\frac{\partial n}{\partial t} + \nabla(n\vec{u}) = 0, \tag{3.1.2}$$

$$\frac{\partial n u_i}{\partial t} + \partial_j(n\Pi_{ij}) = 0, \tag{3.1.3}$$

where $n = \int d^3v f$ is the zero-th order moment which corresponds to the number density in three dimensional space, $\vec{u} = n^{-1} \int d^3v \vec{v} f$ is the primary moment which describes the mean velocity, and $\Pi_{ij} = n^{-1} \int d^3v \ v_i v_j f$ is the secondary moment which is equivalent to the anisotropic stress. These represent the equations of motions for each moment and we can see the higher order moments affect the lower order moments. Even in such a simple case, the moments are related each other. It is of course true for more complicated collisional systems with external forces.

Hereafter we see the Euler equations for baryon and photon fluids in the vector mode, in the early universe. Let us see the Euler equation for the baryon fluid first. In the same way as [47, 48], assuming synchronous gauge (1.2.20), we obtain the equation of motion for the baryon fluid,

$$\dot{v}_b + \mathcal{H} v_b = R\dot{\tau}(v_\gamma - v_b), \tag{3.1.4}$$

where v_b is the velocity of the baryon fluid, v_γ is the velocity of the photon fluid, dot represents the derivative by the conformal time, $R = 4\rho_\gamma/3\rho_b$ is the photon baryon ratio, $\dot{\tau} = a n_e \sigma_T$ is the conformal time derivative of the optical depth with n_e and σ_T being the electron number density and the Thomson scattering cross section. There are no pressure or anisotropic stress terms in the equation of motion for the baryon

fluid, because of the equation of state $P = 0$. This means that there is no effects from the higher order Euler equations on the baryon fluid velocity v_b. Thus, the only effective term which drives the baryon fluid is the collision term $(\partial f/\partial t)_C$. Here we consider the early hot universe in which the Compton scattering between the photon fluid and electrons takes place frequently and the scattered electrons move with the baryon fluid due to the Coulomb interaction. In such a situation, the collision term for the baryon fluid $R\dot{\tau}(v_\gamma - v_b)$ is originated from the Compton scattering.

Next, we discuss the Euler equations for the photon fluid. The equations can be categorized into three spices for the photon fluid. One is the equation for the intensity, the others correspond to the equations of motions for polarizations. Let us see the equation of motions for the intensity first. The Euler equations for intensity of photons in vector mode are given by [47, 48, 49],

$$\dot{v}_\gamma + \frac{k}{8}\Pi_\gamma = -\dot{\tau}(v_\gamma - v_b), \tag{3.1.5}$$

$$\dot{\Pi}_\gamma + \frac{8}{5}kI_3 - \frac{8}{5}kv_\gamma = -\dot{\tau}\left(\frac{9}{10}\Pi_\gamma - \frac{9}{5}E_2\right) + \frac{8}{5}k\sigma, \tag{3.1.6}$$

$$\dot{I}_\ell + k\frac{\ell}{2\ell+1}\left(\frac{\ell+2}{\ell+1}I_{\ell+1} - I_{\ell-1}\right) = -\dot{\tau}I_\ell, \quad (\ell \geq 3), \tag{3.1.7}$$

where Π_γ is the anisotropic stress of the photon fluid, E_2 is the secondary moment of the E-mode polarization, $\sigma = \dot{h}_V/k$ is the vorticity in the spacial metric, h_V is the vector mode perturbation in eq.(1.2.27) and we define I_ℓ as the ℓ-th order moment of the intensity. We consider the Compton scattering term as the collision term which affects the motion of the photon fluid, in the same way as the case of the baryon fluid. The main differences between the photon and baryon fluids are the existence of the anisotropic stress Π_γ in (3.1.5) and its evolution relating with the polarizations. The Euler equations for the polarizations are written as,

$$\dot{E}_\ell + \frac{(\ell+3)(\ell+2)(\ell-1)}{(\ell+1)^3(2\ell+1)}kE_{\ell+1} - \frac{\ell}{2\ell+1}kE_{\ell-1} = -\dot{\tau}\left(E_\ell - \frac{2}{15}\zeta\delta_{\ell 2}\right) + \frac{2}{\ell(\ell+1)}kB_\ell, \tag{3.1.8}$$

$$\zeta \equiv \frac{3}{4}I_2 + \frac{9}{2}E_2, \tag{3.1.9}$$

$$\dot{B}_\ell + \frac{(\ell+3)(\ell+2)(\ell-1)}{(\ell+1)^3(2\ell+1)}kB_{\ell+1} - \frac{\ell}{2\ell+1}kB_{\ell-1} = -\frac{2}{\ell(\ell+1)}kE_\ell, \tag{3.1.10}$$

where E_ℓ and B_ℓ are the ℓ-th moment of the E- and B-mode polarization. You can see that the Euler equations for the baryon, photon intensity and polarizations affect each

other. In case of magnetic fields generation from some external sources only coupled with gravity, all moments in the Euler equations are originated in the vorticity σ. This vorticity σ induces the anisotropic stress of photon first and it drives the photon motion. Then the baryon fluid is pushed because of the Compton scattering between the photons and electrons which follow the baryon fluid. This mechanism is valid in the early universe in which the photon fluid scatters with electrons frequently, and when the photon and baryon fluids are coupled tightly.

3.2 Tight coupling approximation

In general, it is difficult to solve the Euler equations because of infinite number of the moments and their correlations. Then we need to introduce a cutoff order for moments to solve them. When we consider the situation of the tight coupling between the photon and baryon fluids, such as in the early universe, we can partially understand their behavior analytically. We can give the initial conditions for the Euler equations at the early universe by considering the tight coupling approximation. Here we will see the necessary condition of the tight coupling approximation and its role in estimating the moments, especially the relative velocity between the photon and baryon fluids $(v_\gamma - v_b)$ in anticipation of the magnetic fields generation at final step. The condition for the tight coupling between the photon and baryon fluids is given by

$$\frac{k}{\dot{\tau}} \ll 1, \tag{3.2.11}$$

where $k/\dot{\tau}$ the ratio between the mean free path of the photon and the wavelength which we focus on, and it is called the tight coupling parameter. In the early universe, this condition is well satisfied at cosmological scales, meaning that photons are scattered frequently in focused scales. In that case, we can expand each moment by the tight coupling parameter $k/\dot{\tau}$ as,

$$v = v^{(0)} + v^{(1)} + v^{(2)} + v^{(3)} + ... \tag{3.2.12}$$

where the index $^{(n)}$ represents the order of the tight coupling. Hereafter we will consider the vector mode perturbations. Then, solving the Euler equations, we obtain zero-th order expansion for each moment as

$$v_\gamma^{(0)} - v_b^{(0)} = \Pi_\gamma^{(0)} = I_\ell^{(0)} = E_\ell^{(0)} = B_\ell^{(0)} = 0. \tag{3.2.13}$$

When we consider the first order expansion, then the relative velocity, the anisotropic stress and the secondary moment of E-mode polarization are given by

$$v_\gamma^{(1)} - v_b^{(1)} = \left(\frac{k}{\dot{\tau}}\right) \frac{\mathcal{H}}{(1+R)k} v_\gamma^{(0)}, \tag{3.2.14}$$

$$\Pi_\gamma^{(1)} = \frac{32}{15}\left(\frac{k}{\dot{\tau}}\right)(v_\gamma^{(0)} + \sigma^{(0)}), \tag{3.2.15}$$

$$E_2^{(1)} = \frac{8}{45}\left(\frac{k}{\dot{\tau}}\right)(v_\gamma^{(0)} + \sigma^{(0)}). \tag{3.2.16}$$

Here you can see the relative velocity is described as $v_\gamma^{(1)} - v_b^{(1)} \propto v_\gamma^{(0)}$. As I mentioned in the previous subsection, the velocity of the photon fluid is induced by the anisotropic stress Π_γ. This means that the lowest order of v_γ is the first order of the tight coupling and $v_\gamma^{(0)}$ corresponds to zero. Then the first order of the relative velocity also goes to zero, and the leading order of the relative velocity should be the second order of the tight coupling. Here the second order expansions for the relative velocity $v_\gamma^{(2)} - v_b^{(2)}$, the anisotropic stress $\Pi_\gamma^{(2)}$, and the polarization term $E_2^{(2)}$ are written as

$$\begin{aligned} v_\gamma^{(2)} - v_b^{(2)} =& \left(\frac{k}{\dot{\tau}}\right)\frac{\mathcal{H}}{(1+R)k} v_\gamma^{(1)} - \frac{4}{15}\left(\frac{k}{\dot{\tau}}\right)^2 \frac{1}{1+R}(v_\gamma^{(0)} + \sigma^{(0)}) \\ & - \left(\frac{k}{\dot{\tau}}\right)^2 \frac{\mathcal{H} v_\gamma^{(0)}}{(1+R)^2 k^2}\left(\frac{\mathcal{H}R}{1+R} + \frac{\dot{\mathcal{H}}}{\mathcal{H}} + \mathcal{H} + \frac{\dot{v}_\gamma^{(0)}}{v_\gamma^{(0)}} - \frac{\ddot{\tau}}{\dot{\tau}}\right), \end{aligned} \tag{3.2.17}$$

$$\begin{aligned} \Pi_\gamma^{(2)} =& \frac{32}{15}\left(\frac{k}{\dot{\tau}}\right)(v_\gamma^{(1)} + \sigma^{(1)}) \\ & + \frac{176}{45}\left(\frac{k}{\dot{\tau}}\right)^2 \frac{1}{k}\left(\frac{\ddot{\tau}}{\dot{\tau}}(v_\gamma^{(0)} + \sigma^{(0)}) - (\dot{v}_\gamma^{(0)} + \dot{\sigma}^{(0)})\right), \end{aligned} \tag{3.2.18}$$

$$\begin{aligned} E_2^{(2)} =& \frac{8}{45}\left(\frac{k}{\dot{\tau}}\right)(v_\gamma^{(1)} + \sigma^{(1)}) \\ & + \frac{74}{135}\left(\frac{k}{\dot{\tau}}\right)^2 \frac{1}{k}\left(\frac{\ddot{\tau}}{\dot{\tau}}(v_\gamma^{(0)} + \sigma^{(0)}) - (\dot{v}_\gamma^{(0)} + \dot{\sigma}^{(0)})\right), \end{aligned} \tag{3.2.19}$$

where we keep terms which multiplied by $v_\gamma^{(0)}$ correspond to zero at this order, because we need these terms for the higher order expansion. At the end of the tight coupling epoch, $k/\dot{\tau} \sim 1$, we have to solve the Euler equations numerically without the tight coupling approximation. For the connection, we need to give the leading contribution of each moment accurately at the end of the tight coupling epoch and give accurate

'initial conditions' for the Euler equations. To obtain accurate conditions, we should count the required order of the tight coupling approximation, considering evolution equations like eqs.(3.1.4) and (3.1.5). The equations of motion at the n-th order of the tight coupling approximation, for the photon and baryon fluids velocities are given by

$$\dot{v}_b^{(n)} = -\mathcal{H} v_b^{(n)} + R\dot{\tau}(v_\gamma^{(n+1)} - v_b^{(n+1)}), \tag{3.2.20}$$

$$\dot{v}_\gamma^{(n)} = -\frac{k}{8}\Pi_\gamma^{(n)} - \dot{\tau}(v_\gamma^{(n+1)} - v_b^{(n+1)}). \tag{3.2.21}$$

Therefore, if we need the n-th order accurately, we have to know the relative velocity at the $(n+1)$-th order in the tight coupling approximation. As for the relative velocity $v_\gamma - v_b$, the leading term is in the second order of the tight coupling approximation $v_\gamma^{(2)} - v_b^{(2)}$, and we have to calculate $v_\gamma^{(2)}$ and $v_b^{(2)}$ accurately at the end of the tight coupling epoch. Thus we need the third order tight coupling approximation expression for the relative velocity $v_\gamma^{(3)} - v_b^{(3)}$ which is written as

$$\begin{aligned} v_\gamma^{(3)} - v_b^{(3)} =& \left(\frac{k}{\dot{\tau}}\right)\frac{\mathcal{H}}{(1+R)k} v_\gamma^{(2)} - \frac{4}{15}\left(\frac{k}{\dot{\tau}}\right)^2 \frac{1}{1+R}(v_\gamma^{(1)} + \sigma^{(1)}) \\ &- \left(\frac{k}{\dot{\tau}}\right)^2 \frac{\mathcal{H} v_\gamma^{(1)}}{(1+R)^2 k^2}\left(\frac{\mathcal{H}R}{1+R} + \frac{\dot{\mathcal{H}}}{\mathcal{H}} + \mathcal{H} + \frac{\dot{v}_\gamma^{(1)}}{v_\gamma^{(1)}} - \frac{\ddot{\tau}}{\dot{\tau}}\right) \\ &+ \frac{4}{15}\left(\frac{k}{\dot{\tau}}\right)^3 \frac{\mathcal{H}}{(1+R)^2 k}\sigma^{(0)} - \frac{2}{45}\left(\frac{k}{\dot{\tau}}\right)^3 \frac{1}{(1+R)^2 k}\left[(23+11R)\frac{\ddot{\tau}}{\dot{\tau}}\sigma^{(0)}\right. \\ &\left. -(17+11R)\dot{\sigma}^{(0)} - \frac{6\mathcal{H}R\sigma^{(0)}}{1+R}\right]. \end{aligned} \tag{3.2.22}$$

Now we know enough expansion for v_b and v_γ. In the same way with the case of the relative velocity $v_\gamma - v_b$, we need expansions for the anisotropic stress Π_γ and the polarization term E_2. The leading order of these moments are the first order of the tight coupling approximation, and therefore we need the second order terms of them given by eqs.(3.2.18) and (3.2.19) for accurate numerical calculation.

3.3 Magnetic fields generation

Now we can calculate the relative velocity between the photon and baryon fluids $\delta v \equiv v_\gamma - v_b$ accurately. Here we consider the magnetic fields generation induced by the relative velocity δv.

We know that the photon fluid scatter electrons more frequently than protons in the early universe, and it makes separation between electrons and protons. Then the

electric fields are produced and protons catch up with electrons. When we consider the vector mode perturbation, which is corresponding to the rotation mode, this scattering and catching up process can induce magnetic fields via the Maxwell equations, because of the rotation of the electric fields between electrons and protons. The strength of the electric fields depends on the relative velocity between the photon and the proton (i.e., baryon) fluids δv. The equation of motion for such magnetic fields are given by [50]

$$\frac{1}{a^2}\frac{d}{d\eta}(a^2 B^i) = \frac{4\sigma_T \rho_\gamma}{3e}\epsilon^{ijk}\partial_k \delta v_j, \tag{3.3.23}$$

where B^i is the magnetic flux density for direction i, e is the electric charge, and ϵ^{ijk} is the Levi-Civita tensor. Then we can describe the power spectrum of the magnetic fields in the Fourier space as

$$\begin{aligned} a^4 B^i(\vec{k},\eta)B_i^*(\vec{k}',\eta) =& \left(\frac{4\sigma_T}{3e}\right)^2 (\delta^{jl}\delta^{km} - \delta^{jm}\delta^{kl})k_k k'_m \\ &\times \int_0^\eta d\eta' a^2(\eta')\rho_\gamma(\eta')\delta v_j(\vec{k},\eta') \\ &\times \int_0^\eta d\eta'' a^2(\eta'')\rho_\gamma(\eta'')\delta v_l(\vec{k}',\eta''). \end{aligned} \tag{3.3.24}$$

To take the ensemble average of the magnetic fields, we need the ensemble average of the relative velocity spectrum. We denote the relative velocity spectrum as,

$$\left\langle \delta v_j(\vec{k},\eta')\delta v_l(\vec{k}',\eta'')\right\rangle = P_{jl}^{\rm vec}(\hat{k})P_{\delta v}(k)\delta v(k,\eta')\delta v(k,\eta'')(2\pi)^3\delta(\vec{k}-\vec{k}'), \tag{3.3.25}$$

where

$$P_{jl}^{\rm vec}(\hat{k}) = \delta_{jl} - \hat{k}_j\hat{k}_l, \tag{3.3.26}$$

is the projection of the vector mode which satisfies $P_{jl}^{\rm vec}(\hat{k})\hat{k}_j = 0$, $P_{\delta v}(k)$ is the initial power spectrum of relative velocity, and $\delta v(k,\eta)$ is the transfer function of the relative velocity. Here we define the ensemble average of the magnetic fields as

$$\left\langle B^i(\vec{k},\eta)B_i(\vec{k}',\eta)\right\rangle = (2\pi)^2 S_B(k,\eta)\delta(\vec{k}-\vec{k}'), \tag{3.3.27}$$

and we obtain

$$a^4\frac{k^3}{2\pi^2}S_B(k,\eta) = \frac{k^3}{2\pi^2}2P_{\delta v}(k)\left(\frac{4\sigma_T}{3e}\right)^2 k^2\left[\int_0^\eta d\eta' a^2(\eta')\rho_\gamma(\eta')\delta v(\vec{k},\eta')\right]^2. \tag{3.3.28}$$

In following chapters, we consider magnetic fields generation due to these processes. In addition, we have to take care of specific features in the spectrum of magnetic fields generated from cosmic defects. We have to consider the network structure and

its averaged feature for cosmic strings, and mode couplings of different wavenumbers for textures. We will see the magnetic fields generation from each defect according to [1, 2] hereafter.

Chapter.4

Primordial magnetic fields from the string network

Cosmic strings are a type of cosmic defect formed by a symmetry-breaking phase transition in the early universe. Individual strings would have gathered to build a network, and their dynamical motion would induce scalar, vector and tensor type perturbations. In this chapter, we focus on the vector mode perturbations arising from the string network based on the one scale model and calculate the time evolution and the power spectrum of the associated magnetic fields. We show that the relative velocity between photon and baryon fluids induced by the string network can generate magnetic fields over a wide range of scales based on standard cosmology. We obtain the magnetic field spectrum before recombination as $a^2B(k,z) \sim 4 \times 10^{-16} G\mu/((1+z)/1000)^{4.25}(k/\mathrm{Mpc}^{-1})^{3.5}$ Gauss on super-horizon scales, and $a^2B(k,z) \sim 2.4 \times 10^{-17} G\mu/((1+z)/1000)^{3.5}(k/\mathrm{Mpc}^{-1})^{2.5}$ Gauss on sub-horizon scales in co-moving coordinates. This magnetic field grows up to the end of recombination, and has a final amplitude of approximately $B \sim 10^{-17\sim-18} G\mu$ Gauss at the $k \sim 1$ Mpc^{-1} scale today. This field might serve as a seed for cosmological magnetic fields.

4.1 An introduction to magnetic fields from cosmic string network

Cosmic strings are expected to affect physics at various scales [51]. There are a number of phenomena caused by cosmic strings, for instance, as gravitational signatures, primordial gravitational waves (PGWs) from cusps and kinks on infinite strings

and string loops [52, 53, 54, 55], gravitational lensing by strings (strong lensing [56] and microlensing [57]), CMB angular power spectra [32, 58], and so on. As non-gravitational signatures, the following are predicted: ultra-high energy cosmic rays from strings [59] and cusps on string loops via a scalar field [60], and radio bursts from kinks and cusps on strings via the gravitational Aharonov-Bohm effect [61, 62].

Because of the impact on physics, a number of studies exist that aim to place constraints on string tension μ which shows the string energy scale. As for CMB observations, cosmic strings induce CMB anisotropies of the order of $\Delta T/T \sim 4\pi G\mu$, where T is the CMB temperature, ΔT is its fluctuation, and G is the gravitational constant. As a result, the recent CMB temperature measurement by the Planck collaboration provides limits to the energy scale of cosmic strings [63]. Details of the limits depend on the models of the cosmic strings, for instance, $G\mu \leq 3.2 \times 10^{-7}$ for Abelian Higgs strings and $G\mu \leq 1.5 \times 10^{-7}$ for Nambu-Goto strings [63].

Large scale magnetic fields are ubiquitous in the universe in various structures such as in filaments [64] and in clusters of galaxies [65].The strength of magnetic fields is expected to be about $\sim 10^{-8}$ Gauss in filaments (based on the turbulence simulations [64]), and found to be $\sim 10^{-5}$ Gauss in clusters (based on Faraday rotation measurements [65]). It is convincing that these large scale magnetic fields are amplified by the dynamo mechanism from tiny, primordial seed fields. Recent gamma-ray observations have indicated the existence of magnetic fields even in cosmic voids [66]. The strength of magnetic fields are about 10^{-16} Gauss in Mpc scale as [66]. Because voids are far away from most of astrophysical objects, primordial magnetic fields, if any, may survive just as they are in such regions[67].

In this chapter, we investigate primordial magnetic fields induced by the cosmic string network. Previous works about the generation of primordial magnetic fields from cosmic strings include generation from the motion of wiggly strings [68], shock waves induced by cosmic strings [69, 70], the dynamical friction of strings' motion [71], and via the Harrison mechanism in the early universe [72]. Because of the conservation of vorticity, it is argued that primordial magnetic fields can hardly be produced by cosmic defects [72]. To reassess the generation of primordial magnetic fields from cosmic strings, we focus on the tight coupling relationship between photon and baryon fluids in the early universe and the anisotropic stress of photons. We see that generation of magnetic fields from the cosmic string network is possible if we consider up to second order in the tight coupling expansion including the anisotropic stress of photons. In order to calculate the time evolution of cosmic string networks

and their associated magnetic fields, we modified CMBACT [73]; this is the code used to calculate the evolution of the string network and CMB anisotropies from the cosmic string network following the "one scale model" [38, 39, 40].

In the section 2.3, we have described the model of the individual strings and the evolution of the string network. In the next section (section 4.2), we investigate magnetic fields generation from the string network by considering the tight coupling approximation between the photon and baryon fluids. In section 4.3, the method which accounts for the randomness of the strings' initial configuration is given. We then discuss evolution of the magnetic field spectrum before and after the recombination epoch in section 4.4. Finally, we summarize the features of the magnetic fields from the cosmic string network in section 4.5. Throughout this chapter, we assumed an homogeneous and isotropic expanding universe consistent with the Λ-CDM model as the background metric. We fixed the cosmological parameters to $h = 0.73$, $\Omega_m h^2 = 0.127$, $\Omega_b h^2 = 0.0223$, and $N_\nu = 3.04$, where $H_0 = 100h\mathrm{km/s/Mpc}$ is the Hubble constant, Ω_m and Ω_b are the density parameters of matter and baryon, and N_ν is the number of massless neutrinos.

4.2 Magnetic fields

Infinite strings can be the source of magnetic fields on large scales around the recombination era. In this section, we estimate the amplitude of the magnetic fields produced by the network made of infinite strings.

4.2.1 Vector mode perturbation

Here we take the Poisson gauge,

$$ds^2 = a^2(\eta)(-(1+2\psi)d\eta^2 + 2w_i d\eta dx^i + [(1-2\phi)\delta_{ij} + h_{ij}]dx^i dx^j). \tag{4.2.1}$$

In the same way as [74], using the vector projector tensor

$$\mathcal{O}_{ij}^{(\lambda)}(\hat{k}) = \frac{i\lambda}{\sqrt{2}}(\hat{k}_i e_j^{(\lambda)}(\hat{k}) + \hat{k}_j e_i^{(\lambda)}(\hat{k})), \tag{4.2.2}$$

we can denote the vector mode part of h_{ij} directly as

$$h_{ij} = \sum_{\lambda=\pm1} h_V^{(\lambda)} \mathcal{O}_{ij}^{(\lambda)}. \tag{4.2.3}$$

The evolution equation of the vorticity $\sigma = \dot{h}_V/k$ is given based on the Einstein equation by

$$\dot{\sigma}^{(\lambda)} + 2\mathcal{H}\sigma^{(\lambda)} = 8\pi G a^2 \Pi^{(\lambda)}/k. \tag{4.2.4}$$

Here $\lambda = \pm$ is the index of polarization, and $\Pi = \Theta_{ij}^{\rm tot}(k,\tau)\mathcal{O}_{ij}$ is the total anisotropic stress in the vector mode. In this chapter, we assume the infinite strings to be the sources of the vector mode perturbations.

In the vector mode, the Euler equation for the baryon fluid is given by

$$\dot{v}_b - \dot{\sigma} + \mathcal{H}(v_b - \sigma) = R\dot{\tau}(v_\gamma - v_b), \tag{4.2.5}$$

where v_γ and v_b are the velocities of photon and baryon fluids, respectively, ρ_γ and ρ_b are the energy densities of photon and baryon fluids, respectively, $R = 4\rho_\gamma/3\rho_b$ is the photon-baryon ratio, $\dot{\tau} = a\sigma_T n_e$ is the opacity of the Thomson scattering, σ_T is the Thomson scattering cross section, and n_e is the electron number density. The vector mode Boltzmann equations for the photon fluid are given by

$$\dot{v}_\gamma - \dot{\sigma} + \frac{k}{8}\Pi_\gamma = -\dot{\tau}(v_\gamma - v_b), \tag{4.2.6}$$

$$\dot{\Pi}_\gamma + \frac{8}{5}kI_3 - \frac{8}{5}kv_\gamma = -\dot{\tau}\left(\frac{9}{10}\Pi_\gamma - \frac{9}{5}E_2\right), \tag{4.2.7}$$

$$\dot{I}_l + k\frac{l}{2l+1}\left(\frac{l+2}{l+1}I_{l+1} - I_{l-1}\right) = -\dot{\tau}I_l \qquad (l \geq 3), \tag{4.2.8}$$

$$\dot{E}_l + \frac{(l+3)(l+2)l(l-1)}{(l+1)^3(2l+1)}kE_{l+1} - \frac{l}{2l+1}kE_{l-1} = -\dot{\tau}\left(E_l - \frac{2}{15}\xi\delta_{l2}\right) + \frac{2}{l(l+1)}kB_l, \tag{4.2.9}$$

$$\dot{B}_l + \frac{(l+3)(l+2)l(l-1)}{(l+1)^3(2l+1)}kB_{l+1} - \frac{l}{2l+1}kB_{l-1} = -\frac{2}{l(l+1)}kE_l, \tag{4.2.10}$$

where $\Pi_\gamma = 3I_2$ is the anisotropic stress of the photon fluid, I_l is the l-th order moment of the intensity, E_l and B_l are the l-th order moments of the polarization, and $\xi = 3I_2/4 + 9E_2/2$ [47].

As shown in [74], the topological defects induce v_γ and v_b from the vorticity σ. Then, the relative velocity between the photon and baryon fluids, $v_\gamma - v_b$, plays the main role in exciting the magnetic fields [75, 76]. The evolution of the relative velocity

and thus the evolution of the associated magnetic fields are driven by the strength of the coupling between the photon and baryon fluids. Therefore, the magnetic fields evolve differently before and after the epoch of recombination. Before recombination, a tight-coupling approximation can be applied to describe their evolution. However, after recombination, we need to solve the baryon fluid equation (4.2.5) and the full Boltzmann equations (4.2.6)∼(4.2.10). We do this numerically.

4.2.2 Tight-coupling approximation

In the early universe before recombination, photon and baryon fluids are tightly coupled to each other because of the frequent Thomson scattering. In that epoch, the opacity of the Thomson scattering $\dot{\tau}$ was very large and the tight-coupling parameter $k/\dot{\tau}$ takes a very small value ($k/\dot{\tau} \ll 1$). Therefore, we can expand the Boltzmann and the Einstein equations with the tight coupling parameter. This expansion is called the tight-coupling approximation (TCA). In [77], the authors considered magnetic field generation with no external source, and used the first order approximation for the photon's anisotropic stress $\Pi_\gamma^{(1)}$ and the second order approximation for the relative velocity between photon and baryon fluids $v_\gamma^{(2)} - v_b^{(2)}$. In the case where there is an external source, higher order TCA, such as $\Pi_\gamma^{(2)}$ and $v_\gamma^{(3)} - v_b^{(3)}$ are needed [74]. In this chapter, we consider the string network as the external source and we need to consider the higher order approximation.

Here we consider the TCA up to the third order in the conformal Newtonian gauge. In the TCA, we expand the relative velocity as $\delta v = v_\gamma - v_b = 0 + \delta v^{(1)} + \delta v^{(2)} + \delta v^{(3)} + ...$, where $\delta v^{(n)} \propto (k/\dot{\tau})^n$ is the n-th order expansion. Following [74], we find the TCA up to second order for Π_γ and up to third order for δv as,

$$\Pi_\gamma^{(1)} = \frac{32}{15}\left(\frac{k}{\dot{\tau}}\right) v_\gamma^{(0)},$$
$$\Pi_\gamma^{(2)} = \frac{32}{15}\left(\frac{k}{\dot{\tau}}\right) v_\gamma^{(1)} + \frac{176}{45}\left(\frac{k}{\dot{\tau}}\right)^2 \frac{1}{k}\left[\frac{\ddot{\tau}}{\dot{\tau}} v_\gamma^{(0)} - \dot{v}_\gamma^{(0)}\right], \tag{4.2.11}$$

$$\delta v^{(1)} = \left(\frac{k}{\dot{\tau}}\right) \frac{\mathcal{H}}{(1+R)k}(v_\gamma^{(0)} - \sigma^{(0)}), \tag{4.2.12}$$

$$\delta v^{(2)} = \left(\frac{k}{\dot{\tau}}\right) \frac{\mathcal{H}}{(1+R)k}(v_\gamma^{(1)} - \sigma^{(1)}) - \frac{4}{15}\left(\frac{k}{\dot{\tau}}\right)^2 \frac{1}{1+R} v_\gamma^{(0)}$$
$$- \left(\frac{k}{\dot{\tau}}\right)^2 \frac{\mathcal{H}(v_\gamma^{(0)} - \sigma^{(0)})}{(1+R)^2 k^2}\left(\frac{\mathcal{H}R}{1+R} + \frac{\dot{\mathcal{H}}}{\mathcal{H}} + \mathcal{H} + \frac{\dot{v}_\gamma^{(0)} - \dot{\sigma}^{(0)}}{v_\gamma^{(0)} - \sigma^{(0)}} - \frac{\ddot{\tau}}{\dot{\tau}}\right), \tag{4.2.13}$$

$$
\begin{aligned}
\delta v^{(3)} = & \left(\frac{k}{\dot{\tau}}\right)\frac{\mathcal{H}}{(1+R)k}(v_\gamma^{(2)}-\sigma^{(2)}) - \frac{4}{15}\left(\frac{k}{\dot{\tau}}\right)^2\frac{1}{1+R}v_\gamma^{(1)} \\
& - \left(\frac{k}{\dot{\tau}}\right)^2\frac{\mathcal{H}(v_\gamma^{(1)}-\sigma^{(1)})}{(1+R)^2k^2}\left(\frac{\mathcal{H}R}{1+R}+\frac{\dot{\mathcal{H}}}{\mathcal{H}}+\mathcal{H}+\frac{\dot{v}_\gamma^{(1)}-\dot{\sigma}^{(1)}}{v_\gamma^{(1)}-\sigma^{(1)}}-\frac{\ddot{\tau}}{\dot{\tau}}\right) \\
& + \frac{4}{15}\left(\frac{k}{\dot{\tau}}\right)^3\frac{\mathcal{H}}{(1+R)^2k}v_\gamma^{(0)} \\
& - \frac{2}{45k}\left(\frac{k}{\dot{\tau}}\right)^3\frac{1}{(1+R)^2}\left[(23+11R)\frac{\ddot{\tau}}{\dot{\tau}}v_\gamma^{(0)} - (17+11R)\dot{v}_\gamma^{(0)} - \frac{6v_\gamma^{(0)}\mathcal{H}R}{1+R}\right].
\end{aligned}
\tag{4.2.14}
$$

In this chapter, we assume that the strings are the only source of vorticity. In this case, the fact that $v^{(0)} = \sigma^{(0)}$ plays the most important role. Because of this, the first order TCA of the relative velocity is given as $\delta v^{(1)} = 0$. Therefore, $\delta v^{(2)} \sim (k/\dot{\tau})^2\sigma/(1+R)$ is the leading order of the TCA. In our numerical calculation, evolution equations are switched from the TCA to the full Boltzmann equations at the epoch of recombination. At this time, we need to calculate an accurate relative velocity $\delta v^{(2)} = v_\gamma^{(2)} - v_b^{(2)}$ via the Boltzmann equations. The junction conditions for $v_\gamma^{(2)}$ and $v_b^{(2)}$ at recombination are given by the following equations,

$$
\dot{v}_b^{(2)} - \dot{\sigma}^{(2)} + \mathcal{H}(v_b^{(2)} - \sigma^{(2)}) = R\dot{\tau}\delta v_{\rm TCA}^{(3)}, \tag{4.2.15}
$$

$$
\dot{v}_\gamma^{(2)} - \dot{\sigma}^{(2)} + \frac{k}{8}\Pi_\gamma^{(2)} = -\dot{\tau}\delta v_{\rm TCA}^{(3)}. \tag{4.2.16}
$$

Therefore we need $\delta v^{(3)}$ for an accurate calculation of $\delta v^{(2)}$ at the switching time [74] from the TCA to the full Boltzmann equations.

4.2.3 Magnetic field generation

The relative velocity between the photon and baryon fluids can induce magnetic fields [75, 76]. In the early universe, electrons move together with photons because of the frequent Thomson scattering. Because this scattering separates electrons from photons, electric fields are induced and their rotations generate magnetic fields via the Maxwell equations. The evolution equation of the magnetic fields is given by [75, 76, 50],

$$
\frac{1}{a}\frac{\mathrm{d}}{\mathrm{d}\eta}(a^2B^i) = \frac{4\sigma_T\rho_\gamma a}{3e}\epsilon^{ijk}\partial_k(v_{\gamma j} - v_{bj}) \ , \tag{4.2.17}
$$

where e is the elementary charge and ϵ^{ijk} is the Levi-Civita tensor. We can obtain the magnetic field spectrum by integrating (4.2.17) in Fourier space as

$$\left\langle a^4 B^i(\vec{k},\eta) B_i^*(\vec{k}',\eta)\right\rangle = \left(\frac{4\sigma_T}{3e}\right)^2 (\delta^{jl}\delta^{km} - \delta^{jm}\delta^{kl}) k_k k'_m \left\langle \int_0^\eta \mathrm{d}\eta' a^2(\eta')\rho_\gamma(\eta')\delta v_j(\vec{k},\eta') \times \int_0^\eta \mathrm{d}\eta'' a^2(\eta'')\rho_\gamma(\eta'')\delta v_l^*(\vec{k}',\eta'')\right\rangle. \tag{4.2.18}$$

To calculate the above ensemble average we need the unequal–time correlation $\langle \delta v(k,\eta')\delta v(k,\eta'')\rangle$ as a result of continuous generation of metric perturbation from cosmic strings. To obtain this, we perform a number of simulations using CMBACT and estimate the ensemble average directly from the simulations as

$$\left\langle \delta v_j(\vec{k},\eta')\delta v_l^*(\vec{k}',\eta'')\right\rangle = \frac{1}{N_r}\sum_{I=1}^{N_r} Q_{jl}(\hat{k})\delta v^{(I)}(k,\eta')\delta v^{(I)}(k,\eta'')(2\pi)^3\delta(\vec{k}-\vec{k}'), \tag{4.2.19}$$

where

$$Q_{jl}(\hat{k}) = \delta_{jl} - \hat{k}_j\hat{k}_l, \tag{4.2.20}$$

is the projection tensor and $N_r = 100$ is the number of realization (for details, see section 4.3). Substituting (4.2.19) and (4.2.20) into (4.2.18), we obtain the correlation function of the magnetic fields as [77]

$$\left\langle B^i(\vec{k},\eta)B_i(\vec{k}',\eta)\right\rangle = (2\pi)^3 S_B^{\mathrm{ave}}(k,\eta)\delta^{(3)}(\vec{k}-\vec{k}'), \tag{4.2.21}$$

where

$$a^4(\eta)\frac{k^3}{2\pi^2}S_B^{\mathrm{ave}}(k,\eta) = 2\frac{k^3}{2\pi^2}\left(\frac{4\sigma_T}{3e}\right)^2 k^2 \frac{1}{N_r}\sum_{I=1}^{N_r}\left[\int_0^\eta \mathrm{d}\eta'\ a^2(\eta')\rho_\gamma(\eta')\delta v^{(I)}(k,\eta')\right]^2. \tag{4.2.22}$$

The source of this spectrum is δv, which is driven by σ.

4.3 Method

Once the initial configuration of the string network and its evolution are fixed, the spectrum of the magnetic fields can be calculated as shown in section 4.2.

However, the string network has a random initial configuration, and individual strings decay at random. To see the statistical properties of the generated magnetic fields, we need to average out their randomness. For that, we prepare a number of

realizations for the string network and calculate the power spectrum (4.2.22) under each realization.

In practice, we realize the magnetic fields by repeatedly following the three steps listed below using CMBACT[73]:

1. Set a random initial configuration of the string network.
2. Compute the evolution of the energy–momentum tensor of the string network by considering random decay of the strings.
3. Calculate the magnetic field spectrum.

In the m-th realization, the m-th power spectrum $S_B^m(k,\eta)$ in (4.2.21) is calculated. Moreover, we can obtain the averaged power spectrum $S_B^{\rm ave}(k,\eta)$ as

$$S_B^{\rm ave}(k,\eta) = \frac{1}{N_{\rm r}} \sum_{I=1}^{N_{\rm r}} S_B^{(I)}(k,\eta), \tag{4.3.23}$$

where $N_{\rm r}$ is the number of realizations, and we fix $N_{\rm r} = 100$ in this chapter. Because each S_B^m has an initial configuration and evolution, the averaged power spectrum, $S_B^{\rm ave}(k,\eta)$, can not be divided into an initial power spectrum and common transfer functions. Therefore, to see the statistical properties of the generated magnetic fields, we need to calculate a number of spectra under different realizations and average them out as (4.3.23).

According to the above argument and calculating (4.2.22) numerically, we can obtain the power spectrum of the magnetic fields from the string network as shown in Fig.4.1 and Fig.4.2. Fig.4.1 shows magnetic field spectra before recombination when the TCA can be applied, whereas Fig.4.2 shows the spectra after recombination when the TCA is invalid.

4.4 Result & Discussion

In this section, we will give an analytical interpretation of the magnetic field spectrum arising from the string network. Here to understand the behavior of the spectrum, we investigate the evolution of magnetic fields separately before and after recombination.

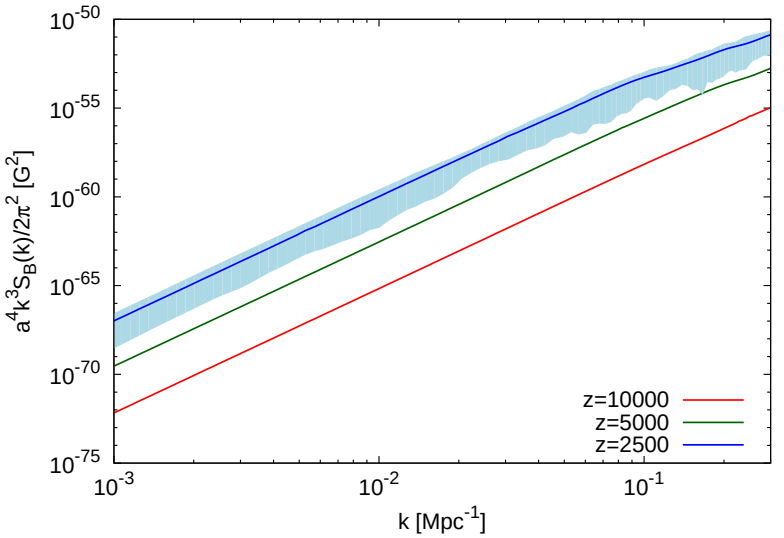

Figure.4.1 Power spectra of magnetic fields at $z = 10,000$ (red solid line), $5,000$ (green solid line), and $2,500$ (blue solid line) from the infinite string network with $G\mu = 1.1 \times 10^{-6}$. We averaged 100 realizations and the light-blue region is the 68% confidence interval for the $z = 2,500$ case. Under these redshifts, the TCA is valid.

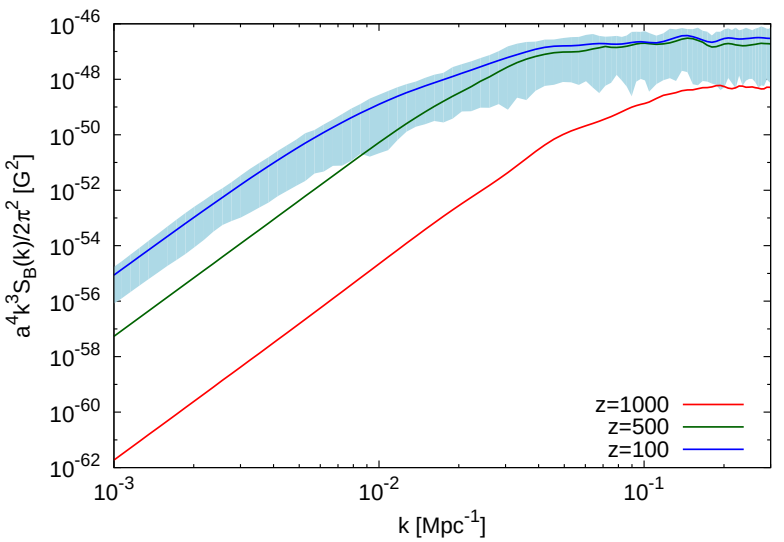

Figure.4.2 Same as Fig.4.1, but at $z = 1,000,\ 500,\ 100$. In these epochs, the TCA is invalid.

4.4.1 Before recombination

Before recombination, Thomson scattering between photons and electrons occurs frequently; therefore, we can use the TCA. Focusing on the vector mode that is

responsible for the generation of magnetic fields, all of the perturbations are induced by vorticity σ from the string network. This assumption leads the first order TCA of the relative velocity to be zero $\delta v^{(1)} = 0$; therefore, the second order TCA of the relative velocity $\delta v^{(2)}$ is the leading order of δv [74],

$$\delta v \approx \delta v^{(2)} \propto \left(\frac{k}{\dot{\tau}}\right)^2 \frac{v_\gamma^{(0)}}{1+R} = \left(\frac{k}{\dot{\tau}}\right)^2 \frac{\sigma^{(0)}}{1+R} = \begin{cases} k^2 a^5 \sigma^{(0)} & \text{(for rad. dominated era)} \\ k^2 a^4 \sigma^{(0)} & \text{(for mat. dominated era).} \end{cases} \tag{4.4.24}$$

Sourced by this relative velocity, magnetic fields are generated via (4.2.22) in individual realizations. Here we define the source function of the magnetic fields $F_s(k,\eta)$ as

$$F_s(k,\eta) \equiv \int_0^\eta \mathrm{d}\eta' \; a^2(\eta')\rho_\gamma(\eta')\delta v(k,\eta'). \tag{4.4.25}$$

Assuming $\sigma \propto a^\nu$, and integrating (4.2.4), we can find $\nu \geq -2$ is always valid once the anisotropic stress Π from the string network arises although the anisotropic stress is continuously generated by the active string network which makes its time-dependence nontrivial. Because of this, the value of ν varies between realizations. Then, substituting $\sigma \propto a^\nu$ and (4.4.24) into (4.4.25), we find that the source function $F_s(k,\eta)$ always increases with time. This means that the co-moving magnetic fields induced in this era are always increasing,

Following the above argument, we obtain a spectrum of the magnetic fields $S_B^{(I)}(k,\eta)$, which grows in time for each realization. Averaging these spectra in the manner explained in section 4.3, we calculate the averaged magnetic field power spectrum as shown in Fig.4.1. From Fig.4.1, we can find approximate expressions for the magnetic field spectrum. On super-horizon scales, the expression is given by

$$a^4(\eta)\frac{k^3}{2\pi^2}S_B^{\mathrm{ave}}(k,z) \approx 1.6\times 10^{-31}(G\mu)^2 \left(\frac{1+z}{1000}\right)^{-8.5} \left(\frac{k}{\mathrm{Mpc}^{-1}}\right)^7 \quad [\mathrm{G}^2], \tag{4.4.26}$$

and on sub-horizon scales,

$$a^4(\eta)\frac{k^3}{2\pi^2}S_B^{\mathrm{ave}}(k,z) \approx 5.8\times 10^{-34}(G\mu)^2 \left(\frac{1+z}{1000}\right)^{-7} \left(\frac{k}{\mathrm{Mpc}^{-1}}\right)^5 \quad [\mathrm{G}^2]. \tag{4.4.27}$$

On super horizon scales, we find that the wavenumber dependence is the same as that of the magnetic field spectrum from texture [74] and second order density perturbations [50, 46], but slightly different from the magnetic fields generated in Einstein-aether gravity $\left\langle B^2_{\mathrm{EA}}(k)\right\rangle \propto k^8$ [78]. The power spectrum of anisotropic stress arising from the string network is shown in Fig.4.3. On sub-horizon scales, we find the power

spectrum of magnetic fields as $k^3 S_B(k) \propto k^5$. To understand this scale dependence, we show the power spectrum of anisotropic stress arising from the string network in Fig.4.3. On sub-horizon scales, the spectrum shows $\Pi \propto k^{-1}$. From the equations (4.2.4) and (4.2.13) we find the relations $\sigma \propto \Pi/k$ and $\delta v \propto k^2\sigma$, which imply that $k^3 S_B(k) \propto k^5$ from (4.2.22). The wavenumber dependence differs from the other models which are given by $\left\langle B^2_{\rm NLSM}(k)\right\rangle \propto k^1$ [74], $\left\langle B^2_{\rm rec}(k)\right\rangle \propto k^2$ or $k^{2/3}$ [50] and $\left\langle B^2_{\rm EA}(k)\right\rangle \propto k^2$ or k^{-2} [78].

On smaller scales before recombination, δv begins to decay at the Silk damping scale. Here, the co-moving spectrum can be written as $\left\langle a^4 B^2(k,a)\right\rangle \propto k^5 a^{-7}$ and the Silk scale can be written as $k_{\rm Silk} \propto a^{-3/2}$ [79]. In the same way as [77], we obtain the power spectrum of magnetic fields at scales smaller than the Silk scale as $\left\langle a^4 B^2_{\rm Silk}(k)\right\rangle \propto k^{1/3}$. This spectrum continues to the horizon scale of electron positron pair annihilation, $k \sim 10^5 {\rm Mpc}^{-1}$, where the mechanism of magnetic field generation considered in this chapter ceases to function [77].

4.4.2 After recombination

Because the TCA was valid before recombination, we only needed the expression of δv up to $\delta v^{(2)}$ for the source of the magnetic fields. However, around recombination, as the number density of free electrons decreases, the frequency of the Thomson scattering between photons and electrons decreases. Moreover the photons and electrons gradually decouple. Then, the baryon fluid becomes less able to catch up with photon fluid and the TCA breaks down. After this switching epoch, to obtain δv, we need to calculate the full Boltzmann-Einstein system (4.2.4)$\sim$(4.2.10). In general, it is difficult to solve the Boltzmann equations and see the evolution of δv analytically. However, on super-horizon scales, we can estimate δv using the condition $k\eta \ll 1$. By integrating (4.2.5) and (4.2.6), baryon and photon fluids velocities can be denoted as

$$v_b(k,\eta) = \sigma(k,\eta) + \frac{1}{a(\eta)}\int^\eta d\eta' a(\eta')\dot\tau(\eta')R(\eta')\delta v(k,\eta') \tag{4.4.28}$$

$$= \sigma(k,\eta) + R(\eta)\int^\eta d\eta' \dot\tau(\eta')\delta v(k,\eta'), \tag{4.4.29}$$

$$v_\gamma(k,\eta) = \sigma(k,\eta) - \frac{k}{8}\int^\eta d\eta' \Pi_\gamma(k,\eta') - \int^\eta d\eta' \dot\tau(\eta')\delta v(k,\eta'). \tag{4.4.30}$$

From (4.4.28)$-$(4.4.30), we obtain the differential equation for δv,

$$\dot{\delta v} \simeq -\frac{k}{8}\Pi_\gamma(k,\eta) - \dot\tau(\eta)\delta v(k,\eta'), \tag{4.4.31}$$

where we neglected the second term on the RHS of (4.4.28) since $R(\eta) = 4\rho_\gamma/3\rho_b \ll 1$ after recombination. We solve it to obtain the form of $\delta v(k,\eta)$

$$\delta v(k,\eta) \simeq -\frac{k}{8} e^{-\tau(\eta)} \int^{\eta} d\eta' \Pi_\gamma(k,\eta') e^{\tau(\eta')}. \tag{4.4.32}$$

Writing the anisotropic stress of photons from (4.2.7) as,

$$\Pi_\gamma(k\eta) \sim \frac{8}{5} k \int^{\eta} d\eta' v_\gamma(k,\eta'), \tag{4.4.33}$$

we can estimate δv using v_γ as

$$\delta v(k,\eta) \sim -k^2 e^{-\tau(\eta)} \int^{\eta} d\eta' e^{\tau(\eta')} \int^{\eta'} d\eta'' v_\gamma(k,\eta''). \tag{4.4.34}$$

Substituting (4.4.33) and (4.4.34) into (4.4.30), we can see that $v_\gamma(k,\eta) = \sigma(k,\eta) + \mathcal{O}((k\eta)^2)$. Because of this, δv on super-horizon scales should be

$$\delta v(k,\eta) \sim -k^2 e^{-\tau(\eta)} \int^{\eta} d\eta' e^{\tau(\eta')} \int^{\eta'} d\eta'' \sigma(k,\eta''). \tag{4.4.35}$$

After vorticity σ becomes source free, σ evolves as $\sigma \propto a^{-2}$ and the source function (4.4.25) becomes constant. Then, the evolution of the magnetic fields finishes at super-horizon scales.

On sub-horizon scales, the same argument as that for the super-horizon holds true, and we can see the same relationship between δv and v_γ as in (4.4.34). The main difference in this case is the effects of the higher order terms in $k\eta$. On sub-horizon scales ($k\eta \geq 1$), the photon fluid velocity v_γ evolves following not the first but the second and third terms on the RHS of (4.4.30) (higher order terms in $k\eta$). Subsequently, after the recombination epoch, the third term vanishes and the evolution of v_γ follows the free-streaming solution. Then, the conformal time dependence of (4.4.34) is up to $\delta v \propto \eta^2$, and the generation of magnetic fields finishes.

In each realization, magnetic fields are induced by this mechanism. As before, because the evolution of magnetic fields varies in realizations, we need to take the realization average as in section 4.3. The averaged magnetic field power spectrum after recombination is given in Fig.4.2. We can see that the anisotropic stress induced by the string network is independent of the wavenumber k on the super-horizon scale from Fig.4.3. Using (4.2.4), (4.2.22) and (4.4.35), the wavenumber power on the super-horizon scale is the same as that before recombination, $\left\langle B^2(k) \right\rangle \propto k^7$. The expression of the magnetic field spectrum today can be written as

$$a^4(\eta) \frac{k^3}{2\pi^2} S_B^{\rm ave}(k,z) \approx 7 \times 10^{-23} (G\mu)^2 \left(\frac{k}{\rm Mpc^{-1}} \right)^7 \quad [\rm G^2], \tag{4.4.36}$$

on super-horizon scales and,

$$a^4(\eta)\frac{k^3}{2\pi^2}S_B^{\rm ave}(k,z) \approx 2.5\times 10^{-35}(G\mu)^2 \quad [{\rm G}^2], \tag{4.4.37}$$

on sub-horizon scales at $z = 100$ as shown in Fig.4.2.

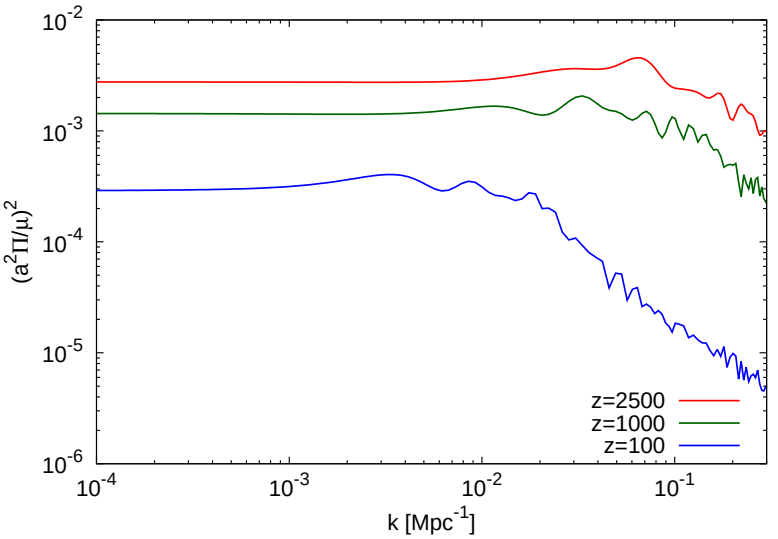

Figure.4.3 Wavenumber dependence of the anisotropic stress at $z = 2500$ (red solid line), 1000 (green solid line), 100 (blue solid line) from the infinite string network.

Finally let us discuss implications of these magnetic fields. If such magnetic fields existed in the early universe, strong magnetic amplification would occur in the accretion shocks of primordial gases during structure formation of the universe. Then they could provide extra pressure and suppress the fragmentation of gas clumps, supporting the formation of massive protostars and super massive black holes [80]. Moreover, they would affect the hyperfine structure of neutral hydrogens in primordial gases and might be observed via the anisotropic power spectrum of the brightness temperature of the 21-cm line with future surveys as discussed in [81].

4.5 Conclusion

In this chapter, we estimated the magnetic field spectrum from the cosmic string network. First, we calculated the evolution of the cosmic string network under the process of the one scale model and its energy momentum tensor using CMBACT [73]. Then, we solved the Boltzmann-Einstein system to obtain the relative velocity be-

tween the photon and baryon fluids using the tight coupling approximation and saw that the leading order of TCA for δv was $\mathcal{O}((k/\dot{\tau})^2)\sigma$ before recombination. Finally, we obtained the power spectrum of the magnetic fields via (4.2.22), before recombination, as $a^2\sqrt{B^2(k,z)} \sim 4\times10^{-16}G\mu/((1+z)/1000)^{4.25}(k/\mathrm{Mpc}^{-1})^{3.5}$ Gauss on super-horizon scales, and $a^2\sqrt{B^2(k,z)} \sim 2.4\times10^{-17}G\mu/((1+z)/1000)^{3.5}(k/\mathrm{Mpc}^{-1})^{2.5}$ Gauss on sub-horizon scales in co-moving coordinates. On scales smaller than the Silk damping scale, the spectrum could be calculated as $a^2\sqrt{B^2(k)} \propto k^{1/6}$. After recombination, the spectrum was driven by the evolution of vorticity on super-horizon scales and the coupling between photon and baryon fluids on sub-horizon scales. When the recombination epoch came to an end, the evolution of magnetic fields also ceased. The magnetic field spectrum today is $a^2\sqrt{B^2(k,z)} \sim 2\times10^{-11}G\mu(k/\mathrm{Mpc}^{-1})^{3.5}$ Gauss on super-horizon scales and $a^2\sqrt{B^2(k,z)} \sim 5\times10^{-17}G\mu$ Gauss on sub-horizon scales.

Chapter.5

Primordial magnetic fields from self-ordering scalar fields

A symmetry-breaking phase transition in the early universe could have led to the formation of cosmic defects. Because these defects dynamically excite not only scalar and tensor type cosmological perturbations but also vector type ones, they may serve as a source of primordial magnetic fields. In this study, we calculate the time evolution and the spectrum of magnetic fields that are generated by a type of cosmic defects, called global textures, using the non-linear sigma (NLSM) model. Based on the standard cosmological perturbation theory, we show, both analytically and numerically, that a vector mode relative velocity between photon and baryon fluids is induced by textures, which inevitably leads to the generation of magnetic fields over a wide range of scales. We find that the amplitude of the magnetic fields is given by $B \sim 10^{-9}((1+z)/10^3)^{-2.5}\,(v/m_{\rm pl})^2\left(k/{\rm Mpc}^{-1}\right)^{3.5}/\sqrt{N}$ Gauss in the radiation dominated era for $k \lesssim 1$ Mpc^{-1}, with v being the vacuum expectation value of the O(N) symmetric scalar fields. By extrapolating our numerical result toward smaller scales, we expect that $B \sim 10^{-14.5}\left((1+z)/10^3\right)^{1/2}(v/m_{\rm pl})^2\left(k/{\rm Mpc}^{-1}\right)^{1/2}/\sqrt{N}$ Gauss on scales of $k \gtrsim 1$ Mpc^{-1} at redshift $z \gtrsim 1100$. This might be a seed of the magnetic fields observed on large scales today.

5.1 An introduction to magnetic fields from self-ordering scalar fields

There exist many studies regarding the phenomenological aspects of topological defects, which include the generation of CMB temperature and polarization anisotropies

[82, 83, 84, 85], gravitational waves (GWs)[45, 86, 44, 87, 88], cosmic rays [89, 90], and some non-gravitational effects [91, 92], among others (for a review of structure formation with topological defects, see [93]). As a rule of thumb, the amplitude of the fluctuations induced by topological defects, such as CMB anisotropies, is of the order $\Delta T/T \sim 4\pi G v^2$, where v is the vacuum expectation value (VEV) of the scalar fields, G is the Newton constant, and T and ΔT are the CMB temperature and its fluctuation, respectively. Therefore, the recent CMB measurement by the Planck satellite has placed limits on the energy scale of the topological defects [63]. The actual limits depend on the detailed models, for instance, $Gv^2 \leq 4.2 \times 10^{-7}$ [94] for cosmic strings, $Gv^2 \leq 3.2 \times 10^{-7}$ for Abelian–Higgs cosmic strings, $Gv^2 \leq 1.5 \times 10^{-7}$ for Nambu–Goto strings, and $Gv^2 \leq 1.1 \times 10^{-6}$ for semi-local strings and global textures [63].

In this chapter, we pay particular attention to global textures with $N \gg 4$, which can be well-approximated by self-ordering scalar fields that follow the non-linear sigma model (NLSM). The NLSM can describe the evolution of global $O(N)$ symmetric scalar fields with an accuracy up to corrections on the order of $1/N$. The NLSM has attracted much attention since the discovery of CMB B-mode polarizations by the BICEP2 experiment [95] because textures following the NLSM can be a source of the scale-invariant GWs [96][44][45], just as inflation in the early universe can produce the scale-invariant GWs. To observationally distinguish between GWs originating from inflation and from textures, one should consider observables that reflect the time evolution of the GWs. The GWs from inflation are frozen on super-horizon scales at first, and decay with oscillations after the horizon crossing. The GWs from textures, on the other hand, are generated inside the horizon, and decay with oscillations after the scalar fields that source the GWs decay away as the universe expands. In [97], the authors calculate the CMB temperature and polarization anisotropies in the NLSM and find that the shapes of the correlation functions of the CMB anisotropies in the NLSM are different from the corresponding ones from inflation. Therefore, detailed observations of CMB anisotropies can distinguish between GWs from the two different origins. In fact, the recent B-mode measurement by BICEP2 places an upper bound on the VEV in the NLSM at $v \lesssim 9 \times 10^{-4} G^{-1/2}$, and the GWs from the NLSM are shown to be slightly disfavored by the data compared with those from inflation [98][99], while contamination by dust in the BICEP2 data has to be re-analyzed with PLANCK data.

In this chapter, we investigate yet another route to probe the NLSM: the generation of magnetic fields. Because of the non-linear nature of the NLSM, scalar

fields following the NLSM inevitably induce vector mode perturbations as well as scalar and tensor modes ones. The relative vector mode velocity between photon and baryon fluids induces rotation in electric fields, leading to the generation of magnetic fields [77]. Recent discoveries of large-scale magnetic fields in void regions [66][100] as well as magnetic fields at high redshifts [101] make the investigation more interesting because such magnetic fields may be of primordial origin in the early universe. Therefore, one of the aims of this chapter is to derive the spectrum of magnetic fields generated by vector perturbations in the NLSM within the observational limits of CMB anisotropies.

We already reviewed the NLSM, in which N-component scalar fields act as a source of cosmological perturbations, in section 2.4. Then, this chapter is organized as follows. In the next section, we derive the power spectrum of magnetic fields in the NLSM, both numerically and analytically, using the tight coupling approximation. We will see that in order to obtain a reliable result, we should expand the equations up to the third order in the tight coupling approximation between photon and baryon fluids. We discuss the result and give an analytic interpretation of the spectrum of the magnetic fields in section 4, followed by our conclusion in section 5. Throughout this chapter, we fix the cosmological parameters to $h = 0.7$, $\Omega_b h^2 = 0.0226$, $\Omega_{\rm c} h^2 = 0.112$, and $N_\nu = 3.046$, where $H_0 = 100h$ km/s/Mpc is the Hubble constant, Ω_b and $\Omega_{\rm c}$ are the density parameters of baryonic and cold dark matter, respectively, and N_ν is the effective number of massless neutrinos. Those parameter values are consistent with the Planck results, and correspond to the ΛCDM model [102].

5.2 Magnetic fields

In this section, we investigate generation of seeds of large scale magnetic fields from the self-ordering scalar fields which follow the NLSM. These scalar fields can induce cosmological vector mode perturbations and eventually produce magnetic fields.

5.2.1 Vector mode perturbations and their evolution equations

We begin by reviewing the basic linear perturbation theory and define the vector mode. Let us consider the perturbed metric around the flat FRW one in the

synchronous gauge as

$$ds^2 = g_{\mu\nu}dx^\mu dx^\nu = a^2(\eta)(-d\eta^2 + (\delta_{ij} + h_{ij})dx^i\ dx^j), \tag{5.2.1}$$

where h_{ij} is the metric perturbation. In Fourier space, the vector part of h_{ij} can be expressed as

$$h_{ij} = \frac{i\hat{k}_i h_j^V + i\hat{k}_j h_i^V}{\sqrt{2}}. \tag{5.2.2}$$

Here h_i^V is a divergenceless vector and can be rewritten using the vector basis $e_i^{(\pm)}(\hat{k})$ as

$$h_i^V = \sum_{\lambda=\pm} \lambda h_V^{(\lambda)} e_i^{(\lambda)}(\hat{k}). \tag{5.2.3}$$

Combining eq. (5.2.2) and eq. (5.2.3), we can denote h_{ij} directly as

$$h_{ij} = \sum_{\lambda=\pm} h_V^{(\lambda)} \mathcal{O}_{ij}^{(\lambda)}, \quad \mathcal{O}_{ij}^{(\lambda)} = \frac{i\lambda}{\sqrt{2}}(\ \hat{k}_i e_j^{(\lambda)}(\hat{k}) + \hat{k}_j e_i^{(\lambda)}(\hat{k})\ ), \tag{5.2.4}$$

where $\mathcal{O}_{ij}^{(\lambda)}$ is the vector projection tensor. Using this projection tensor, we can derive the vector mode perturbation equation for $\sigma = \dot{h}_V/k$ as

$$\dot{\sigma}^{(\lambda)} + 2\mathcal{H}\sigma^{(\lambda)} = 8\pi G a^2 \Pi^{(\lambda)}/k, \tag{5.2.5}$$

where $\Pi^{(\lambda)} = T_{ij}^{(\mathrm{tot})} \mathcal{O}_{ij}^{(\lambda)}$ is the total anisotropic stress in the vector mode,$\mathcal{H} = \dot{a}/a$ is conformal hubble, and a dot denotes a conformal time derivative. Hereafter we shall omit the superscript (λ) for the purpose of presentation. The total energy-momentum tensor consists of two parts: one is from the ordinary matter and radiation and the other is from the scalar fields given by eq. (2.4.91). Anisotropic stress of the scalar fields $\Pi^\phi = T_{ij}^\phi \mathcal{O}_{ij}$ can be calculated as

$$a^2\Pi^\phi(\vec{k},\eta) = \frac{v^2}{2}\int \frac{\mathrm{d}^3p}{(2\pi)^3}\frac{\mathrm{d}^3q}{(2\pi)^3}\sqrt{1-\mu^2}\,[k-2q\mu]\,q\,F(q,p,\eta)\beta_a(\vec{p})\beta_a(\vec{q})(2\pi)^3\delta(\vec{k}-\vec{p}-\vec{q}), \tag{5.2.6}$$

where $\mu = \hat{k}\cdot\hat{q}$ and $p = \sqrt{k^2 - 2kq\mu + q^2}$. For the expression of anisotropic stress of ordinary matter and radiation, we refer to, e.g., ref. [22]. Let us define the transfer function for the anisotropic stress of the scalar fields as

$$a^2\pi^\phi(k,q,\mu,\eta) \equiv \frac{v^2}{2}\sqrt{1-\mu^2}\,[k-2q\mu]\,q\ F(q,p,\eta), \tag{5.2.7}$$

and the transfer function for σ as

$$\sigma(k,q,\mu,\eta) = \frac{4\pi}{a^2(\eta)}\frac{v^2}{m_{\mathrm{pl}}^2}\int^\eta d\eta'\ a^2(\eta')\sqrt{1-\mu^2}\,[k-2q\mu]\,q\ F(q,p,\eta')/k. \tag{5.2.8}$$

The fluid equation for baryon in the vector mode is given by

$$\dot{v}_b + \mathcal{H} v_b = \frac{4\rho_\gamma}{3\rho_b} a n_e \sigma_T (v_\gamma - v_b), \tag{5.2.9}$$

where ρ_γ and ρ_b are the energy densities of photon and baryon fluids, respectively, $R = 4\rho_\gamma/3\rho_b$, σ_T is the Thomson scattering cross section, n_e is the electron number density, and $a n_e \sigma_T = \dot{\tau}$ is the opacity of the Thomson scattering. On the other hand, the vector mode Boltzmann equation of photon fluid expanded in terms of multipole momenta is given by

$$\dot{v}_\gamma + \frac{1}{8} k \Pi_\gamma = -\dot{\tau}(v_\gamma - v_b), \tag{5.2.10}$$

$$\dot{\Pi}_\gamma + \frac{8}{5} k I_3 - \frac{8}{5} k v_\gamma = -\dot{\tau}\left(\frac{9}{10}\Pi_\gamma - \frac{9}{5} E_2\right) + \frac{8}{5} k\sigma, \tag{5.2.11}$$

$$\dot{I}_l + k \frac{l}{2l+1}\left(\frac{l+2}{l+1} I_{l+1} - I_{l-1}\right) = -\dot{\tau} I_l \qquad (\text{for } l \geq 3), \tag{5.2.12}$$

for intensity and

$$\dot{E}_l + \frac{(l+3)(l+2)l(l-1)}{(l+1)^3(2l+1)} k E_{l+1} - \frac{l}{2l+1} k E_{l-1} = -\dot{\tau}\left(E_l - \frac{2}{15}\zeta \delta_{l2}\right) + \frac{2}{l(l+1)} k B_l, \tag{5.2.13}$$

$$\dot{B}_l + \frac{(l+3)(l+2)l(l-1)}{(l+1)^3(2l+1)} k B_{l+1} - \frac{l}{2l+1} k B_{l-1} = -\frac{2}{l(l+1)} k E_l, \tag{5.2.14}$$

for polarization. Here v_γ and Π_γ are the velocity and anisotropic stress of photons, respectively, I_l is the l-th order moment of photons' distribution, and E_l and B_l are the photons' polarization moments and $\zeta \equiv 3I_2/4 + 9E_2/2$ [47].

As we shall show in section 5.2.2, the relative velocity between the photon and baryon fluids plays the key role in generation of magnetic fields. Since the strength of the coupling between photon and baryon velocities significantly changes before and after recombination, evolution of the relative velocity and hence the magnetic fields qualitatively differs between these two epochs. Before recombination, the tight-coupling approximation allows us to solve the system of equations partially, which we shall see shortly, and helps us to interpret numerical results. On the other hand, after recombination, the system of equations is solved completely numerically.

Tight-coupling approximation

In the early universe, photon and baryon fluids are tightly coupled because the opacity of the Thomson scattering $\dot{\tau}$ is very large. Therefore we can expand the perturbation equations in section 5.2.1 in terms of the tight-coupling parameter $k/\dot{\tau} \ll 1$.

This is called the tight coupling approximation (TCA). In ordinary analyses without external sources such as the NLSM, the first order solution for anisotropic stress of photons $\Pi_g^{(1)}$ and the second order solution for the relative velocity between the photon and baryon fluids $\delta v^{(2)} = v_\gamma^{(2)} - v_b^{(2)}$ were used [77]. However, when there exist NLSM scalar fields as an external source in the linearized Boltzmann system, we find that one should consider the TCA up to the third order terms proportional to σ, as discussed below.

In the tight coupling expansion, the baryon velocity relative to the photon velocity is expanded using the tight coupling parameter, i.e., $v_\gamma - v_b = 0 + \delta v^{(1)} + \delta v^{(2)} + \ldots$, where $\delta v^{(1)}$ and $\delta v^{(2)}$ are proportional to $(k/\dot{\tau})$ and $(k/\dot{\tau})^2$, respectively. The tight coupling solutions of Π_γ and δv up to the second order are given by

$$\begin{aligned}
\Pi_\gamma^{(1)} =& \frac{32}{15}\left(\frac{k}{\dot{\tau}}\right)(v_\gamma^{(0)} + \sigma^{(0)}), \\
\Pi_\gamma^{(2)} =& \frac{32}{15}\left(\frac{k}{\dot{\tau}}\right)(v_\gamma^{(1)} \\
&+\sigma^{(1)}) + \frac{176}{45}\left(\frac{k}{\dot{\tau}}\right)^2 \frac{1}{k}\left[\frac{\ddot{\tau}}{\dot{\tau}}(v_\gamma^{(0)} + \sigma^{(0)}) - (\dot{v}_\gamma^{(0)} + \dot{\sigma}^{(0)})\right]
\end{aligned} \tag{5.2.15}$$

$$\delta v^{(1)} = \left(\frac{k}{\dot{\tau}}\right)\frac{\mathcal{H}}{(1+R)k} v_\gamma^{(0)} \tag{5.2.16}$$

$$\begin{aligned}
\delta v^{(2)} =& \left(\frac{k}{\dot{\tau}}\right)\frac{\mathcal{H}}{(1+R)k} v_\gamma^{(1)} - \frac{4}{15}\left(\frac{k}{\dot{\tau}}\right)^2 \frac{1}{1+R}(v_\gamma^{(0)} + \sigma^{(0)}) \\
&- \left(\frac{k}{\dot{\tau}}\right)^2 \frac{\mathcal{H} v_\gamma^{(0)}}{(1+R)^2 k^2}\left(\frac{\mathcal{H}R}{1+R} + \frac{\dot{\mathcal{H}}}{\mathcal{H}} + \mathcal{H} + \frac{\dot{v}_\gamma^{(0)}}{v_\gamma^{(0)}} - \frac{\ddot{\tau}}{\dot{\tau}}\right)
\end{aligned} \tag{5.2.17}$$

It is imporant to note that $\delta v^{(2)}$ is not necessarily smaller than $\delta v^{(1)}$ in the NLSM. This is because, in the NLSM, the metric perturbation σ is always much larger than the fluid perturbation variables such as v_γ (see figure 5.1 and discussion in section 5.3), and it sometimes happens that the first order solution proportional to v_γ is smaller than the second order solution proportional to σ i.e. $(k/\dot{\tau})v_\gamma \lesssim (k/\dot{\tau})^2\sigma$. We can see directly this relation from (5.2.10), which implies

$$v_\gamma \sim k\int d\eta \frac{k}{\dot{\tau}}\sigma \sim k\eta\left(\frac{k}{\dot{\tau}}\right)\sigma. \tag{5.2.18}$$

Therefore, the condition that $(k/\dot{\tau})v_\gamma \lesssim (k/\dot{\tau})^2\sigma$ is satisfied at least on super-horizon scales, and the slip term is dominated by the second order terms in the tight coupling approximation.

In fact, in the numerical calculations, we must eventually switch to evaluate the slip term directly from v_γ and v_b because the tight coupling approximation breaks down in late times. Because the slip term is dominated by the second order term $\delta v^{(2)}$ in early times, we must keep solving v_γ and v_b accurate enough up to the second order in the tight coupling approximation, i.e., $v_\gamma^{(2)}$ and $v_b^{(2)}$. In terms of the tight coupling approximation, the evolution equation of $v_\gamma^{(2)}$, for instance, is given by

$$\dot{v}_\gamma^{(2)} = -\frac{1}{8}k\Pi_\gamma^{(2)} - \dot{\tau}\delta v^{(3)} \ . \tag{5.2.19}$$

This is why we need to consider TCA up to the third order. The slip term at the third order is given by

$$\begin{aligned}\delta v^{(3)} = &\left(\frac{k}{\dot{\tau}}\right)\frac{\mathcal{H}}{(1+R)k}v_\gamma^{(2)} - \frac{4}{15}\left(\frac{k}{\dot{\tau}}\right)^2\frac{1}{1+R}(v_\gamma^{(1)}+\sigma^{(1)}) \\ &-\left(\frac{k}{\dot{\tau}}\right)^2\frac{\mathcal{H}v_\gamma^{(1)}}{(1+R)^2k^2}\left(\frac{\mathcal{H}R}{1+R}+\frac{\dot{\mathcal{H}}}{\mathcal{H}}+\mathcal{H}+\frac{\dot{v}_\gamma^{(1)}}{v_\gamma^{(1)}}-\frac{\ddot{\tau}}{\dot{\tau}}\right) \qquad (5.2.20) \\ &+\frac{4}{15}\left(\frac{k}{\dot{\tau}}\right)^3\frac{\mathcal{H}}{(1+R)^2k}\sigma^{(0)} \\ &-\frac{2}{45k}\left(\frac{k}{\dot{\tau}}\right)^3\frac{1}{(1+R)^2}\left[(23+11R)\frac{\ddot{\tau}}{\dot{\tau}}\sigma^{(0)} - (17+11R)\dot{\sigma}^{(0)} - \frac{6\sigma^{(0)}\mathcal{H}R}{1+R}\right]. \qquad (5.2.21)\end{aligned}$$

Here we show only the terms proportional to σ. The condition $\delta v^{(3)} \ll \delta v^{(2)}$ is always valid in the tight coupling regime.

5.2.2 Magnetic field generation

We consider generation of magnetic fields originated from the relative velocity between the photon and baryon fluids, $\delta v = v_\gamma - v_b$. Well before recombination, due to the frequent Thomson scattering of photons off electrons, electrons are separated with protons, and move together with photons. For protons to catch up with electrons, electric fields are induced and rotation of the induced electric fields generates magnetic fields via Maxwell equations.

The equation for the generation of magnetic fields is given by [50]

$$\frac{1}{a}\frac{\mathrm{d}}{\mathrm{d}\eta}(a^2B^i) = \frac{4\sigma_T\rho_\gamma a}{3e}\epsilon^{ijk}\partial_k(v_{\gamma j} - v_{bj}), \tag{5.2.22}$$

where e is the elementary charge and ϵ^{ijk} is the Levi-Civita tensor. The appearance of the rotation of δv in eq. (5.2.22) clearly shows that only the vector mode part of

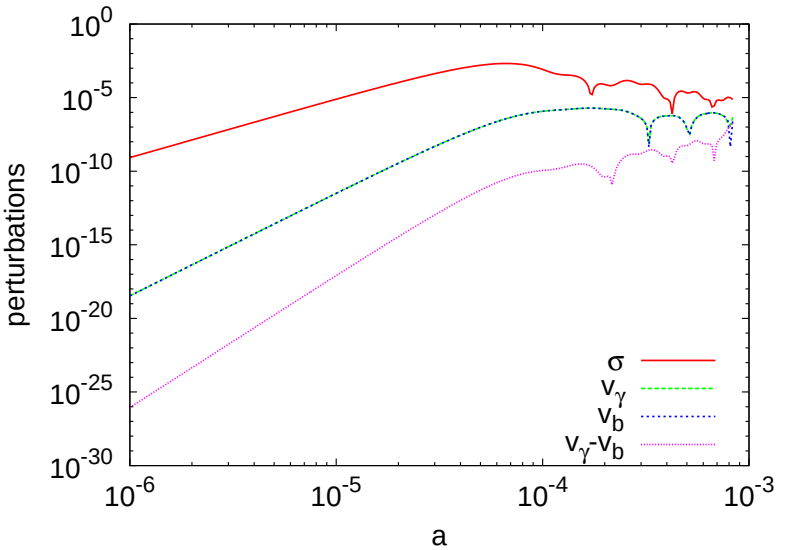

Figure.5.1 Time-evolutions of the transfer functions. Here $\sigma(k,q,\mu,\eta)$ (red line), $v_\gamma(k,q,\mu,\eta)$ (green), $v_b(k,q,\mu,\eta)$ (blue) and $\delta v(k,q,\mu,\eta)$ (magenta) are plotted as functions of the scale factor. We assume $k = q = 10^{-1}\mathrm{Mpc}^{-1}$ and, $\mu = 0$. We can see that the condition $\sigma \gg v_\gamma$ is almost always satisfied.

δv can contribute to magnetic fields. By integrating eq. (5.2.22) in Fourier space, we obtain

$$a^4 B^i(\vec{k},\eta)B_i^*(\vec{k}',\eta) = \left(\frac{4\sigma_T}{3e}\right)^2 (\delta^{jl}\delta^{km} - \delta^{jm}\delta^{kl})k_k k'_m \int_0^\eta \mathrm{d}\eta' a^2(\eta')\rho_\gamma(\eta')\delta v_j(\vec{k},\eta') \times \int_0^\eta \mathrm{d}\eta'' a^2(\eta'')\rho_\gamma(\eta'')\delta v_l^*(\vec{k}',\eta''). \tag{5.2.23}$$

Next we take an ensemble average of this expression over the initial configuration of the NLSM scalar fields $\beta_a(\vec{k})$. The ensemble average of the relative velocity can be calculated using the transfer function $\delta v(k,q,\mu,\eta)$ and the NLSM's initial power spectrum $\mathcal{P}^N_{\mathrm{ini}}$ defined in appendix 2.4.1 as

$$\left\langle \delta v_j(\vec{k},\eta')\delta v_l^*(\vec{k}',\eta'')\right\rangle = P_{jl}(\hat{k})\frac{\mathcal{P}^N_{\mathrm{ini}}}{2\pi^2}(2\pi)^3\delta(\vec{k}-\vec{k}') \times \int dq\ q^2 \int d\mu\ \delta v(k,q,\mu,\eta')\delta v(k,q,\mu,\eta''), \tag{5.2.24}$$

$$P_{jl}(\hat{k}) = \delta_{jl} - \hat{k}_j\hat{k}_l. \tag{5.2.25}$$

The correlation function of magnetic fields is then obtained as

$$\left\langle B^i(\vec{k},\eta)B_i^*(\vec{k}',\eta)\right\rangle = (2\pi)^3 S_B(k,\eta)\delta(\vec{k}-\vec{k}'), \tag{5.2.26}$$

where

$$a^4(\eta)\frac{k^3}{2\pi^2}S_B(k,\eta) = \frac{k^3}{2\pi^2}\left(\frac{4\sigma_T}{3e}\right)^2 \frac{\mathcal{P}^N_{\rm ini}}{\pi^2}k^2 \int dq\ q^2 \int_{-1}^{1} d\mu \times \left[\int_0^\eta {\rm d}\eta'\ a^2(\eta')\rho_\gamma(\eta')\delta v(k,q,\mu,\eta')\right]^2 . \qquad (5.2.27)$$

We calculate eq. (5.2.27) numerically and the power spectra of magnetic fields at several redshifts are depicted in figure 5.2.

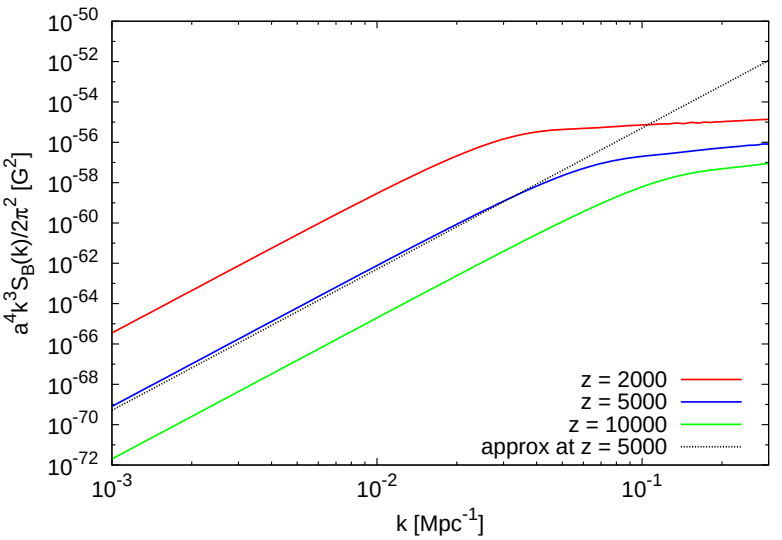

Figure.5.2 Power spectra of magnetic fields at $z = 2000$ (red solid line), $z = 5000$ (blue solid line) and $z = 10000$ (green solid line) from scalar fields in the NLSM. Here we take the NLSM parameters as $v^4/N = 10^{-12}m_{\rm pl}^4$. The black dotted line is the approximate amplitude which is given by eq. (5.3.45).

5.3 Analytical Understanding

Let us try to understand the results obtained in the previous section analytically. In our numerical calculations, we consider scalar fields following the NLSM as the only source of vector mode cosmological perturbations. Therefore we assume that there are no vector mode perturbations at $\eta \to 0$. In this setup, vorticity σ evolves first with the scalar fields as an external source (eq. (5.2.6)), and it induces photons' anisotropic stress Π_γ. Then Π_γ leads to the photon velocity v_γ and it propagates to the baryon velocity v_b. Because the induced anisotropic stress Π_γ is suppressed by a factor of the tight coupling parameter $k/\dot{\tau}$ due to the frequent Thomson scattering

(see eq. (5.2.15)), the velocities induced from the anisotropic stress are much smaller than σ, in other words, the condition that $\sigma \gg v_\gamma \sim v_b$ is valid at least in the tight coupling era. Therefore, we can find that the dominant term in eq. (5.2.17) is

$$\delta v(k,q,\mu,\eta) \approx -\frac{4}{15}\left(\frac{k}{\dot{\tau}}\right)^2 \frac{1}{1+R}\sigma(k,q,\mu,\eta). \tag{5.3.28}$$

To calculate $\sigma(k,q,\mu,\eta)$, we introduce approximations for the Bessel function in eq. (2.4.88) which are given by

$$\frac{J_\nu(x)}{x^\nu} \approx \begin{cases} \frac{1}{2^\nu \Gamma(\nu+1)} & (\text{for } x \ll 1) \\ \frac{1}{x^\nu}\sqrt{\frac{2}{\pi x}}\cos\left(x - \frac{2\nu+1}{4}\pi\right) & (\text{for } x \gg 1) \end{cases}. \tag{5.3.29}$$

Using these approximations, we can calculate super-horizon ($k\eta \ll 1$) and sub-horizon ($k\eta \gg 1$) solutions in the radiation and matter dominated eras as we shall show below.

5.3.1 Super-horizon

On super-horizon scales, the wavenumber of fluctuations k is smaller than the inverse of the horizon scale, i.e., $k\eta \ll 1$. However the wavenumber q in eq. (5.2.27) which comes from the convolution integral does not necessarily satisfy $q\eta \ll 1$. We know from eq. (5.2.7) and eq. (5.3.29) that $\sigma(k,q,\mu,\eta)$ as a function of q decays as $\sigma \propto q^{-2\nu+1}$ for $q \gg \eta^{-1}$, and we could expect that the bulk of the q-integration comes from the range of $q \lesssim \eta^{-1}$. In this case we can express eq. (5.2.27) as

$$a^4 \frac{k^3}{2\pi^2} S_B(k) \propto k^5 \eta^{-3} \left[\eta a^{-2} \delta v(k, q = 1/\eta, \mu, \eta)\right]^2. \tag{5.3.30}$$

For $k \ll q \sim p \sim 1/\eta$, we can find the k-dependence of σ from eq. (5.2.8) as,

$$\sigma \propto \frac{\eta^2}{k}. \tag{5.3.31}$$

Then, substituting eq. (5.3.28) and eq. (5.3.31) into eq. (5.3.30), we obtain

$$a^4 \frac{k^3}{2\pi^2} S_B(k) \propto k^5 \left[\frac{k^2}{k}\right]^2 \propto k^7. \tag{5.3.32}$$

We can see this power law tail on large scales in figure 5.2. The spectral index is same as that of the magnetic fields generated from second order density perturbations [50], but slightly different from the one obtained in the Einstein-aether gravity model, where $\sqrt{\langle B_{EA}^2(k)\rangle} \propto k^4$ [103].

5.3.2 Sub-horizon

On sub-horizon scales, i.e. $k\eta \gg 1$, the situation changes in a more complicated way. Because of the condition that $p\eta = \sqrt{k^2 - 2kq\mu + q^2}\eta \gg 1$, we must take special care of rapid oscillations of the Bessel functions in eqs.(5.2.8) and (5.2.27). In order to manipulate the equations analytically, we divide the interval of integration with wavenumber q into three regions: (i) $k \sim q \gg \eta^{-1}$; q is on sub-horizon scale, (ii) $q \ll \eta^{-1}$; q is on super-horizon scale, and (iii) $\eta^{-1} < q < \alpha\eta^{-1}$; q is nearly on the horizon scale (with α being $\mathcal{O}(1)$ constant). Considering contributions from each interval, we estimate the power spectrum of magnetic fields.

case (i) $k \sim q \gg \eta^{-1}$

In this case, because the conditions that $p\eta \gg 1$ and $q\eta \gg 1$ are satisfied from the conservation of the momentum, the source function of the vorticity σ has decayed away. Without sources, the vorticity also decays and therefore the contribution from this part is negligible.

case (ii) $q \ll \eta^{-1}$

In this case, $p \sim k$ and the source of the vorticity is growing. Using the approximation of eq. (5.3.29), and assuming the radiation dominated era ($\nu = 2$), we can evaluate eq. (5.2.8) as

$$\begin{aligned}\sigma &\propto \frac{1}{a^2}\int_0^{\eta'} d\eta''\ \eta''^5 q(1 - 2q\mu/k)\frac{J_\nu(k\eta'')}{(k\eta'')^\nu}, \\ &\propto \eta'^{-2}k^{-6}q(k\eta')^3 J_3(k\eta'). \end{aligned} \tag{5.3.33}$$

Here we use the fact that $1 - 2q\mu/k \simeq 1$ and the formula $\int dx\ x^{n+1}J_n(x) = x^{n+1}J_{n+1}(x)$, and ignore the factor $\sqrt{1-\mu^2}$. Using the above formula again and eq. (5.3.28), we obtain

$$\int_0^{\eta} d\eta'\ \rho_\gamma a^2 \delta v \propto k^{-6}q(k\eta)^4 J_4(k\eta). \tag{5.3.34}$$

Substituting eq. (5.3.34) into eq. (5.2.27) and using eq. (5.3.29), the spectrum can be written as

$$\begin{aligned} a^4\frac{k^3}{2\pi^2}S_B(k) &\propto k^5\int_0^{1/\eta} dq\ q^4\left[k^{-6}(k\eta)^4 J_4(k\eta)\right]^2 \\ &\propto k^0\ . \end{aligned} \tag{5.3.35}$$

case (iii) $\eta^{-1} < q < \alpha\eta^{-1}$

In this range, we need to treat the source carefully. First, assuming the radiation dominated era, let us divide the η' integral in eq. (5.2.27) as

$$\int_0^\eta a^2(\eta')\rho_\gamma(\eta')\delta v\, d\eta' \propto \int_0^\eta \eta'\sigma(\eta')d\eta' = \int_0^{q^{-1}} \eta'\sigma_{\eta'<q^{-1}}(\eta')d\eta' + \int_{q^{-1}}^\eta \eta'\sigma_{\eta'>q^{-1}}(\eta')d\eta' \,. \tag{5.3.36}$$

The integrand of the first term in the above equation, $\sigma_{\eta'<q^{-1}}(\eta')$, is given by eq. (5.3.33), and the integration leads to the term proportional to $k^{-6}q(k/q)^4 J_4(k/q)$. That of the second term is calculated as

$$\begin{aligned}\sigma_{\eta'>q^{-1}}(\eta') \simeq& \frac{1}{a^2}\int_0^{q^{-1}} d\eta'' \eta''^5 q(1-2q\mu/k)\frac{J_\nu(k\eta'')}{(k\eta'')^\nu} \\ &+\frac{1}{a^2}\int_{q^{-1}}^{\eta'} d\eta'' \eta''^5 q(1-2q\mu/k)\frac{J_\nu(k\eta'')}{(k\eta'')^\nu}\frac{J_\nu(q\eta'')}{(q\eta'')^\nu} \\ &\propto \eta'^{-2}k^{-6}[q(k/q)^3 J_3(k/q) + k^2 q^{-1}(k\eta')(J_3(k\eta')J_2(q\eta') + \mathcal{O}(q/k))]\end{aligned} \tag{5.3.37}$$

where we used $J_\nu(q\eta'')/(q\eta'')^\nu \simeq \mathcal{O}(1)$ for $q\eta'' \ll 1$, and omitted the constant factor of $\mathcal{O}(1)$.

Then the integration of δv can be calculated, by integrating by parts, as

$$\begin{aligned}\int_0^\eta d\eta'\ \rho_\gamma a^2 \delta v \propto \big[&k^{-6}q(k/q)^4 J_4(k/q) + k^{-4}q(k/q)^3 J_3(k/q)(\eta^2 - q^{-2}) \\ &+\ k^{-4}q^{-1}(k\eta)^2 J_4(k\eta)J_2(q\eta)\big]\,.\end{aligned} \tag{5.3.38}$$

Substituting the above equation into eq.(5.2.27) and ignoring the cross terms, we obtain,

$$\begin{aligned}a^4\frac{k^3}{2\pi^2}S_B(k) \propto k^5 \int_{1/\eta}^{\alpha/\eta} dq\ q^2\ \big[&k^{-12}q^2(k/q)^8 J_4^2(k/q) \\ &+\ k^{-8}q^2(k/q)^6 J_3^2(k/q)(\eta^2 - q^{-2})^2 + k^{-8}q^{-2}(k\eta)^4 J_4^2(k\eta)J_2^2(q\eta)\big]\,.\end{aligned} \tag{5.3.39}$$

Integrating with q, we find that the first, second, and the third terms in the above equation give terms $\propto k^0$, $\propto k^1$, and $\propto k^0$, respectively. Taking these terms together, we can find the k dependence of the magnetic field spectrum as

$$a^4\frac{k^3}{2\pi^2}S_B(k) \propto k[1 + \mathcal{O}(1/k\eta)]. \tag{5.3.40}$$

Therefore, in the radiation dominated era ($\nu = 2$), we find $a^4 k^3 S_B(k)/2\pi^2 \propto k$, which is confirmed in our numerical calculation. Finally, by reading off the numerical amplitude from the result of our numerical calculation we find the power spectrum of magnetic field on sub-horizon scales as

$$a^4 B^2 \sim \frac{10^{-44}}{(1+z)^3}\frac{1}{N}\left(\frac{v}{10^{-3}m_{pl}}\right)^4\left(\frac{k}{\mathrm{Mpc}^{-1}}\right)^1 \ [\mathrm{G}^2] \tag{5.3.41}$$

Similarly, we find $a^4 k^3 S_B(k)/2\pi^2 \propto k^{-1}$ in the matter dominated era ($\nu = 3$).

In figure 5.2, we find that the spectrum shows $k^3 S_B \propto k$ on small scales (say, $k \gtrsim 0.1$ Mpc^{-1}) in the radiation dominated era. At $z = 2000$ (the red solid line), the spectrum on sub-horizon scales shows the k dependence between the fully radiation dominated ($\propto k$) and matter dominated ones ($\propto k^{-1}$). On much smaller scales ($k \gg 1$ Mpc^{-1}) and in the matter dominated era, we expect that the spectrum of magnetic fields should be proportional to k because on those scales the source of vector perturbations has already decayed away and the magnetic fields just decay adiabatically after their creation deep in the radiation dominated era. From the fact that the generation mechanism is based on the mass difference between positively charged particles (protons) and negatively charged particles (electrons) and the small velocity slip between these particles, we expect that the spectrum continues up to the horizon scale at the epoch of $e^{\pm}$ annihilation $k \sim 10^5$ Mpc^{-1} and a cutoff at that scale [77].

5.3.3 Approximation at super-horizon scale

On super-horizon scales and in the radiation dominated era, we can estimate not only the shape of the spectrum but also the amplitude of magnetic fields approximately. On super-horizon scales the power spectrum of magnetic fields is given by

$$a^4(\eta)\frac{k^3}{2\pi^2}S_B(k,\eta) = \frac{k^3}{2\pi^2}\left(\frac{4\sigma_T}{3e}\right)^2\frac{\mathcal{P}^N_{\mathrm{ini}}}{\pi^2}k^2\int_0^{1/\eta} dq\ q^2\int_{-1}^{1} d\mu \times\left[\int_0^{\eta}\mathrm{d}\eta'\ a^2(\eta')\rho_\gamma(\eta')\delta v(k,q,\mu,\eta')\right]^2. \tag{5.3.42}$$

Substituting eq. (5.3.29) and eq. (5.2.7) to eq. (5.2.5) we get,

$$\sigma(k,q,\mu,\eta) \simeq -\frac{\pi A_\nu}{48}\sqrt{1-\mu^2}\mu\left(\frac{v}{m_{pl}}\right)^2\eta^4\frac{q^2}{k}, \tag{5.3.43}$$

where we assume $k \ll q \sim 1/\eta$. Using the above expression, we can write the velocity slip as

$$\delta v(k, q, \mu, \eta) \approx \frac{\pi A_\nu}{180} R^{-1} \dot{\tau}^{-2} \sqrt{1-\mu^2}\mu \left(\frac{v}{m_{pl}}\right)^2 \eta^4 q^2 k. \tag{5.3.44}$$

Substituting eq.(5.3.44) into eq.(5.3.42), we obtain

$$a^4(z)\frac{k^3}{2\pi^2} S_B(k, z) \sim \frac{10^{-3}}{(1+z)^9}\frac{1}{N}\left(\frac{v}{m_{pl}}\right)^4 \left(\frac{k}{\mathrm{Mpc}^{-1}}\right)^7 \ [\mathrm{G}^2], \tag{5.3.45}$$

in unit of Gauss at redshift $z \gg z_{\rm eq} \approx 3300$ [102]. This analytic power is plotted in figure5.2 to make a comparison with numerical results.

5.3.4 After recombination

In the above sections, we discussed magnetic field generation in the era when the tight coupling approximation is valid. Here we consider the era after the tight coupling approximation breaks down. In particular, we estimate when the magnetic fields become source-free on super-horizon scales, by considering the time evolution of the source function of magnetic fields $S(\eta) = \rho_\gamma a^2 \delta v q^{3/2}$, which satisfies $B^2 \propto [\int d\eta S]^2$.

On super-horizon scales ($k \ll \mathcal{H}$), the scalar fields with wavenumbers $q \sim \mathcal{H}$ have the biggest contribution to the source of vector perturbations and hence the magnetic fields. Thus we can set $q \sim 1/\eta$ in investigating the behavior of the source. When the tight coupling approximation is valid, i.e. $z \gg z_{\rm rec}$, we can estimate the time evolution of δv as

$$\delta v \ \propto \ k^2 \frac{\eta}{\dot{\tau}} \sigma \ \propto \ \eta^7, \tag{5.3.46}$$

from eq. (5.2.10) and eq. (5.2.11). Then after recombination, we can estimate $\delta v \approx v_\gamma$ from the same equations as

$$\delta v \propto \ k^2 \eta^2 \sigma \ \propto \ \eta^4. \tag{5.3.47}$$

Using these relations, the time evolution of the source term of magnetic fields before and after recombination can be derived as

$$S(\eta) = \rho_\gamma a^2 v_\gamma q^{3/2} \propto \begin{cases} \eta^{3/2} & \text{(before recombination)} \\ \eta^{-3/2} & \text{(after recombination)} \end{cases} . \tag{5.3.48}$$

Therefore, the evolution of magnetic fields becomes source-free after recombination. In fact, during recombination, δv is considerably enhanced and significant amount of magnetic fields is produced by the end of recombination $z \gtrsim 300$. For $z \lesssim 300$, the magnetic fields simply decay adiabatically. The spectrum of magnetic fields after recombination is depicted in figure 5.3.

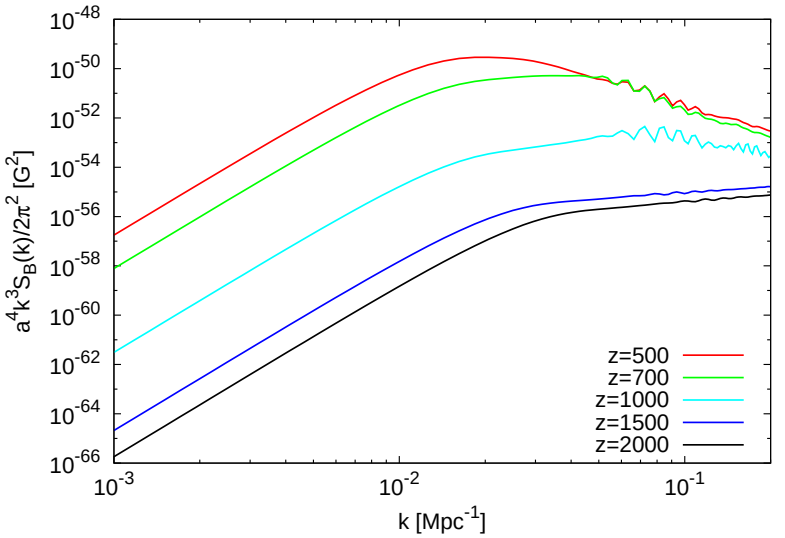

Figure.5.3 Power spectra of magnetic fields at $z = 2000$ (black solid line), 1500 (green solid line), 1000 (cyan solid line), 700 (green solid line), and 500 (red solid line) from scalar fields in the NLSM. Here we take the NLSM parameters as $v^4/N = 10^{-12} m_{\rm pl}^4$. The evolution of the spectrum comes to an end by $z = 300$.

5.4 Conclusion

In this chapter, we consider magnetic field generation from self-ordering scalar fields that follow the NLSM. We find that to reliably estimate the magnetic fields, one needs to expand the Boltzmann equations up to the third order terms in the tight coupling approximation. This is because the vorticity σ is very large so that $\mathcal{O}\left((k/\dot{\tau})v_\gamma\right) \sim \mathcal{O}\left((k/\dot{\tau})^3\sigma\right)$ in the tight coupling era (see figure.5.1) if the anisotropic stress of the scalar fields eq. (5.2.6) is an external source. By smoothly connecting the tight coupling solutions to the numerical ones we obtain the full magnetic field spectrum in the radiation dominated era and the matter dominated era, with an analytic interpretation of the results. In so doing, we see that the scalar fields with wavenumber $q \sim 1/\eta$ are the main source for both super-horizon ($k\eta \ll 1$) and sub-horizon ($k\eta \gg 1$) magnetic fields. By extrapolating our numerical result toward smaller scales analytically, we find $B \sim 10^{-22} \left(v/10^{-3} m_{pl}\right)^2 (1+z)^{1/2} \left(k/\mathrm{Mpc}^{-1}\right)^{1/2} /\sqrt{N}$ Gauss at $k \gtrsim 1$ Mpc^{-1} and $z \gtrsim z_{\rm rec}$. The strengths of magnetic fields smoothed at $\lambda = 1$ and 100 Mpc scales are $B_\lambda \sim 1.8 \times 10^{-25}$ and 4.5×10^{-26} Gauss, respectvely, where $B_\lambda^2 \equiv \int dk k^2 e^{-\lambda^2 k^2} S_B(k)/2\pi^2$. The energy density of magnetic

fields is $\rho_B \equiv \int dk k^2 S_B(k)/2\pi^2 \sim 1.2 \times 10^{-49}$ [G^2]. This might serve as a seed of large scale magnetic fields in the present universe.

Part.III

Gravitational waves radiation from cosmic string network

In this part, we will see gravitational waves from cosmic strings. There are two kinds of configuration of strings, namely loops and infinite strings. Both of them emit gravitational waves [3, 42, 104, 105, 106, 107, 108, 109, 110, 111, 53, 112, 113]. In this thesis, we focus on gravitational waves from kinks, which is sharp structures on cosmic infinite strings. Here we first introduce the gravitational waves in the cosmological perturbation theory, and kinks on infinite strings. Next we will see the gravitational waves from such kinks on the infinite string network.

Chapter.6

Preparation for gravitational waves from cosmic strings

In this chapter, we will introduce the primordial gravitational waves in standard cosmology, and the physics of kinks on infinite cosmic strings. In the next chapter, we combine them according to [3] and calculate gravitational waves from kinks on strings.

6.1 Primordial gravitational waves

Gravitational waves [11, 114, 115] are the metric perturbations in tensor mode perturbations (1.2.34). We can characterize their amplitude using the spectrum of tensor mode as

$$\left\langle h^T(\vec{k},\eta)h^{T*}(\vec{k}',\eta)\right\rangle = 2|h|^2(k,\eta)P^T_{\rm ini}(k)(2\pi)^3\delta(\vec{k}-\vec{k}'), \tag{6.1.1}$$

where the factor 2 is the number of tensor mode ($\sigma = \pm 2$), $|h|^2(k,\eta)$ is the square of the transfer function,

$$P^T_{\rm ini}(k)(2\pi)^3\delta(\vec{k}-\vec{k}') = \left\langle h^T_{\rm ini}(\vec{k})h^{T*}_{\rm ini}(\vec{k}')\right\rangle, \tag{6.1.2}$$

is the initial power spectrum of tensor mode and $|h|^2(k,\eta)P^T_{\rm ini}(k)$ corresponds to the squared amplitude of gravitational waves.

Here we consider primordial gravitational waves As a superposition of many stochastic, isotropic waves with a wide range of frequency. In standard cosmology, we define such primordial gravitational waves using the concept of density parameters (1.1.16) as

$$\Omega_{\rm GW}(k,\eta) = \frac{1}{\rho_{\rm crit,0}}\frac{d\rho_{\rm GW}}{d\ln k} = \frac{|\dot{h}|^2(k,\eta)k^3P^T_{\rm ini}(k)}{12\pi^2H_0^2a^2(\eta)}, \tag{6.1.3}$$

where

$$\begin{aligned}\rho_{\rm GW} =& \frac{\left\langle \dot{h}^T(\vec{x},\eta)\dot{h}^{T*}(\vec{x},\eta)\right\rangle}{32\pi G a^2(\eta)} \\ =& \frac{1}{32\pi G a^2(\eta)}\int \frac{d^3k}{(2\pi)^3}\frac{d^3k'}{(2\pi)^3}\sum_{\sigma=\pm 2}\left\langle \dot{h}_T^{(\sigma)}(\vec{k},\eta)\dot{h}_T^{(\sigma)*}(\vec{k}',\eta)\right\rangle e^{-i(\vec{k}-\vec{k}')\cdot\vec{x}} \\ =& \frac{1}{16\pi G a^2(\eta)}\int d\ln k \frac{k^3 P_{\rm ini}^T(k)}{2\pi^2}|\dot{h}|^2(k,\eta) \end{aligned} \tag{6.1.4}$$

is the energy density of the gravitational waves, $|h|^2(k,\eta)$ is the squared transfer function of tensor mode perturbation and dot $\dot{}$ denote the conformal time derivative. This expression is a convenient form to express the energy density of primordial gravitational waves. Considering the evolution of tensor mode perturbation $h(k,\eta)$, we can estimate the gravitational wave spectrum $\Omega_{\rm GW}(k,\eta)$.

6.2 Kinks on cosmic strings

Quadrupole motions of strings can induce tensor mode metric perturbations and they emit gravitational waves [11, 114, 115]. Here we focus on the continuous but undifferentiable (sharpened) points on cosmic strings which emit gravitational waves significantly [42, 52].

There are two kinds of such differential discontinuity on strings (see fig.6.1). One is called kinks, which are caused by reconnections of strings and they propagate on strings with blunting by cosmic expansion [42]. The other is called cusps, which are caused by the overlap of periodic modes on strings [42]. On the infinite strings, there are only kinks because infinite strings have no loop and there can not be cusps by periodic modes. The number of kinks are increased by collisions and reconnections of infinite strings. In contrast, there are both the differential discontinuities on string loops. When we consider wiggled strings, there are many periodic modes on string loops which produce cusps, and cusps can give dominant contribution to gravitational waves from loops.

Different types of strings produce gravitational waves at different scales [3, 55, 116, 104, 105, 106, 107, 108]. Infinite strings give the dominant contribution to GWs at the horizon scale of that epoch [3, 55]. On the contrary, string loops give the dominant contribution from cosmological scales to smaller scales [104, 105, 106, 107, 108, 56] because of their contraction caused by the gravitational radiation.

Here we want to focus on phenomena and observational signatures in cosmological

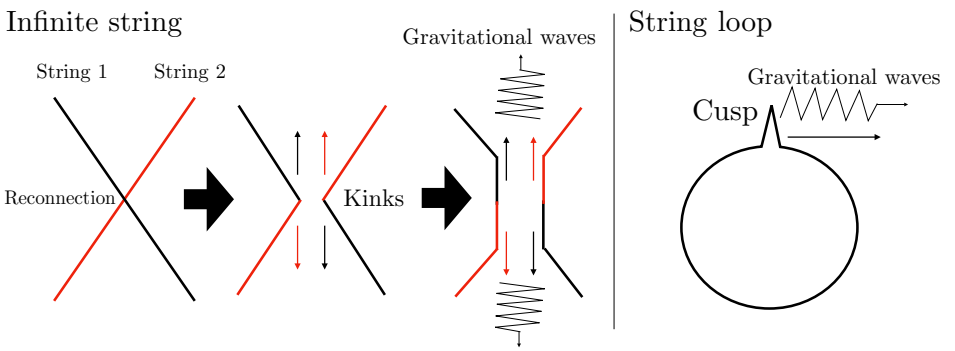

Figure.6.1 Images of kinks and a cusp on strings.

scales, and we will see the case of kinks on infinite strings hereafter.

6.2.1 A kink on the string

In this section, as a preparation for the next chapter, we will introduce the distribution of kinks on infinite strings. First let us see the wave modes on cosmic infinite strings, and define kinks and their sharpness in the Minkowski spacetime [28, 116] in which the metric is represented as $g_{\mu\nu} = \eta_{\mu\nu}$. We consider the equation of motion of the string on string worldsheet [32] using the action given by eq.(2.3.63). To fix the string worldsheet, we choose the gauge as

$$\frac{\partial \vec{x}}{\partial \zeta_1} \cdot \frac{\partial \vec{x}}{\partial \zeta_2} = 0, \tag{6.2.5}$$

$$\left(\frac{\partial \vec{x}}{\partial \zeta_1}\right)^2 + \left(\frac{\partial \vec{x}}{\partial \zeta_2}\right)^2 = 1. \tag{6.2.6}$$

In this gauge, we can obtain the following equation of motion,

$$\frac{\partial^2 \vec{x}}{\partial \zeta_1^2} - \frac{\partial^2 \vec{x}}{\partial \zeta_2^2} = 0. \tag{6.2.7}$$

We fix the coordinate (ζ_1, ζ_2) as (t, ξ), where t is the physical time and ξ is the space coordinate which runs along the string. Then the solution of the mode $\vec{x}$ is given by

$$\vec{x} = \frac{1}{2}\left(\vec{a}(\xi - t) + \vec{b}(\xi + t)\right), \tag{6.2.8}$$

where $\vec{a}(\xi - t)$ and $\vec{b}(\xi + t)$ are arbitrary functions called left and right moving mode, respectively, which satisfy

$$\left(\frac{\partial \vec{a}}{\partial \xi}\right)^2 = \left(\frac{\partial \vec{b}}{\partial \xi}\right)^2 = 1. \tag{6.2.9}$$

Hereafter let us discuss the feature of kinks on strings. Kinks are generated by collisions and reconnections between strings. Here we first consider collision and reconnection between two strings. At the time of collision, the strings reconnect each other at the collided point. Then the reconnected strings have the sharp structure called the kink. Here we focus on a reconnected point on the string as $(t, \xi) = (t_{\rm k}, \xi_{\rm k})$, where the kink exists, and we consider only the left moving mode, $\vec{a}(\xi - t)$ for the sake of simplicity. We can describe the left moving mode $\vec{a}(\xi - t)$ using $(t_{\rm k}, \xi_{\rm k})$ as

$$\vec{a}(\xi - t) = \vec{a}(\xi_{\rm k} - t_{\rm k}) \equiv \vec{a}(p_{\rm k}). \tag{6.2.10}$$

In the 'left side' $p_{\rm l}(\xi, t) = \xi - t < p_k$ and the 'right side' $p_{\rm r}(\xi, t) = \xi - t > p_k$, the left moving modes $\vec{a}(p_{\rm l})$ and $\vec{a}(p_{\rm r})$ come from different strings. The left moving mode itself $\vec{a}$ is continuous, but the tilt of the string $\partial\vec{a}/\partial\xi$ is discontinuous at the point of the kink $p_{\rm k}$ in general. Here we define the sharpness of the kink as

$$\psi = \frac{1}{2}(1 - \vec{a}'_{\rm l} \cdot \vec{a}'_{\rm r}), \tag{6.2.11}$$

where $\vec{a}'_{\rm l}$ and $\vec{a}'_{\rm r}$ are the tilts of the colliding strings

$$\vec{a}'_{\rm l} = \lim_{p_{\rm l} \to p_{\rm k}} \frac{\partial \vec{a}}{\partial \xi}(p_{\rm l}), \quad \vec{a}'_{\rm r} = \lim_{p_{\rm r} \to p_{\rm k}} \frac{\partial \vec{a}}{\partial \xi}(p_{\rm r}), \tag{6.2.12}$$

the inner product $\vec{a}'_{\rm l} \cdot \vec{a}'_{\rm r} = \cos\theta_{\rm k}$ corresponds to cosine of the angle $\theta_{\rm k}$ at the tip of the kink, and you can see that the sharpest kink is represented as $\psi = 1$ and the bluntest one is represented as $\psi = 0$.

Next let us consider the evolution of sharpness of a kink on a cosmic string in the homogeneous and isotropic expanding universe (2.3.62). We fix the gauge as eq.(6.2.5) and the coordinate (ζ_1, ζ_2) as (η, ξ), where η is the conformal time and ξ is the comoving space coordinate which runs along the string. We can obtain the equation of motion for modes on strings from the action (2.3.63) as,

$$\ddot{\vec{x}} + 2\mathcal{H}\dot{\vec{x}}(1 - \dot{\vec{x}}^2) = \frac{1}{\epsilon}\left(\frac{\vec{x}'}{\epsilon}\right)', \tag{6.2.13}$$

where ϵ is given in eq.(2.3.67), dot $\dot{}$ and prime $'$ denote the conformal time and the coordinate ξ derivatives, respectively. Here we define the alternatives of the left and right moving modes $\vec{a}$, $\vec{b}$ as

$$\vec{p}_{\pm} \equiv \dot{\vec{x}} \mp \frac{1}{\epsilon}\vec{x}', \tag{6.2.14}$$

where $\vec{p}_+$ and $\vec{p}_-$ satisfy

$$|\vec{p}_+|^2 = |\vec{p}_-|^2 = 1, \tag{6.2.15}$$

and these modes correspond to the tilt of the string which are given by $\vec{a}'$ in the Minkowski spacetime. Here we can rewrite the equation of motion (6.2.13) using $\vec{p}_+$ and $\vec{p}_-$ as

$$\dot{\vec{p}}_\pm \pm \frac{\vec{p}'_\pm}{\epsilon} = -\mathcal{H}\left(\vec{p}_\mp - (\vec{p}_+ \cdot \vec{p}_-)\vec{p}_\pm\right). \tag{6.2.16}$$

From the equation of motions for $\vec{p}_+$ and $\vec{p}_-$, we can see the scaler factor dependence of them as

$$\frac{\partial \vec{p}_+}{\partial(\epsilon\xi + \eta)} \propto \mathcal{H}, \tag{6.2.17}$$

$$\frac{\partial \vec{p}_-}{\partial(\epsilon\xi - \eta)} \propto \mathcal{H}, \tag{6.2.18}$$

where we make variable transformation from (ξ, η) to $(\epsilon\xi + \eta, \epsilon\xi - \eta)$. These variables go to zero in the Minkowski spacetime, in which $\epsilon = 1$ and $\mathcal{H} = 0$. These correspond to the equations of motions for the tilts of the left moving and right moving modes,

$$\frac{\partial \vec{a}'}{\partial(\xi + \eta)} = 0, \tag{6.2.19}$$

$$\frac{\partial \vec{b}'}{\partial(\xi - \eta)} = 0, \tag{6.2.20}$$

and therefore we can say $\vec{p}_+$ and $\vec{p}_-$ represent the tilts of left $\vec{a}'$ and right $\vec{b}'$ moving modes. Now we can define the sharpness of a kink on a string in the homogeneous and isotropic expanding universe as in the same way as eq.(6.2.11),

$$\psi = \frac{1}{2}(1 - \vec{p}_{+,\mathrm{l}} \cdot \vec{p}_{+,\mathrm{r}}), \tag{6.2.21}$$

where $\vec{p}'_{+\mathrm{l}}$ and $\vec{p}'_{+\mathrm{r}}$ are the left and right sides (like $\vec{a}'_{\mathrm{l}}$ $\vec{a}'_{\mathrm{r}}$) of the left moving mode $\vec{p}_+$. Here we have to remind that there are right moving modes as well and the sharpness of kinks produced by right moving modes can be represented as eq.(6.2.21) with replacing the subscript + to −.

Hereafter we will see the evolution of the sharpness ψ and its distribution on the string [117]. If we regard $\vec{p}_+$ and $\vec{p}_-$ as functions of variables $(\epsilon\xi - \eta, \eta)$ and $(\epsilon\xi + \eta, \eta)$, respectively, we can reduce the equation of motion eq.(6.2.16) to

$$\dot{\vec{p}}_\pm = -\mathcal{H}\left(\vec{p}_\mp - (\vec{p}_+ \cdot \vec{p}_-)\vec{p}_\pm\right). \tag{6.2.22}$$

Rewriting eq.(6.2.22) in the physical coordinate, we obtain

$$\frac{d\vec{p}_\pm}{dt} = -H\left(\vec{p}_\mp - (\vec{p}_+ \cdot \vec{p}_-)\vec{p}_\pm\right), \tag{6.2.23}$$

we then write eq.(6.2.23) as the equation of motion for the sharpness as

$$\frac{d\psi}{dt} = \frac{H}{2}\left(\vec{p}_- \cdot \vec{p}_{+,\mathrm{r}} + \vec{p}_- \cdot \vec{p}_{+,\mathrm{l}} - (\vec{p}_- \cdot \vec{p}_{+,\mathrm{r}})(\vec{p}_{+,\mathrm{l}} \cdot \vec{p}_{+,\mathrm{r}}) - (\vec{p}_- \cdot \vec{p}_{+,\mathrm{l}})(\vec{p}_{+,\mathrm{l}} \cdot \vec{p}_{+,\mathrm{r}})\right). \tag{6.2.24}$$

Considering the ensemble average of $\vec{p}_- \cdot \vec{p}_+$,

$$\langle \vec{p}_- \cdot \vec{p}_+ \rangle = -(1 - 2v^2) \equiv -\kappa, \tag{6.2.25}$$

we reduce eq.(6.2.24) to

$$\frac{d\psi}{dt} = -2\kappa H \psi. \tag{6.2.26}$$

Based on the simulation of cosmic string network [117], it is found that $\kappa_{\mathrm{r}} \approx 0.18$ and $\kappa_{\mathrm{m}} \approx 0.3$ in the radiation and matter dominated epochs, respectively. Then we can represent the sharpness ψ as the function of physical time,

$$\psi \propto t^{-2\zeta}, \tag{6.2.27}$$

where

$$\zeta \equiv \kappa \frac{d\ln a}{d\ln t} = \begin{cases} 0.09 & \text{(radiation dominated epoch)} \\ 0.2 & \text{(matter dominated epoch),} \end{cases} \tag{6.2.28}$$

becomes constant in the radiation and matter dominated epochs.

6.2.2 Distribution of kinks on strings

Here we introduce the sharpness distribution of kinks on infinite strings. The distribution of kinks is determined by three factors,
(i) production of kinks by collisions between infinite strings,
(ii) the sharpness of kinks blunted by the cosmic expansion,
(iii) kinks taken away by string loops.

First, let us discuss the contribution from (i), considering a collision between string 1 (st1) and string 2 (st2). The probability of a collision is given by the intersection probability of the infinitesimal regions of string worldsheet 1 dA_1 and string worldsheet 2 dA_2. Here we choose the coordinate of string worldsheets as $u = \xi - t$ and $s = \xi + t$, and the infinitesimal region on each worldsheet is written as $[u, u + du]$ times $[s, s + ds]$ (see fig.6.2). The probability of the collision is represented as

$$dP_{1,2} = \frac{d\Omega}{V dt}, \tag{6.2.29}$$

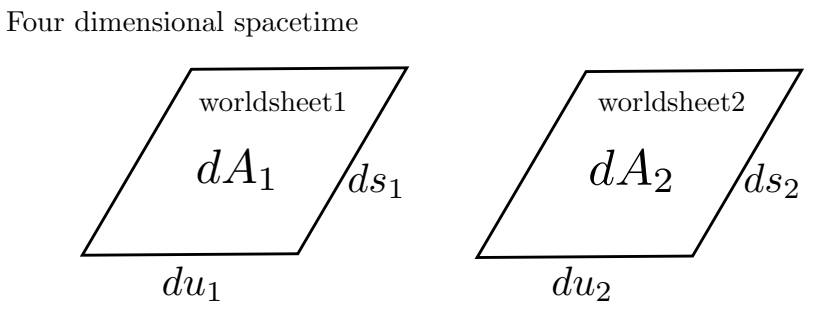

Figure.6.2 Rough illustrations of string worldsheets. dA_1 is the worldsheet for string 1 and dA_2 is the worldsheet for string 2.

where Vdt is the four dimensinal volume with the volume of space V, and $d\Omega$ is the four dimensional volume configured by dA_1 times dA_2, which is given by

$$d\Omega = \left|\sqrt{-\mathrm{det}g^{\mu\nu}}\epsilon_{\alpha\beta\gamma\delta}\frac{\partial x^\alpha}{\partial u_1}\frac{\partial x^\beta}{\partial s_1}\frac{\partial x^\gamma}{\partial u_2}\frac{\partial x^\delta}{\partial s_2}\right| du_1 ds_1 du_2 ds_2. \tag{6.2.30}$$

Because the areas of the worldsheets are smaller than the horizon scale $dA_1, dA_2 \ll H^{-2}$, the metric can be treated as the Minkowski spacetime $g_{\mu\nu} = \eta_{\mu\nu}$, and we can denote $d\Omega$ as

$$d\Omega = \frac{1}{4}\Delta(\vec{p}_{+,\mathrm{l}}, \vec{p}_{+,\mathrm{r}}, \vec{p}_{-,\mathrm{l}}, \vec{p}_{-,\mathrm{r}}) du_1 ds_1 du_2 ds_2 \tag{6.2.31}$$

where Δ is the products of $\vec{p}_\pm$,

$$\Delta(\vec{p}_{+,\mathrm{l}}, \vec{p}_{+,\mathrm{r}}, \vec{p}_{-,\mathrm{l}}, \vec{p}_{-,\mathrm{r}}) = \frac{1}{4}\left|(\vec{p}_{+,\mathrm{l}} \times \vec{p}_{+,\mathrm{r}}) \cdot (\vec{p}_{-,\mathrm{l}} - \vec{p}_{-,\mathrm{r}}) + (\vec{p}_{-,\mathrm{l}} \times \vec{p}_{-,\mathrm{r}}) \cdot (\vec{p}_{+,\mathrm{l}} - \vec{p}_{+,\mathrm{r}})\right|. \tag{6.2.32}$$

To calculate the collision probability $dP_{1,2}$, we consider the integration of $[du\ ds] = [2d\xi\ dt]$ and rewrite $\Delta(\vec{p}_{+,\mathrm{l}}, \vec{p}_{+,\mathrm{r}}, \vec{p}_{-,\mathrm{l}}, \vec{p}_{-,\mathrm{r}})$ using the sharpness ψ. Here we rewrite Δ by calculating (6.2.32) following [117],

$$\Delta(\vec{p}_{+,\mathrm{l}}, \vec{p}_{+,\mathrm{r}}, \vec{p}_{-,\mathrm{l}}, \vec{p}_{-,\mathrm{r}}) = \bar{\Delta}\int d\psi g(\psi), \tag{6.2.33}$$

where $\bar{\Delta}$ is the averaged $\Delta(\vec{p}_{+,\mathrm{l}}, \vec{p}_{+,\mathrm{r}}, \vec{p}_{-,\mathrm{l}}, \vec{p}_{-,\mathrm{r}})$ and $g(\psi)$ is the distribution function of sharpness produced by the collision. Considering up to the first order of $\vec{p}_+ \cdot \vec{p}_- < 1$,

we obtain

$$\begin{aligned}\bar{\Delta} =& \int \frac{d\vec{p}_{+,\mathrm{l}}}{4\pi}\frac{d\vec{p}_{+,\mathrm{r}}}{4\pi}\frac{d\vec{p}_{-,\mathrm{l}}}{4\pi}\frac{d\vec{p}_{-,\mathrm{r}}}{4\pi}\Delta(\vec{p}_{+,\mathrm{l}},\vec{p}_{+,\mathrm{r}},\vec{p}_{-,\mathrm{l}},\vec{p}_{-,\mathrm{r}}) \\ =& \frac{2\pi}{35}\left(1+\frac{2}{3}\kappa-\frac{1}{11}\kappa^2\right),\end{aligned} \tag{6.2.34}$$

and the distribution function $g(\psi)$ is given by

$$g(\psi) = \frac{35}{256}\sqrt{\psi}(15-6\psi-\psi^2), \tag{6.2.35}$$

where the domain of $g(\psi)$ is $0 \leq \psi \leq 1$. Then we can calculate the collision probability as

$$dP_{1,2} = \frac{\bar{\Delta}V}{L^4}dt, \tag{6.2.36}$$

where we integrate the length of strings in the volume V as $\int^V d\xi = L_V = V/L^2$ and L is the correlation length of strings. Because collisions make kinks, you can see that the number of collisions is equivalent to the number of kinks. We can represent the number of produced kinks in the volume V per unit time by collision as

$$dP_{1,2} = dN|_{\mathrm{produced}} = \frac{\bar{\Delta}V}{L^4}dt, \tag{6.2.37}$$

and the number of produced kinks per unit time and in the range of $[\psi, \psi+d\psi]$ is written as

$$\left.\frac{\partial N}{\partial t}(\psi,t)\right|_{\mathrm{produced}} d\psi = \frac{\bar{\Delta}V}{L^4}g(\psi)d\psi. \tag{6.2.38}$$

We now take into account the effects of the cosmic expansion. We consider the conservation of the total amount of kinks, up to the sharpness $\psi(t)$,

$$\frac{d}{dt}\left[\int^{\psi(t)} d\psi' N(\psi',t)\right] = \int^{\psi(t)} d\psi' \left[\frac{\partial N}{\partial t}(\psi',t) - \frac{2\zeta}{t}\frac{\partial}{\partial\psi'}\left(\psi' N(\psi',t)\right)\right] = 0, \tag{6.2.39}$$

and thus the equation

$$\frac{\partial N}{\partial t}(\psi',t) - \frac{2\zeta}{t}\frac{\partial}{\partial\psi'}\left(\psi' N(\psi',t)\right) = 0, \tag{6.2.40}$$

has to be satisfied. Here the blunting of kinks, the second term of the left hand side, $d\psi'/dt = -2\zeta\psi'/t$ comes from the cosmic expansion. Then we can represent the effects of the expansion for kinks as

$$\left.\frac{\partial N}{\partial t}(\psi,t)\right|_{\mathrm{blunt}} = \frac{2\zeta}{t}\frac{\partial}{\partial\psi}\left(\psi N(\psi,t)\right). \tag{6.2.41}$$

Next we will see the decrease of kinks on infinite strings. When strings collide each other, some string loops are produced and some kinks are taken away by string loops. Here the length of strings taken away by loops is given by [118, 119, 120],

$$\left.\frac{dL_V}{dt}\right|_{\rm loop} = -\eta_l \frac{V}{L^3} \tag{6.2.42}$$

where η_l is the product of the loop chopping efficiency and the root mean velocity of strings, $\eta_l = \tilde{c}v/2$, and it is related to the evolution of the string network (2.3.78). The fraction of amount of kinks which leaves infinite strings is written as

$$\left.\frac{1}{N}\frac{\partial N}{\partial t}\right|_{\rm loop} = \left.\frac{1}{L_V}\frac{dL_V}{dt}\right|_{\rm loop} = -\frac{\eta_l}{L}. \tag{6.2.43}$$

Finally, considering the three contributions eqs.(6.2.38), (6.2.41) and (6.2.43), we obtain the equation of motion for the distribution function of kinks on infinite strings as

$$\begin{aligned}\frac{\partial N}{\partial t}(\psi,t) =& \left.\frac{\partial N}{\partial t}(\psi,t)\right|_{\rm produced} + \left.\frac{\partial N}{\partial t}(\psi,t)\right|_{\rm blunt} + \left.\frac{\partial N}{\partial t}\right|_{\rm loop} \\ =& \frac{\bar{\Delta} V}{L^4} g(\psi) + \frac{2\zeta}{t}\frac{\partial}{\partial \psi}\left(\psi N(\psi,t)\right) - \frac{\eta_l}{L} N(\psi,t).\end{aligned} \tag{6.2.44}$$

Now we can calculate the evolution of the sharpness distribution of kinks on infinite strings in the volume V. Solving eq.(6.2.44) and the evolution of cosmic string network given by eqs.(2.3.78), (2.3.79), we obtain the distribution function of kinks. Then we calculate the gravitational waves from kinks distributed on infinite strings in the next chapter.

Chapter.7

Improved calculation of the gravitational wave spectrum from kinks on infinite cosmic strings

Gravitational wave observations provide unique opportunities to search for cosmic strings. One of the strongest sources of gravitational waves is discontinuities of cosmic strings, called kinks, which are generated at points of intersection. Kinks on infinite strings are known to generate a gravitational wave background over a wide range of frequencies. In this chapter, we calculate the spectrum of the gravitational wave background by numerically solving the evolution equation for the distribution function of the kink sharpness. We find that the number of kinks for small sharpness is larger than the analytical estimate used in a previous work, which makes a difference in the spectral shape. Our numerical approach enables us to make a more precise prediction on the spectral amplitude for future gravitational wave experiments.

7.1 Introduction

Cosmic strings continuously generate gravitational waves throughout the history of the universe after their formation. Gravitational wave bursts from different epochs and different directions overlap one another and form a gravitational wave background over a wide range of frequencies. Thus, gravitational wave experiments are expected to be a powerful tool to test the existence of cosmic strings. Various types of experiments can be used to probe the gravitational wave background at different frequencies: pulsar timing experiments [121, 122] measure gravitational waves at $\sim 10^{-8}$Hz; space

missions such as eLISA [123, 124] and DECIGO [125, 126] explore 10^{-3}Hz and 0.1Hz, respectively; ground-based experiments such as Advanced-LIGO [127], Advanced-VIRGO [128] and KAGRA [129] focus on $\sim$ 100Hz.

Gravitational wave signatures from cosmic strings have been extensively investigated in the literature [116, 130, 131, 132, 133]. It has been widely accepted that the string network evolves towards the scaling regime, where infinite strings continuously decay into loops and the string network keeps $\mathcal{O}(1)$ infinite strings per Hubble volume. Thus, the network consists of infinite strings and loops, both of which can be sources of gravitational waves. In refs. [52, 42], it has been suggested that non-smooth structures in strings, such as cusps and kinks, emit strong gravitational wave bursts. Cosmic string loops generically have cusps and kinks, and various works have shown that they generate a large gravitational wave background at high frequencies [42, 104, 105, 106, 107, 108, 109, 110, 111, 53, 112, 113]. While loops generate gravitational waves of wavelength shorter than the loop size, gravitational waves from infinite strings become important for long wavelength. The spectrum of the gravitational wave background originating from kinks on infinite strings are calculated in ref. [55].

In this chapter, we reexamine the spectrum of the gravitational wave background from kinks on infinite strings. Since the strength of gravitational wave bursts depends on the sharpness of kinks, we need to obtain the distribution function of the sharpness to calculate the spectrum. The evolution equation for the sharpness distribution is modeled in ref. [117], and ref. [55] calculated the spectrum by using analytic solutions of the differential equation for the distribution function. The analytic solutions are obtained separately for radiation-dominated (RD) and matter-dominated (MD) eras and the normalization for the RD era is chosen to have the same amplitude with the MD era at radiation-matter equality. Instead of using analytic solutions, we numerically solve the differential equation to obtain the sharpness distribution function, which enables us to smoothly connect the RD and MD eras. In fact, since the string network evolves differently in these eras [134, 120, 135, 136, 137, 138, 139, 140], the parameters in the differential equation differ for MD and RD. They should determine the normalization of the distribution function and our numerical method correctly takes into account these effects.

The change of the parameters at radiation-matter equality is taken into account in two different ways. First, we interpolate the values using the tangent hyperbolic function. Second, we calculate the time evolution of the parameters by using the

velocity-dependent one-scale (VOS) model [40]. In the first case, the values of the numerical parameters are set to be the same as the previous work, which makes the comparison easier and enables us to show the effect of their change at radiation-matter equality clearly. The second case enables us to follow the scaling law of the string network and provides more realistic time evolution of the parameters.

The outline of this chapter is as follows. In section 7.2, we briefly describe the methods to calculate the distribution function for the kink sharpness and gravitational wave background spectrum. In section 7.3, we perform the numerical calculation to evaluate the distribution function of kinks. Then, using the kink distribution, we calculate the spectrum of the gravitational wave background. In section 7.4, we make a comparison with previous works. Section 7.5 is devoted to conclusions.

7.2 Gravitational wave from kinks on the infinite strings

First, we review the dynamics of cosmic strings and describe the method to calculate the distribution function of kink sharpness and the power spectrum of the gravitational wave background.

7.2.1 Dynamics of cosmic strings

We consider cosmic strings in a spatially flat Friedmann-Lemaître-Robertson-Walker (FLRW) metric,

$$\mathrm{d}s^2 = a^2(\tau)\left(-\mathrm{d}\tau^2 + \mathrm{d}\boldsymbol{x}^2\right) = g_{\mu\nu}\mathrm{d}x^\mu \mathrm{d}x^\nu\,, \tag{7.2.1}$$

where $a(\tau)$ is the scale factor of the universe. A cosmic string is represented as a two-dimensional worldsheet in the four-dimensional spacetime. We choose the coordinates on the worldsheet as $\zeta^1 = \tau$ (conformal time), $\zeta^2 = \sigma$ (a direction along a cosmic string), and $\frac{\partial x^\mu}{\partial \tau}\frac{\partial x_\mu}{\partial \sigma} = 0$, then the action of the Nambu-Goto string is given by

$$S[x^\mu] = -\mu \int \mathrm{d}^2\zeta \sqrt{-\det(\gamma_{ab})}\,, \tag{7.2.2}$$

where μ is the tension of the string, $\gamma_{ab} = \frac{\partial x^\mu}{\partial \zeta^a}\frac{\partial x^\nu}{\partial \zeta^b} g_{\mu\nu}$ is the induced metric on the string worldsheet. Taking the variation of the action with respect to x^μ, we obtain the equation of motion for a cosmic string,

$$\frac{\partial^2 \boldsymbol{x}}{\partial \tau^2} + \frac{2}{a}\frac{\mathrm{d}a}{\mathrm{d}\tau}\frac{\partial \boldsymbol{x}}{\partial \tau}\left\{1 - \left(\frac{\partial \boldsymbol{x}}{\partial \tau}\right)^2\right\} = \frac{1}{\epsilon}\frac{\partial}{\partial \sigma}\left(\frac{1}{\epsilon}\frac{\partial \boldsymbol{x}}{\partial \sigma}\right)\,, \tag{7.2.3}$$

where

$$\epsilon \equiv \sqrt{\frac{(\partial \boldsymbol{x}/\partial\sigma)^2}{1-(\partial \boldsymbol{x}/\partial\tau)^2}}\,, \tag{7.2.4}$$

is interpreted as energy per unit σ, and we set $\epsilon = 1$ at the present time. When the Hubble friction is negligible, the equation has solutions of left and right propagating waves. Accordingly, we define the new variable $\boldsymbol{p}_\pm$ which corresponds to the left and right moving modes,

$$\boldsymbol{p}_\pm \equiv \frac{\partial \boldsymbol{x}}{\partial\tau} \mp \frac{1}{\epsilon}\frac{\partial \boldsymbol{x}}{\partial\sigma}\,. \tag{7.2.5}$$

7.2.2 Cosmic string network

Cosmic strings follow "scaling law" where the number of infinite strings conserves in the horizon. In the VOS model [40], the network evolution is characterized by the correlation length L. The total energy of a cosmic string and the average velocity are defined by

$$E = \mu a \int \mathrm{d}\sigma\epsilon \tag{7.2.6}$$

$$v^2 \equiv \frac{\int \mathrm{d}\sigma \left(\frac{\partial \boldsymbol{x}}{\partial\tau}\right)^2 \epsilon}{\int \mathrm{d}\sigma\epsilon}, \tag{7.2.7}$$

Then, the energy density $\rho_{\rm inf}$ of infinite strings is defined as

$$\rho_{\rm inf} = \frac{\mu}{L^2}. \tag{7.2.8}$$

Using the physical time t, which relates to the conformal time as $\mathrm{d}t = a\mathrm{d}\tau$, the evolution equations of the correlation length and velocity are

$$\frac{\mathrm{d}L}{\mathrm{d}t} = HL(1+v^2) + \frac{1}{2}cpv, \tag{7.2.9}$$

$$\frac{\mathrm{d}v}{\mathrm{d}t} = (1-v^2)\left(\frac{k}{L} - 2Hv\right), \tag{7.2.10}$$

where $k(v) \equiv \frac{1}{v(1-v^2)}\frac{\int \mathrm{d}\sigma\left\{1-(\mathrm{d}\boldsymbol{x}/\mathrm{d}\tau)^2\right\}(\mathrm{d}\boldsymbol{x}/\mathrm{d}\tau)\cdot\boldsymbol{u}\epsilon}{\int \mathrm{d}\sigma\epsilon} \simeq \frac{2\sqrt{2}}{\pi}\frac{1-8v^6}{1+8v^6}$ and $\boldsymbol{u}$ is a unit vector parallel to the curvature radius vector, and H is the Hubble parameter $H = \frac{\mathrm{d}a/\mathrm{d}t}{a}$. The second term of the right hand of (7.2.9) is the energy transmitted to loops per unit time, p is a probability of reconnection and c is the loop chopping efficiency parameter which is set $c \simeq 0.23$ [141]. With $\gamma \equiv L/t$, the first equation is rewritten as

$$\frac{\mathrm{d}\gamma}{\mathrm{d}t} = \frac{1}{t}\left\{-\gamma + H\gamma t(1+v^2) + \frac{1}{2}cpv\right\}. \tag{7.2.11}$$

By setting $\mathrm{d}\gamma/\mathrm{d}t$ and $\mathrm{d}v/\mathrm{d}t$ to be zero in (7.2.10) and (7.2.11), we obtain the asymptotic solutions

$$\gamma = \text{Const.},\ v = \text{Const.} \tag{7.2.12}$$

As we find the correlation length $L = \gamma t$ grows in proportion to t, the number of infinite strings is conserved in the horizon. The velocity keeps constant value for a fixed cosmic expansion rate.

7.2.3 Distribution function of kinks on infinite strings

Kinks are defined as discontinuities in the string tangent vector $\boldsymbol{x}$. They are produced by reconnection between cosmic strings and propagate along strings. The sharpness of the kink is defined by

$$\psi \equiv \frac{1}{2}(1 - \boldsymbol{p}_{\pm,\,1} \cdot \boldsymbol{p}_{\pm,\,2})\,. \tag{7.2.13}$$

The subscript $\pm$ denotes the left and right moving modes, and $1/2$ represent the left/right side of the discontinuity, respectively. The range of sharpness is $0 \leq \psi \leq 1$ and a large value of ψ corresponds to a sharp kink.

Let us define $-\alpha \equiv \langle \boldsymbol{p}_+ \cdot \boldsymbol{p}_- \rangle = -(1 - 2v^2)$, where the bracket means ensemble average in the string network, v^2 is the mean square velocity of strings. Rewriting (7.2.5) and (7.2.13) in terms of ψ, we have [117]

$$\psi \propto t^{-2\zeta}\,, \tag{7.2.14}$$

where t is the proper time $t = \int a d\tau$ and $\zeta = \alpha\nu$. The parameter ν characterizes the evolution of the scale factor as $a \propto t^{\nu}$. The value of ζ in the MD era differs from the one in the RD era, as we provide in table 7.1.

Intersections in the cosmic string network continuously generate kinks on infinite strings. We define the distribution function of kinks as a function of the sharpness and proper time, $N(\psi,\, t)$, so that $N(\psi,\, t)d\psi$ is the number of kinks between ψ and $\psi + \mathrm{d}\psi$ within the volume V at proper time t. Then its time evolution is given by [117]

$$\frac{\partial N}{\partial t}(\psi,\, t) - \frac{2\zeta}{t}\frac{\partial}{\partial \psi}(\psi N(\psi,\, t)) = \frac{\bar{\Delta} V}{\gamma^4 t^4} g(\psi) - \frac{\eta}{\gamma t} N(\psi,\, t), \tag{7.2.15}$$

where $\bar{\Delta}$ is the probability of the intersection[142], γ characterizes the correlation length of the string network L as $L = \gamma t$, and η is the decrease rate of kinks due to the loop production which is determined from simulations [118]. The function $g(\psi)$

in (7.2.15) is the initial sharpness distribution, and given by

$$g(\psi) = \frac{35}{256}\sqrt{\psi}(15 - 6\psi - \psi^2)\,, \tag{7.2.16}$$

where we set $g(\psi) = 0$ for $\psi < 0$ or $1 < \psi$. When the left hand side of (7.2.15) equals to zero, the equation demonstrates that the number of kinks is conserved while the sharpness decreases as in (7.2.14). In the right hand side of (7.2.15), the first term denotes a production of kinks by intersection of strings, the second term denotes decreasing of the number of kinks by the loop production. This term can be obtained by considering the length of cosmic strings d transferred from infinite strings to loops,

$$\left.\frac{\dot{d}}{d}\right|_{\rm loop} = -\frac{\eta}{\gamma t}\,, \tag{7.2.17}$$

and we have assumed that the fraction of kinks taken away on loops is proportional to the loss of length, $\dot{d}/d \propto \dot{N}/N$.

	RD	MD
γ	0.31	0.50
ζ	0.09	0.2
$\bar{\Delta}$	0.20	0.21
η	0.18	0.1

Table.7.1 The values of the constant adopted in ref. [55] are summarized for RD and MD eras.

	RD	MD
γ	0.27	0.56
ζ	0.062	0.16
$\bar{\Delta}$	0.19	0.21
η	0.076	0.068

Table.7.2 The values of the constant for RD and MD eras obtained by solving the VOS equations.

To obtain the kink distribution using (7.2.15), we need the time evolution of γ, ζ, $\bar{\Delta}$, and η. In this chapter, we show results by using two different methods to obtain them. In the first case, we use the parameter values used in ref. [55] and we smoothly change them from RD to MD at radiation-matter equality $t_{\rm eq} \simeq 2.0 \times 10^{12}$s using

$$\chi(t) = \chi_m \frac{1 + \tanh(100\ln(t/t_{\rm eq}))}{2} + \chi_r \frac{1 - \tanh(100\ln(t/t_{\rm eq}))}{2}\,, \tag{7.2.18}$$

where χ_m and χ_r describe values for MD and RD. The values for RD and MD eras are listed in table 7.1. Using the same values with the previous work makes easier to see the effect of the parameter transitions at radiation-matter equality, which was not taken into account in the previous work.

In the second case, we calculate the time evolution of γ, ζ, $\bar{\Delta}$, and η by solving the VOS equations (7.2.10) and (7.2.11). The parameter values $\zeta, \eta, \bar{\Delta}$ are obtained from

v as

$$\zeta = \alpha\nu = (1-2v^2)\left(\frac{\ln(a/a_{\rm ini})}{\ln(t/t_{\rm ini})}\right), \tag{7.2.19}$$

$$\eta = \frac{1}{2}cpv\,, \tag{7.2.20}$$

$$\bar{\Delta} = \frac{2\pi}{35}\left\{1+\frac{2}{3}(1-2v^2)-\frac{1}{11}(1-2v^2)^2\right\}. \tag{7.2.21}$$

Table. 7.2 shows the asymptotic values of the parameters for RD and MD eras obtained by solving the VOS equations. As we can find by comparing the two tables, some of the parameter values are different from the previous work, and they affect the kink distribution as well as the amplitude of the gravitational wave background.

7.2.4 Gravitational waves from kinks

It has been shown in ref. [55] that the kinks which contribute the most to the power of gravitational waves with angular frequency ω satisfy the following condition:

$$\left(\psi\frac{N(\psi,\,t)}{V(t)/(\gamma t)^2}\right)^{-1} \sim \omega^{-1}. \tag{7.2.22}$$

We define the sharpness of kinks which satisfies (7.2.22) for a given frequency ω as $\psi_{\rm max}(\omega,\,t)$. This condition means that the main contribution on the gravitational wave background at physical frequency ω comes from kinks with sharpness $\psi_{\rm max}$ whose average
interval $(\psi N(\psi,\,t)/(V(t)/(\gamma t)^2))^{-1}$ is comparable with the wavelength of the gravitational waves ω^{-1}.

The strength of a gravitational wave burst from one kink on loops has been formalized in ref. [42]. Including the dependence on the sharpness ψ, the strain amplitude is given by

$$h(f,z) = \frac{G\mu[\psi_{\rm max}(\omega,z)]^{1/2}l}{[(1+z)fl]^{2/3}}\frac{1}{r(z)}\Theta(1-\theta_m), \tag{7.2.23}$$

where $\theta_m = [(1+z)fl]^{-1/3}$, $f = a\omega/(2\pi a_0)$ is the gravitational wave frequency today with $a_0 = 1$ being the present scale factor, r is the distance to the source $r(z) = \int_0^z dz/H(z)$, and l is twice the fundamental period $T_l = l/2$ of string loops. Since we consider infinite strings and their typical curvature is given by γt, l is replaced by the correlation length γt in our calculation. The step function $\Theta(1-\theta_m)$ is introduced to set a low-frequency cutoff, which reflects the fact that kinks do not emit gravitational waves larger than the horizon size. We calculate the Hubble parameter

using $H = H_0[\Omega_r(a/a_0)^{-4} + \Omega_m(a/a_0)^{-3} + \Omega_\Lambda]^{1/2}$, where Ω_r, Ω_m and Ω_Λ are the density parameters for radiation, matter, and the cosmological constant, respectively. We use $\Omega_r h^2 = 4.31 \times 10^{-5}$ where h is the reduced Hubble constant. In this chapter, we assume a flat universe and use the values obtained from Planck satellite [20]: $h = 0.692$, $\Omega_m = 0.308$ and $\Omega_\Lambda = 0.692$.

The power of the gravitational wave background is usually characterized by $\Omega_{\rm gw} \equiv (\mathrm{d}\rho_{\rm gw}/\mathrm{dln}f)/\rho_c$, where $\rho_{\rm gw}$ is the energy density of gravitational waves and ρ_c is the critical density of the universe. The gravitational wave spectrum generated from kinks on infinite strings is given by

$$\Omega_{\rm gw}(f) = \frac{2\pi^2 f^2}{3H_0^2} \int \frac{dz}{z} \Theta(n(f,z)-1) n(f,z) h^2(f,z)\,, \tag{7.2.24}$$

where

$$n(f,z) = \frac{1}{f}\frac{d\dot{N}}{d\ln z} = \frac{1}{f}\cdot\frac{1}{2}\theta_m(f,z)\frac{z}{1+z}\frac{\psi_{\rm max}(\omega,z)N(\psi_{\rm max}(\omega,z),z)}{V} l^{-1}\frac{dV}{dz}\,, \tag{7.2.25}$$

and $dV/dz = 4\pi a^3 r^2(z)/H(z)$ is the volume between the redshift z and $z + dz$. The step function $\Theta(n(f,z) - 1)$ is introduced to exclude rare bursts, whose intervals are longer than $\sim 1/f$ and cannot form a continuous background of gravitational waves. Note the difference in the notation: $\psi\tilde{N}$ (number of kinks with sharpness $\ln\psi \sim \ln\psi + d\ln\psi$ per volume) in ref. [55] is identical to $\psi N/V$ in this chapter. In summary, the differences with respect to ref. [55] are

- We replace the typical curvature of infinite string as $l \sim \gamma t$ instead of $l \sim t$.
- The probability of observing the gravitational wave burst from a kink is $\theta_m/2$ [107] instead of $\theta_m/4$.
- The distance r and the volume dV/dz are calculated numerically instead of using approximated analytic expressions.
- Ω_Λ is included in the calculation of the Hubble parameter.

These changes increase the overall spectral amplitude by 9.6 in RD era and 2.7 in MD era compared to the one calculated in ref. [55].

7.3 Results

7.3.1 Result with the tanh interpolation

We first solve the differential equation (7.2.15) using the tanh interpolation (7.2.18) with the values in table 7.1. The result is shown in figure 7.1. As mentioned in the

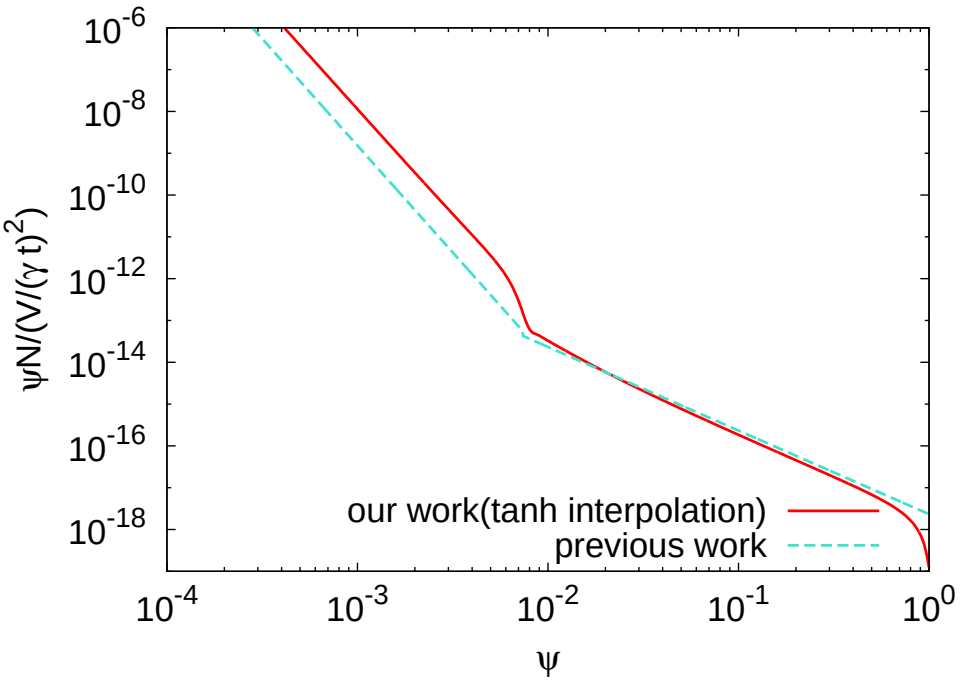

Figure.7.1 The distribution function of kinks obtained using the tanh interpolation. The vertical axis is the number of kinks on infinite strings per length. The horizontal axis is the sharpness of kinks. The light-blue broken line is the analytic estimation in the previous work [55] and the red solid line is our numerical result.

previous section, the sharpness of kinks decreases with time. The number of old kinks with small sharpness is larger than new ones, because $\mathcal{O}(1-10)$ of kinks are produced per horizon and the number of newly produced kinks per comoving length decreases as the horizon grows. In figure 7.1, we find that the distribution function of kinks has two regions with different slopes. The left part ($\psi \lesssim 10^{-2}$) corresponds to kinks generated during the RD era, and the right part ($\psi \gtrsim 10^{-2}$) corresponds to kinks generated in the MD era. Note that our result has a step at radiation-matter equality ($\psi \sim 7.4 \times 10^{-3}$), which is not seen in the result of the previous work. The reason will be discussed in the next section.

Figure 7.2 is the numerical results for the power spectrum of the gravitational wave background $\Omega_{\rm gw}$. To calculate the gravitational wave background, we first look for the value which satisfies (7.2.22) each time in the calculation of $N(\psi, t)$ for each gravitational wave frequency ω, and define it as $\psi_{\rm max}(\omega, t)$. Then, using the values of $\psi_{\rm max}$, we numerically integrate (7.2.24) to obtain the power spectrum. Note that the vertical axis of figure 7.1 is identical to the inverse of the left hand side of (7.2.22).

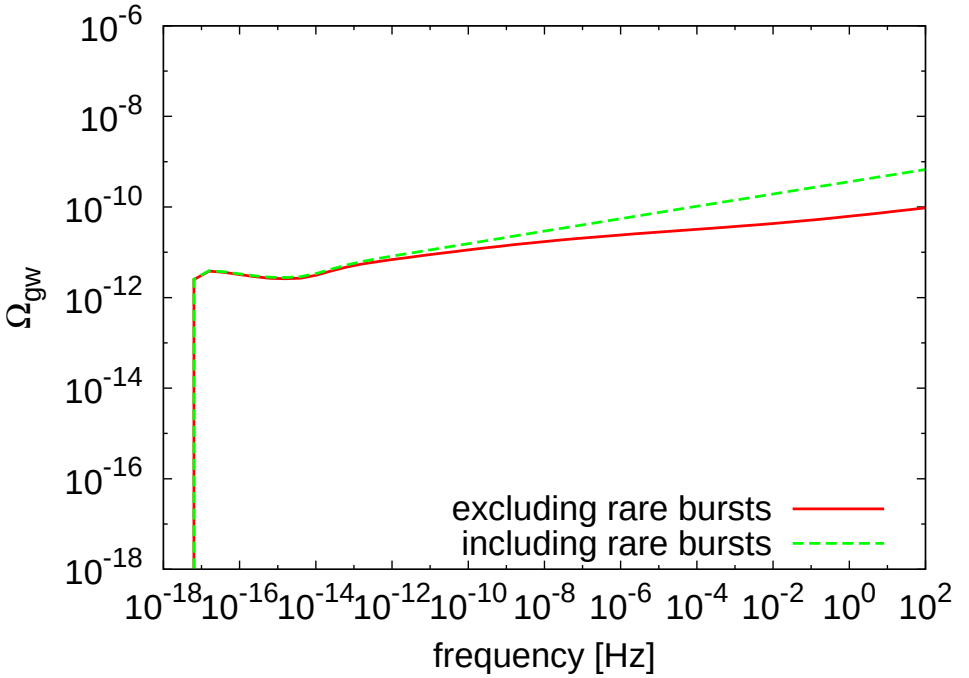

Figure.7.2 Power spectrum of the gravitational wave background for $G\mu = 10^{-7}$. The red solid line is the result obtained excluding rare bursts and the green broken line is the result including rare bursts.

So gravitational wave frequency ω is corresponded to the vertical axis of figure 7.1.

As seen in figure 7.1, old kinks are numerous and the gravitational wave emission has a short interval, while new kinks are few and the interval is large. Thus, the high frequency gravitational waves are emitted from old kinks and low frequency gravitational waves are from new kinks. The gravitational waves in the range of $10^{-13}\,\mathrm{Hz} \leq f$ are generated from kinks with small sharpness produced in the RD era. The middle frequency $10^{-15}\,\mathrm{Hz} \leq f \leq 10^{-13}\,\mathrm{Hz}$ corresponds to kinks produced during the transition from the RD era to the MD era. The low frequency gravitational waves $f \leq 10^{-15}\,\mathrm{Hz}$ are emitted from kinks produced in the MD era.

7.3.2 Result with the VOS model

In this section, we solve the differential equation (7.2.15) by simultaneously solving the VOS equations (7.2.10) and (7.2.11). The VOS model provides time evolution of γ and v, which can be converted to ζ, η and $\bar{\Delta}$ by (7.2.19), (7.2.20) and (7.2.21). The time evolution of the parameters is shown in figure 7.3. We find their evolution

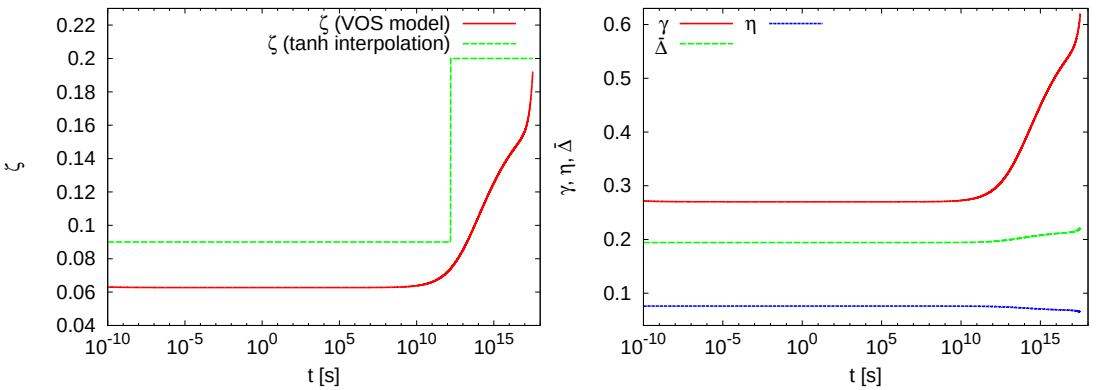

Figure.7.3 The time evolution of the parameters which characterize the production of kinks and their evolution. In the left figure, the time evolution of ζ is shown. The red solid line is obtained by solving VOS equations and the green broken line is the one interpolated by the tanh function. In the right figure, we show time evolution of $\gamma, \bar{\Delta}$ and η obtained by solving the VOS equations. The red solid line is γ, the green broken line is $\bar{\Delta}$ and the blue broken line is η.

is very different from the tanh interpolation. First, the VOS equations with $c = 0.23$ provide different asymptotic values of the parameters as seen by comparing tables 7.1 and 7.2. Second, the transition from the RD era to the MD era is not instant and it takes time to approach the asymptotic value. In addition, the parameter values change near the present time, since we include cosmological constant.

The distribution of kinks obtained by the VOS model is shown in figure 7.4. From the figure, we find two differences between the results with the tanh interpolation and the VOS model. First, the number of kinks increases considerably because the slope of the distribution function becomes steeper both for the RD and MD eras. Second, the position corresponding to radiation-matter equality has moved toward large ψ. The reason is discussed in the next section.

Figure 7.5 shows the power spectrum of the gravitational wave background $\Omega_{\rm gw}$ calculated using the kink distribution obtained by the VOS model. We see that the amplitude is larger than the case of the tanh interpolation, because of the increase in the number of kinks. Since the number increases more at small ψ, which corresponds kinks generated during the RD era, the power of the gravitational wave spectrum is enhanced in high frequencies.

Figure 7.6 is the comparison between sensitivity curves of future gravitational wave observations and the power spectra of the gravitational wave background for different values of string tension. The SKA [122] is a radio interferometer, which can detect

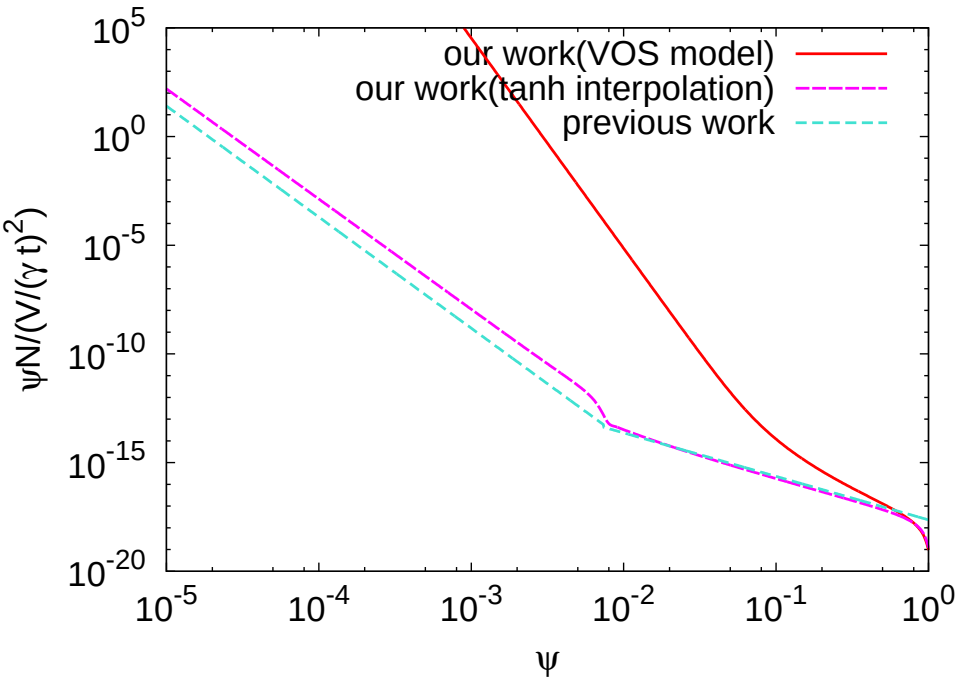

Figure.7.4 The distribution function of kinks obtained by solving the VOS equations (the red solid line). The axises is same as figure 7.1. For comparison, we also show the analytic estimation by the previous work [55] (light-blue broken line) and our result of the tanh interpolation (magenta broken line).

gravitational waves by pulsar timing arrays. The eLISA [123, 124] and DECIGO [125, 126] missions will observe gravitational waves using laser interferometers at space. Advanced-LIGO [127] is a laser interferometer constructed on the ground and will construct observation network with other ground-based detectors such as Advanced-VIRGO [128] and KAGRA in near future [129].

7.4 Discussion

First, let us compare our numerical result of the tanh interpolation with the previous work [55]. The major difference is that our result has a step-like feature in the distribution function of kinks at radiation-matter equality as seen in figure 7.1. This step arises because of the changes in the value of γ in the evolution equation of the distribution function. The source term in (7.2.15) (the first term in the right hand side) has a factor of $\bar{\Delta}/\gamma^4$, and it becomes smaller in the MD era. Thus, the number of newly produced kinks is smaller in the MD era.

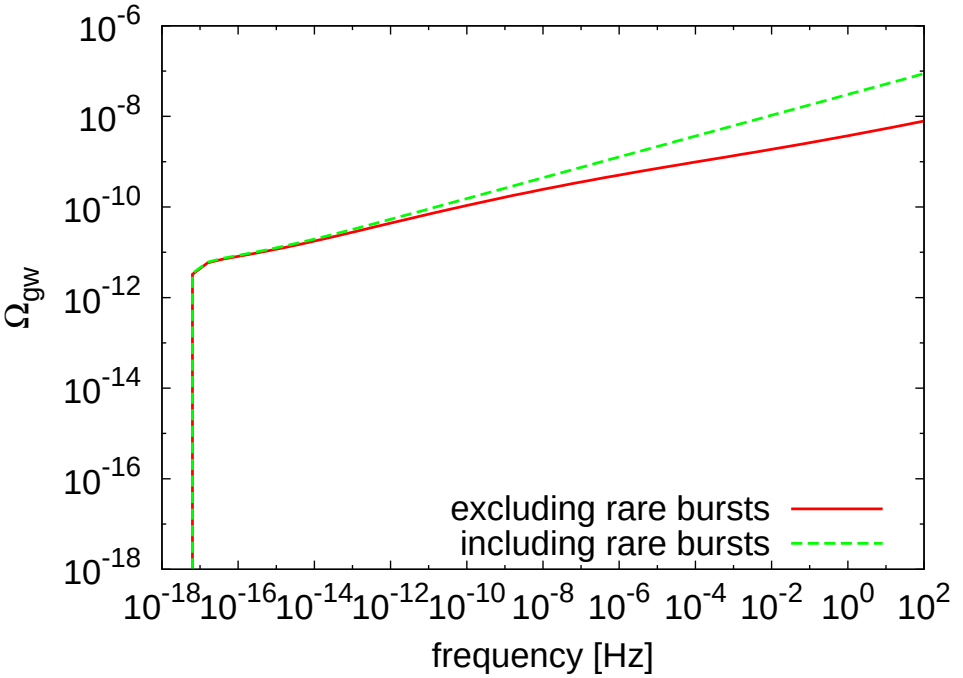

Figure.7.5 Power spectrum of the gravitational wave background for $G\mu = 10^{-7}$. The axises are same as figure 7.2.

The gravitational wave spectrum reflects the existence of this transition phase, and has three regions of different spectral slopes: the MD era $f \leq 10^{-15}\,\mathrm{Hz}$, the transition phase $10^{-15}\,\mathrm{Hz} \leq f \leq 10^{-13}\,\mathrm{Hz}$, and the RD era $10^{-13}\,\mathrm{Hz} \leq f$. Let us analytically estimate the frequency dependence of Ω_{gw}. The distribution function of kinks is related to the frequency of the gravitational wave background by (7.2.22). The low-frequency gravitational waves $f \leq 10^{-15}\,\mathrm{Hz}$ are generated by kinks produced in the MD era, and we can read $\psi N/(V/(\gamma t)^2) \sim \psi^{-2}$ from figure 7.1. Then we can derive $\Omega_{\mathrm{gw}} \propto f^{-1/6}$ using (7.2.22) and (7.2.23). This frequency dependence of the spectrum coincides with the analytic result in the previous work [55] and is also consistent with the numerical result shown in figure 7.2. The high-frequency region $10^{-13}\,\mathrm{Hz} \leq f$ corresponds to the gravitational wave from kinks produced in the RD era, where the result in figure 7.1 gives $\psi N/(V/(\gamma t)^2) \sim \psi^{-5.1}$ and we get $\Omega_{\mathrm{gw}} \propto f^{7/51}$. This also coincides with the analytic result of ref. [55], and is consistent with the spectrum with rare bursts in figure 7.2. The difference from the previous work arises in $10^{-15}\,\mathrm{Hz} \leq f \leq 10^{-13}\,\mathrm{Hz}$. In the transition phase, the value of ψ_{max} is the same for all the given frequency, so $\psi_{\mathrm{max}} \simeq$ Const., and we get $\Omega_{\mathrm{gw}} \propto f^{1/3}$ from (7.2.22) and (7.2.23). In fact, this frequency dependence can be seen in the numerical

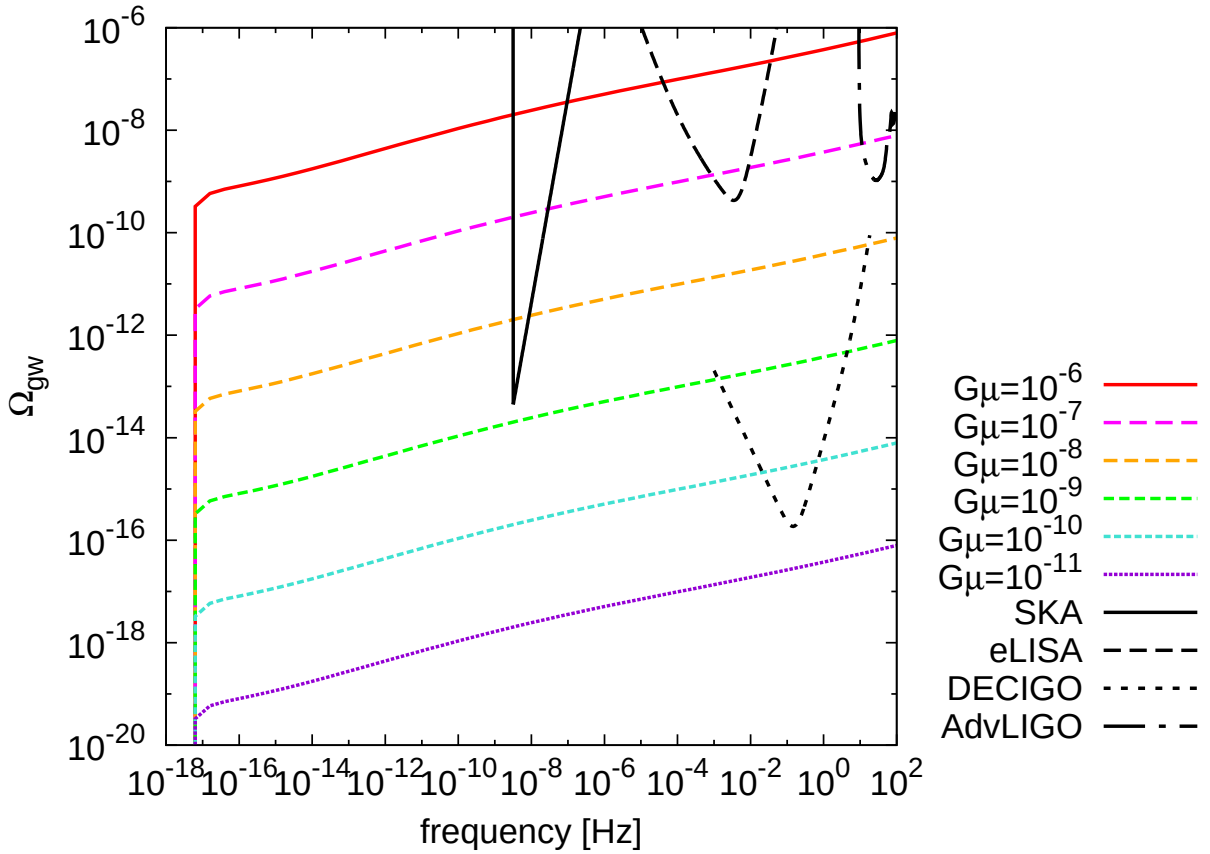

Figure.7.6 The power spectrum of the gravitational wave background for different string tensions. The spectrum shown here do not include rare bursts. The black solid and broken lines are sensitivity curves of gravitational wave experiments.

result of figure 7.2.

Let us compare the spectral amplitude with the previous work [55]. We compare the results using the case with rare bursts, since the condition of excluding rare bursts depends on the distribution function of kinks and the comparison cannot be made simply. First of all, the overall amplitude is 9.6 and 2.7 times larger than the previous work in RD and MD eras respectively, because of the modifications listed in section 7.2.4. In addition, the amplitude of the high frequency region increases because of the larger number of kinks produced during the RD era. By extracting the dependence on $\psi_{\max}$ and γ from (7.2.24), we obtain

$$\Omega_{\rm gw}(f) \propto f^2 \int \frac{{\rm d}z}{z} \psi_{\max}(\omega, z) \left(\psi_{\max}(\omega, z) \frac{N(\psi_{\max}(\omega, z), z)}{V/(\gamma t)^2} \right) \gamma^{-8/3}$$

$$\propto f^2 \int \frac{\mathrm{d}z}{z} \psi_{\max}(\omega, z) \gamma^{-8/3}. \tag{7.4.26}$$

As seen in figure 7.1, the number of kinks produced during RD era is larger than the previous work and the value of $\psi_{\max}$ becomes larger about twice for a fixed ω. Therefore, for every frequency of the gravitational wave background corresponding to the RD era, the amplitude $\propto \psi_{\max}$ becomes twice larger than in the previous work. In total, the spectral amplitude is a few times larger in the low frequency and $\mathcal{O}(10)$ larger in the high frequency.

Next, let us discuss the case where we solve the parameter evolution with the VOS model. First, we explain why the distribution of kinks has different shape compared to the case of the tanh interpolation. In ref. [55], the solution of the distribution function is provided as

$$\psi \frac{N}{V/(\gamma t)^2} \propto \psi^{\frac{-3+3\nu+\eta/\gamma}{2\zeta}}. \tag{7.4.27}$$

As seen in tables 7.1 and 7.2, the parameter values from the VOS equations are different from the ones used in the tanh case. They largely affect the ψ dependence of the distribution function as seen in (7.4.27). In particular, the small value of ζ increases the power of ψ, and makes the slope steeper. This increases the kink number considerably at small ψ. In addition, the number of kink production is determined by the coeficient of $\bar{\Delta}/\gamma^4$ in the first term of the right hand side of (7.2.15). The difference in this factor also increases the overall amplitude slightly. In figure 7.4, we also see the position of radiation-matter equality shifts to larger ψ. As provided in ref. [55], the value of ψ corresponding to radiation-matter equality ψ_* is given by

$$\psi_*(t_0) = \left(\frac{t_{\rm eq}}{t_0} \right)^{2\zeta_m}, \tag{7.4.28}$$

where the suffix m is the value during MD era. Since the value of ζ is smaller than the one used in the tanh case, ψ_* becomes larger in the VOS case.

Then, let us describe the reason of the large increase of the spectral amplitude in figure 7.5. The reason is the same as described in the tanh case, that is the increase of $\psi_{\max}$. For example, $\psi_{\max}$ increases 100 times at 10^2[Hz]. Then, from (7.4.26), $\Omega_{\rm gw}$ increases $\mathcal{O}(10^2)$. Taking account the enhancement of the overall amplitude 9.6 for RD era, we find that the power spectrum has increased $\mathcal{O}(10^3)$ at high frequencies compared to the previous work.

From figure 7.6, we find that the gravitational wave background from kinks on infinite strings is testable by future experiments depending on the tension of strings. The SKA would probe $G\mu \gtrsim 10^{-9}$, eLISA and Advanced-LIGO can test $G\mu \gtrsim 10^{-7}$,

and DECIGO has the strongest sensitivity to reach $G\mu \gtrsim 10^{-10}$. Note that the spectrum shown in figure 7.6 do not include rare bursts. Since rare bursts with large amplitude exists at high frequencies as seen in figure 7.2, laser-interferometer experiments could be also used to search for rare burst signals.

7.5 Conclusions

In this work, we have calculated the power spectrum of the gravitational wave background from kinks on infinite strings. First, we have solved the differential equation (7.2.15) to obtain the distribution function of kinks numerically in two ways. First, unlike the analytic estimation of ref. [55], we have smoothly connected the parameters using a tangent hyperboric function, which are related to the evolution of the cosmic string network, at radiation-matter equality. As a result, we have found a step in the distribution function of kinks at the transition from the RD era to the MD era, which was overlooked in the previous work [55]. At the same time, we have found an increase in the number of kinks generated in the RD era. Second, we have calculated the distribution of kinks by following the time evolution of the parameters with the VOS equations. We have found a steeper slope of the distribution function, which gives a large increase of the kink number at small sharpness, and the shift of the position of radiation-matter equality.

Next, using the numerical result of the distribution function of kinks, we have calculated the power spectrum of the gravitational wave background. In the case where we use the tanh interpolation, due to the step in the distribution function of kinks, we have found that the power spectrum behaves as $\Omega_{\rm gw} \propto f^{1/3}$ at $10^{-15}\,{\rm Hz} \lesssim f \lesssim 10^{-13}\,{\rm Hz}$. The power spectrum has increased more in the case where we solve the the VOS equations. In addition to the precise estimation of the kink distribution, we have also carefully evaluated all the factors involved in the calculation of the spectrum. This allows us to offer a rather precise prediction on the spectral amplitude. By comparing the results with sensitivities of future experiments, we have shown that gravitational waves from kinks on infinite strings can be probed at different frequencies.

Finally, let us comment on the gravitational wave background from cusps and kinks on cosmic string loops. Loops emit gravitational waves whose wavelength is shorter than the loop size, and usually the number of loops is more than that of infinite strings. Thus, it is more likely that the gravitational wave background generated

by infinite strings is sub-dominant at high frequencies compared to the one from loops. However, since the typical loop size is not known yet, gravitational waves from kinks on infinite strings could be more important than that from loops, especially for the SKA which probes low frequencies. It is important to consider both origins of gravitational wave background to provide constraints on cosmic strings, and thus our careful estimation of the gravitational wave background from kinks on infinite strings would help to constrain cosmic strings by observation at low frequencies. Moreover, there are cosmic superstrings predicted in superstring theory, and they also form the network consisting of loops and infinite strings. They have cusps and kinks which emit gravitational waves. Recently, the power spectrum of the gravitational wave background produced by loops of cosmic superstrings has been investigated [143], but the one from kinks on infinite superstrings is not clear yet. It is being examined in a work in progress. If a new era of multi-wavelength gravitational wave observations is successful and a detection was made, we might even be able to get insight in the physics of the very early universe.

Part.IV

Weak lensing signals from the texture

In this part, we will see the gravitational lensing signals from textures according to [4]. We focus on the weak lensing signals, which is called the CMB lensing and the cosmic shear, induced by the texture. In the standard cosmology, we have the scalar mode perturbations from the density and gravitational potential perturbations, and when we see the the lensing signals from the scalar mode perturbations, the signals from textures are contaminated by the contributions from the standard cosmological perturbations. On the other hand, the vector and tensor modes are the just decreasing modes when we consider the first order of the standard cosmological perturbation theory. Then we are not prevented by the quantities of the standard perturbation theory if we see the vector and tensor modes. Here we are interested in the signal induced by only vector and tensor modes, then we will see parity odd modes of the gravitational lensing signals.

Here we will introduce the cosmic defects and gravitational lensing theirselves, and their recent developments in section 8.1 at first. The next we define the un-equal time power spectra of the texture in vector and tensor modes in section 8.2. Then we will see the derivation of the parity odd modes, CMB lensing curl-mode and the cosmic shear B-mode, from the un-equal time power spectrum in section 8.3. Then we can see the resulting spectra and their observability in section 8.4.

Chapter.8

Weak lensing from self-ordering scalar fields

Cosmological defects result from cosmological phase transitions in the early Universe and the dynamics reflects their symmetry-breaking mechanisms. These cosmological defects may be probed through weak lensing effects because they interact with ordinary matters only through the gravitational force. In this chapter, we investigate global textures by using weak lensing curl and B modes. Non-topological textures are modeled by the non-linear sigma model (NLSM), and induce not only the scalar perturbation but also vector and tensor perturbations in the primordial plasma due to the nonlinearity in the anisotropic stress of scalar fields. We show angular power spectra of curl and B modes from both vector and tensor modes based on the NLSM. Furthermore, we give the analytic estimations for curl and B mode power spectra. The amplitude of weak lensing signals depends on a combined parameter $\epsilon_v^2 = N^{-1} (v/m_{\rm pl})^4$ where N and v are the number of the scalar fields and the vacuum expectation value, respectively. We discuss the detectability of the curl and B modes with several observation specifications. In the case of the CMB lensing observation without including the instrumental noise, we can reach $\epsilon_v \approx 2.7 \times 10^{-6}$. This constraint is about 10 times stronger than the current one determined from the Planck. For the cosmic shear observation, we find that the signal-to-noise ratio depends on the mean redshift and the observing number of galaxies as $\propto z_{\rm m}^{0.7}$ and $\propto N_{\rm g}^{0.2}$, respectively. In the study of textures using cosmic shear observations, the mean redshift would be one of the key design parameters.

8.1 introduction

Current cosmological observations confirm that the universe begins with extremely high temperature, what we call the hot big-bang model. As the universe expands adiabatically, it cools down from the hot initial condition. Therefore, it is natural to expect that cosmological phase transitions occur in the history of the universe. Cosmological phase transitions result in various cosmological defects depending on the symmetry of the phase transitions, e.g., cosmic strings, domain walls, and textures, which were first discussed by T.W.B.Kibble [8]. We can examine the nature of the phase transition that happened in the early universe through the resulting defects by using cosmological observations since these defects affect various observables; in the case of cosmic strings, see e.g., Ref. [144].

The global $O(N)$ symmetry breaking results in domain walls ($N = 1$), cosmic strings ($N = 2$), monopoles ($N = 3$), textures ($N = 4$), and non-topological textures ($N > 4$). Effects of the defects such as cosmic strings and textures can be seen at the horizon scale at that time, which corresponds to the correlation length of the strings or the textures. According to this fact, defects could affect several cosmological observables in the various scales through the metric perturbations, which include, for example, gravitational waves [42, 52, 53, 54, 55, 3], weak gravitational lensings [56, 57], generation of magnetic fields [1], the cosmic microwave background (CMB) angular power spectrum [32, 58] and the CMB lensing [145, 146, 147].

In this chapter, we focus on the non-topological texture with large-N limit $N \gg 4$ [148, 149, 150]. The dynamics of non-topological textures is exactly described by the non-linear sigma model (NLSM). Effects of textures on the cosmological observations, such as the large-scale structure [148, 151], cosmic microwave background fluctuations [152, 84, 153, 97, 98], gravitational waves [154, 45, 44], and generation of magnetic fields [2], have been studied in many articles. Some cosmological defects including textures induce not only the scalar, but also the vector and tensor modes originated from the anisotropic stress of scalar fields such as [42, 52, 53, 54, 55, 3, 56, 57, 1, 32, 58, 145, 146, 147, 152, 84, 153, 97, 98, 154, 45, 44, 2]. These vector and tensor modes are good tracers of cosmological defects since the vector and tensor modes do not arise from the standard cosmology in the linear order. It is possible to bring information of the phase transition that happened in the early stage of the universe through studying the vector and tensor modes induced from the cosmological defect.

We focus on the weak lensing from the vector and tensor modes induced by the non-topological texture. Photons emitted from the CMB last scattering surface and galaxies are deflected by the foreground scalar, vector, and tensor perturbations, called the CMB lensing and the cosmic shear, respectively [155, 156]. We can decompose these deflection patterns into the parity-even and parity-odd signatures. The parity-even signal emerged from the scalar, vector, and tensor modes. On the other hand, the parity-odd mode is induced only from the vector and tensor modes [157, 158, 159]. Therefore, the parity-odd mode of the CMB lensing and the cosmic shear, that is, the curl mode and the cosmic shear B-mode, respectively, are a good probe for the cosmological defects such as the texture. The parity-even modes of the CMB lensing and the cosmic shear which are induced from the first-order scalar mode have been detected with a high signal-to-noise ratio by e.g., the Planck [160], the Canada-France Hawaii Telescope Lensing Survey (CFHTLenS) [161, 162, 163], and the Dark Energy Survey (DES) [164, 165]. In previous studies, many parity-odd models have been studied and discussed, e.g., cosmic (super) strings [145, 146, 147], primordial gravitational waves [166, 167], or the second-order perturbation [168, 169, 170]. Although the parity-odd mode has not been detected, the prediction of the parity-odd mode for possible sources must become one of the important observable in the future high sensitivity observations.

In this chapter, we study the parity-odd signals from the non-topological texture governed by the NLSM with large-N limit. The outline of this chapter is as follows. In Section 8.2, we review and summarize the NLSM with large-N limit. The NLSM has N-component real scalar fields and the non-linearity of these scalar fields induces the vector and tensor modes. The vector and tensor modes from the NLSM with large-N limit can be determined by solving Einstein equation. In addition, we give an analytical estimation of the vector and tensor modes. In Section 8.3, we present the formulation of weak lensing signals. As mentioned above, we focus on the parity-odd signatures, that is, the curl mode for the CMB lensing and the B-mode for the cosmic shear. In Section 8.4, we provide results and discussions. We also give analytical estimates of the lensing signal and discussions of the detectability of the non-topological texture. In Section 8.5, we provide our conclusion.

8.2 Non-linear sigma model

In this section, we review the non-linear sigma model (NLSM), which has the vector and tensor modes originated from the anisotropic stress of scalar fields. The NLSM can accurately describe cosmological defects with the global $O(N)$ symmetry in the case of $N > 2$ [148, 149]. Throughout this chapter, we assume the background metric is given by the Friedman-Robertson-Walker metric as

$$ds^2 = a(\eta)^2 \left[-d\eta^2 + d\boldsymbol{x}^2\right] \ , \tag{8.2.1}$$

where η and $a(\eta)$ are the conformal time and the scale factor, respectively.

We focus on the dynamics of real N-scalar fields with the Lagrangian which satisfies the global $O(N)$ symmetry:

$$\mathcal{L} = -\frac{1}{2}\left(\nabla_\mu \boldsymbol{\Phi}^t\right)\left(\nabla^\mu \boldsymbol{\Phi}\right) - \frac{\lambda}{4}\left(\boldsymbol{\Phi}^t\boldsymbol{\Phi} - v^2\right)^2 + \mathcal{L}_{\rm T} \ , \tag{8.2.2}$$

where we define the array of real N-scalar fields as $\boldsymbol{\Phi} = (\phi_1, \phi_2, \cdots, \phi_N)$. Moreover, v and λ are the vacuum expectation value (VEV) and the dimensionless self-coupling parameter, respectively. The interaction with the thermal environment having the temperature T is represented as $\mathcal{L}_{\rm T} \sim T^2\boldsymbol{\Phi}^t\boldsymbol{\Phi}$. In the case of low temperature, $T \ll v$, the global $O(N)$ symmetry breaks spontaneously to $O(N-1)$ symmetry with the condition $\boldsymbol{\Phi}^t\boldsymbol{\Phi} = v^2$. According to this constraint, the equation of motion for scalar fields is determined from Eq. (8.2.2) as

$$\nabla^\mu\nabla_\mu\beta_a + \sum_{b=1}^{N-1}\left(\nabla^\mu\beta_b\right)\left(\nabla_\mu\beta^b\right)\beta_a = 0 \ , \tag{8.2.3}$$

where β_a is scalar fields normalized by the VEV, namely, $\beta_a \equiv \Phi_a/v$. The normalized scalar fields obey the condition $\sum_{a=1}^{N}\beta_a\beta^a = 1$. The above equation (8.2.3) is called the non-linear sigma model.

By taking the large-N limit in Eq. (8.2.3), the solution of Eq. (8.2.3) in the Fourier space is given as [2]

$$\beta_a(\boldsymbol{k},\eta) = \sqrt{A_\nu}\left(\frac{\eta}{\eta_{\rm ini}}\right)^{3/2}\frac{J_\nu(k\eta)}{(k\eta)^\nu}\beta_a(\boldsymbol{k},\eta_{\rm ini}) \ , \tag{8.2.4}$$

where $\nu \equiv d\ln a/d\ln\eta + 1$ and $A_\nu \equiv 4\Gamma(2\nu-1/2)\Gamma(\nu-1/2)/\left(3\Gamma(\nu-1)\right)$. We assume that $\beta_a(\boldsymbol{k},\eta_{\rm ini})$ are random gaussian variables. During the radiation- and matter-dominated eras, the parameter ν takes $\nu_{\rm rad} = 2$ and $\nu_{\rm mat} = 3$, respectively. Although

the solution of scalar fields β_a depends on the phase transition time $\eta_{\rm ini}$, the power spectrum of scalar fields is independent of this time [2]. The dimensionless power spectrum for normalized scalar fields can be given as

$$\langle \beta_a(\boldsymbol{k},\eta)\beta_b^*(\boldsymbol{k'},\eta)\rangle = \frac{2\pi^2}{k^3}\mathcal{P}_\beta(k,\eta)\delta_{ab}(2\pi)^3\delta_d^3(\boldsymbol{k}-\boldsymbol{k'}) \ , \tag{8.2.5}$$

$$\mathcal{P}_\beta(k,\eta) = \frac{3A_\nu}{N}(k\eta)^3\left(\frac{J_\nu(k\eta)}{(k\eta)^\nu}\right)^2 \ , \tag{8.2.6}$$

where the initial power spectrum is determined as (see e.g., Ref. [45])

$$\langle \beta_a(\boldsymbol{k},\eta_{\rm ini})\beta_b^*(\boldsymbol{k'},\eta_{\rm ini})\rangle = \begin{cases} \frac{6\pi^2\eta_{\rm ini}^3}{N}\delta_{ab}(2\pi)^3\delta_d^3(\boldsymbol{k}-\boldsymbol{k'}) & (k\eta_{\rm ini}\ll 1) \\ 0 & (k\eta_{\rm ini}\gtrsim 1) \ . \end{cases} \tag{8.2.7}$$

The amplitude of the solution is determined to satisfy the condition $\sum_{a=1}^N \beta_a\beta^a = 1$. Note that, the configuration of scalar fields is not correlated on sub-horizon scales, i.e., $k\eta_{\rm ini} \gtrsim 1$. In other words, as expressed in the above equation, the correlation of scalar fields vanishes in these scales. From Eq. (8.2.6), we can see that the power spectrum of scalar fields does not depend on the initial time. Therefore, we have omitted the initial time $\eta_{\rm ini}$ from the argument of the power spectrum. The energy momentum tensor for scalar fields is written as

$$T^\phi_{\mu\nu} = v^2\sum_a\left[(\partial_\mu\beta_a)(\partial_\nu\beta^a) - \frac{1}{2}g_{\mu\nu}(\partial_\lambda\beta_a)\left(\partial^\lambda\beta^a\right)\right] \ . \tag{8.2.8}$$

The anisotropic stress of scalar fields corresponds to the (i,j) component of the energy momentum tensor.

From here, we derive evolution equations for the vector and tensor metric perturbations with the anisotropic stress of self-ordering scalar fields. In our study, we work in the Poisson gauge given by

$$ds^2 = a^2(\eta)\left[-d\eta^2 + 2\sigma_i d\eta dx^i + (\delta_{ij}+h_{ij})\,dx^i dx^j\right] \ , \tag{8.2.9}$$

where we drop the scalar metric perturbation since we are interested in the vector σ_i and tensor h_{ij} perturbations. Due to the gauge conditions, the vector and tensor perturbations satisfy ${\sigma^i}_{,i} = {h^{ij}}_{,i} = 0$.

The Einstein equations for the vector $\sigma_{\rm V}$ and tensor $h_{\rm T}$ perturbations in the Fourier space are given as

$$k\left[\dot\sigma_{\rm V}(\boldsymbol{k},\eta) + 2\mathcal{H}\sigma_{\rm V}(\boldsymbol{k},\eta)\right] = \frac{8\pi}{m_{\rm pl}^2}\pi^\phi_{\rm V}(\boldsymbol{k},\eta) \ , \tag{8.2.10}$$

$$\ddot h_{\rm T}(\boldsymbol{k},\eta) + 2\mathcal{H}\dot h_{\rm T}(\boldsymbol{k},\eta) + k^2 h_{\rm T}(\boldsymbol{k},\eta) = \frac{8\pi}{m_{\rm pl}^2}\pi^\phi_{\rm T}(\boldsymbol{k},\eta) \ , \tag{8.2.11}$$

where a dot denotes the derivative with respect to the conformal time. Anisotropic stresses for the vector and tensor modes can be given by the product of scalar fields as

$$\pi_{\rm V}^{\phi}(\boldsymbol{k},\eta) = \int \frac{d^3\boldsymbol{q}}{(2\pi)^3}\int \frac{d^3\boldsymbol{p}}{(2\pi)^3}\delta_d^3(\boldsymbol{k}-\boldsymbol{q}-\boldsymbol{p})\left[\frac{v^2}{2}\sqrt{1-\mu^2}q(k-2q\mu)\right]\sum_a \beta_a(\boldsymbol{q},\eta)\beta^a(\boldsymbol{p},\eta)\,, \tag{8.2.12}$$

$$\pi_{\rm T}^{\phi}(\boldsymbol{k},\eta) = \int \frac{d^3\boldsymbol{q}}{(2\pi)^3}\int \frac{d^3\boldsymbol{p}}{(2\pi)^3}\delta_d^3(\boldsymbol{k}-\boldsymbol{q}-\boldsymbol{p})\left[v^2\left(1-\mu^2\right)q^2\right]\sum_a \beta_a(\boldsymbol{q},\eta)\beta^a(\boldsymbol{p},\eta)\,, \tag{8.2.13}$$

where we define $\mu \equiv \hat{\boldsymbol{k}}\cdot\hat{\boldsymbol{q}}$. In order to predict the weak lensing signal, we define the dimensionless unequal-time power spectra for the vector and tensor modes which are defined as

$$\langle \xi_{\rm X}(\boldsymbol{k},\eta)\xi_{\rm X}^*(\boldsymbol{k'},\eta')\rangle = (2\pi)^3\delta_d^3(\boldsymbol{k}-\boldsymbol{k'})\frac{2\pi^2}{k^3}\mathcal{P}_{\rm X}(k,\eta,\eta')\,, \tag{8.2.14}$$

where $\xi_{\rm X}$ denotes the vector ($\xi_{\rm X}=\sigma_{\rm V}$) and tensor ($\xi_{\rm X}=h_{\rm T}$) modes. We can solve evolution equations for the vector and tensor modes in Eqs. (8.2.12) and (8.2.13) straightforwardly. By using solutions of the vector and tensor modes, we can write down the dimensionless unequal-time power spectrum during the matter-dominated era ($\nu=3$) as

$$\mathcal{P}_{\rm X}(k\eta,k\eta') = \mathcal{A}\int_{-\infty}^{\infty} d\ln q_k \int_{-1}^{1} d\mu \mathcal{F}_{\rm X}(q_k,\mu,k\eta)\mathcal{F}_{\rm X}(q_k,\mu,k\eta')\,, \tag{8.2.15}$$

$$\begin{aligned}\mathcal{A} &= 144\pi^2 A_3^2\epsilon_v^2\,,\\ &\approx 1.22\times 10^7\epsilon_v^2\,,\end{aligned} \tag{8.2.16}$$

$$\mathcal{F}_{\rm V}(q_k,\mu,x) = \sqrt{1-\mu^2}\,(1-2q_k\mu)\,q_k^{5/2}\frac{1}{x^4}\int_0^x dx_1\; x_1^7\frac{J_3(q_kx_1)}{(q_kx_1)^3}\frac{J_3(p_kx_1)}{(p_kx_1)^3}\,, \tag{8.2.17}$$

$$\mathcal{F}_{\rm T}(q_k,\mu,x) = 2(1-\mu^2)q_k^{7/2}\frac{1}{x^3}\int_0^x dx_1\;\left[xx_1G(x,x_1)\right]x_1^4\frac{J_3(q_kx_1)}{(q_kx_1)^3}\frac{J_3(p_kx_1)}{(p_kx_1)^3}\,, \tag{8.2.18}$$

where $q_k \equiv q/k$, $p_k \equiv p/k$, $x \equiv k\eta$, and $G(x,x_1) = xx_1\left(j_1(x_1)n_1(x) - j_1(x)n_1(x_1)\right)$ is the Green function for the evolution equation of the tensor mode (8.2.11), and $J_\nu(x)$, $j_\nu(x)$, and $n_\nu(x)$ are the Bessel function, the spherical Bessel function, and the spherical Neumann function, respectively. The shape of the unequal-time power spectrum does not depend on the theoretical parameters such as N and v. These parameters change only the amplitude of the power spectrum and appear through a special combination of $N^{-1}v^4$. Therefore, in this chapter, we define a new parameter through the combination of theoretical parameters as

$$\epsilon_v^2 \equiv N^{-1}\left(v/m_{\rm pl}\right)^4\,. \tag{8.2.19}$$

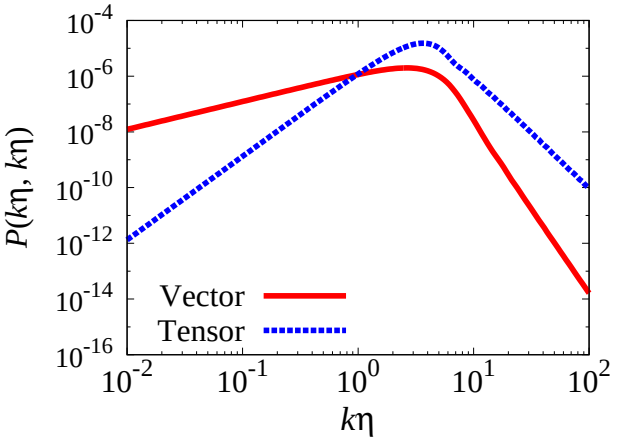

Figure.8.1 Power spectra $\mathcal{P}(k\eta, k\eta)$ for the vector and tensor modes from the NLSM. For the presentation purpose, we set $\mathcal{A} = 1$ in this figure. Due to the convolution of scalar fields in Eqs. (8.2.12) and (8.2.13), the peak moves to smaller scales than the horizon scale where $k\eta = 1$.

In this chapter, for simplicity, we evaluate the weak lensing signal by using the power spectrum during the matter-dominated era. The correction to the radiation component should be small since lensing signals are mainly contributed from the perturbations at late times of cosmic evolution.

We depict the dimensionless equal-time power spectrum for the vector and tensor modes in Fig. 8.1. We can see that on super (sub) horizon scales, the vector (tensor) mode is greater than the tensor (vector) mode. In the following section, in order to discuss the angular power spectra of the curl and B modes, we evaluate the asymptotic power on small scales. From here, we estimate the asymptotic power of the dimensionless equal-time power spectrum on sub-horizon scales as follows. At first, let us see the vector mode. By integrating Eq. (8.2.17), we obtain the notation of $\mathcal{F}_{\rm V}(q_k, \mu, x)$ exactly as

$$\mathcal{F}_{\rm V}(q_k, \mu, x) = \sqrt{1-\mu^2} q_k^{-1/2} p_k^{-3} x^{-3} \left(q_k J_2(q_k x) J_3(p_k x) - p_k J_3(q_k x) J_2(p_k x) \right) \ . \tag{8.2.20}$$

Using the approximations for the Bessel function, $J_\nu(x \ll \nu) \propto x^\nu$ and $J_\nu(x \gg \nu) \propto x^{-1/2}{\rm cos}x$, and assuming a cutoff scale $1/x$, we can integrate the auto-power spectrum for the vector mode as

$$\mathcal{P}_{\rm V}(x, x) \propto x^{-6} \int^{1/x} dq_k \Big[p_k^{-6} J_3^2(p_k x) J_2^2(q_k x) \\ -2 p_k^{-5} q_k^{-1} J_2(p_k x) J_3(p_k x) J_2(q_k x) J_3(q_k x) + p_k^{-4} q_k^{-2} J_2^2(p_k x) J_3^2(q_k x) \Big]$$

$$\sim \alpha_1 x^{-8} + \alpha_2 x^{-7} + \alpha_3 x^{-6}$$
$$\propto x^{-6} \,, \tag{8.2.21}$$

where α_1, α_2 and α_3 are constants. Therefore the $k\eta$ dependence of $\mathcal{P}_{\rm V}(k\eta, k\eta)$ is $\propto (k\eta)^{-6}$. Next, we see the tensor mode. Here we find the most dominant term of $\mathcal{F}_{\rm T}(q_k, \mu, x)$, that is, the highest power of x and x_1, by considering the integrand as

$$\begin{aligned}
\mathcal{F}_{\rm T}(q_k, \mu, x) &\sim p_k^{-3} q_k^{-1/2} x^{-3} \int^x dx_1 \left[(x_1 - x)\cos(x - x_1) + (1 + x x_1)\sin(x - x_1)\right] \\
&\quad \times x_1^{-2} J_3(q_k x_1) J_3(p_k x_1) \\
&\sim p_k^{-3} q_k^{-1/2} x^{-2} \int^{x \to 1/q_k} dx_1 x_1^{-1} \sin(x - x_1) J_3(q_k x_1) J_3(p_k x_1) \\
&\sim p_k^{-3} q_k^{-1/2} x^{-2} q_k J_3(p_k/q_k),
\end{aligned} \tag{8.2.22}$$

where we have assumed $p_k > q_k$ and we can obtain the expression for the case $p_k < q_k$ in the same way. Now we are able to calculate the $k\eta$ dependence of $\mathcal{P}_{\rm T}(x, x)$ as

$$\begin{aligned}
\mathcal{P}_{\rm T}(x, x) &\propto \int dq_k q_k^{-1} \left[p_k^{-3} q_k^{-1/2} x^{-2} q_k J_3(p_k/q_k)\right]^2 \\
&\propto x^{-4} \propto (k\eta)^{-4} \,.
\end{aligned} \tag{8.2.23}$$

Here we have obtained the $k\eta$ dependence of the dimensionless equal-time power spectrum for vector and tensor modes as $\mathcal{P}_{\rm V}(k\eta, k\eta) \propto (k\eta)^{-6}$ and $\mathcal{P}_{\rm T}(k\eta, k\eta) \propto (k\eta)^{-4}$, respectively. These spectra leave various trails on physical values and these estimations enable us to predict their analytic forms.

8.3 Weak lensing

In this section, we give a review about the relation between weak lensing signals and vector and tensor perturbations from the textures following Refs. [145, 159]. We pull parity-odd signals from the CMB lensing and the cosmic shear which are called the curl and B modes, respectively. In the following subsection, we present details about the curl and B modes.

8.3.1 CMB lensing curl mode

CMB photons are deflected by foreground scalar, vector, and tensor perturbations. We decompose the deflection angle of CMB photons projected on the celestial sphere

$\Delta_a(\hat{\boldsymbol{n}})$ into the gradient ($\phi(\hat{\boldsymbol{n}})$) and curl ($\varpi(\hat{\boldsymbol{n}})$) modes as

$$\Delta_a(\hat{\boldsymbol{n}}) = \nabla_a \phi(\hat{\boldsymbol{n}}) + (\nabla_b \varpi(\hat{\boldsymbol{n}}))\, \epsilon^b{}_a \ , \tag{8.3.24}$$

where $\epsilon^b{}_a$ is the covariant dimensional Levi-Civita tensor. Note that latin characters started from a, b, $\cdots$ in the above relation denote the azimuthal and polar angles denoted as θ and ϕ, respectively. From here, we drop the gradient mode since, in this chapter, we are interested in the curl mode.

In order to relate the curl mode and the angular power spectrum, we solve the geodesic equation in the perturbed spacetime. By solving the perturbed geodesic equation, the curl mode can be expressed by using the metric perturbations of the vector and tensor modes as

$$\varpi^{:a}{}_{:a} = -\int_0^{\chi_{\rm S}} d\chi \frac{\chi_{\rm S} - \chi}{\chi \chi_{\rm S}} \left[\frac{d}{d\chi} \left(\chi \Omega^a{}_{:b} \epsilon^b{}_a \right) \right] \ , \tag{8.3.25}$$

where χ is the comoving distance measured from the observer at the origin and $\chi_{\rm S}$ is the comoving distance at the sources. Ω^a in Eq. (8.3.25) includes the vector and tensor perturbations as

$$\Omega_a = \left(-\sigma_i + h_{ij} e^j_\chi \right) e^i_a \ , \tag{8.3.26}$$

where e^i_χ and e^i_a are the orthogonal spacelike basis along the light ray. We expand the curl mode by using the spherical harmonics and define the angular power spectrum for the curl mode as

$$\varpi(\hat{\boldsymbol{n}}) = \sum_{\ell,m} \varpi_{\ell,m} Y_{\ell,m}(\hat{\boldsymbol{n}}) \ , \tag{8.3.27}$$

$$C_\ell^{\varpi\varpi} = \frac{1}{2\ell+1} \sum_{m=-\ell}^{\ell} \left\langle \varpi_{\ell,m} \varpi^*_{\ell,m} \right\rangle \ . \tag{8.3.28}$$

Finally, we obtain the angular power spectrum of the curl mode in terms of the vector (X = V) and tensor (X = T) perturbations as

$$C_\ell^{({\rm X})\varpi\varpi} = 4\pi \int_0^\infty \frac{dk}{k} \int_0^{\chi_S} k d\chi \int_0^{\chi_S} k d\chi' \mathcal{S}^{({\rm X})}_{\varpi,\ell}(k\chi) \mathcal{S}^{({\rm X})}_{\varpi,\ell}(k\chi') \mathcal{P}_{\rm X}(k, \eta_0 - \chi, \eta_0 - \chi') \ , \tag{8.3.29}$$

where $\mathcal{P}_{\rm X}(k, \eta, \eta')$ denotes the dimensionless unequal-time power spectrum of metric perturbations. $\mathcal{S}^{({\rm X})}_{\varpi,\ell}(k\chi)$ is the weight function defined as

$$\mathcal{S}^{({\rm V})}_{\varpi,\ell}(x) = \sqrt{\frac{(\ell-1)!}{(\ell+1)!}} \frac{j_\ell(x)}{x} \ , \tag{8.3.30}$$

$$\mathcal{S}^{({\rm T})}_{\varpi,\ell}(x) = \frac{1}{2} \frac{(\ell-1)!}{(\ell+1)!} \sqrt{\frac{(\ell+2)!}{(\ell-2)!}} \frac{j_\ell(x)}{x^2} \ . \tag{8.3.31}$$

In the case of the CMB lensing, the comoving distance to the source $\chi_{\rm S}$ corresponds to that to the CMB last scattering surface.

We assume that the curl-mode lensing potential is reconstructed by using the quadratic estimator [171, 172]. In this case, the CMB lensing noise arises from the lensing reconstruction noise from the cosmic variance of the lensed CMB fluctuations. We assume an ideal experiment for the CMB lensing throughout this chapter and neglect instrumental noise. Consequently, the noise of the CMB lensing is limited by the reconstruction noise due to the quadratic estimator.

8.3.2 Cosmic shear B-mode

The intrinsic shape of galaxies is deformed by foreground perturbations. The deformation pattern is characterized by the reduced shear [173, 156]. The geodesic deviation equation describes the deformation of the shape of galaxies. By solving the geodesic deviation equation, we can relate the reduced shear and the vector and tensor perturbations as [145, 159]

$$g = -\frac{1}{2}\int_0^{\chi_{\rm S}} d\chi \frac{\chi_{\rm S}-\chi}{\chi\chi_{\rm S}}\left[\nabla_a\nabla_b\Upsilon - \frac{d}{d\chi}\left(\chi\nabla_b\Omega_a\right)\right]e_+^a e_+^b - \frac{1}{4}\left[h_{ab}e_+^a e_+^b\right]_0^{\chi_{\rm S}} \ , \quad (8.3.32)$$

where Υ contains the scalar, vector, and tensor modes as

$$\Upsilon = -\left(\Psi+\Phi\right) - \sigma_i e_\chi^i + \frac{1}{2}h_{ij}e_\chi^i e_\chi^j \ . \quad (8.3.33)$$

Note that Υ does not appear in the cosmic shear B-mode but in the cosmic shear E-mode. Therefore, we do not focus on Υ when we study the cosmic shear B-mode. Because the reduced shear is a spin-2 variable, we can expand the reduced shear according to the spin-2 spherical harmonics as

$$g(\hat{\boldsymbol{n}}) = \sum_{\ell,m}\left(E_{\ell m} + iB_{\ell m}\right){}_{+2}Y_{\ell m}(\hat{\boldsymbol{n}}) \ , \quad (8.3.34)$$

where we split multipole coefficients into E and B modes by using the parity. Hereafter, we focus on the cosmic shear B-mode and drop the E-mode. As well as the CMB lensing, the angular power spectrum of the B mode is defined as

$$C_\ell^{BB} = \frac{1}{2\ell+1}\sum_{m=-\ell}^{\ell}\langle B_{\ell m}B_{\ell m}^*\rangle \ . \quad (8.3.35)$$

	$f_{\rm sky}$	$z_{\rm m}$	$N_{\rm g}[{\rm arcmin}^{-2}]$
HSC	0.05	1.0	35
SKA	0.75	1.6	10
LSST	0.5	1.5	100

Table.8.1 The experimental specifications of the HSC, SKA, and LSST.

By solving the perturbed geodesic deviation equation, we can relate the angular power spectrum of the B mode and the vector or tensor metric perturbations as

$$C_\ell^{({\rm X})BB} = \left[\frac{1}{4}\frac{(\ell+2)!}{(\ell-2)!}\right] 4\pi \int_0^\infty \frac{dk}{k} \int_0^\infty k d\chi \int_0^\infty k d\chi' \times \mathcal{S}_{B,\ell}^{({\rm X})}(k,\chi)\mathcal{S}_{B,\ell}^{({\rm X})}(k,\chi')\mathcal{P}_{\rm X}(k,\eta_0-\chi,\eta_0-\chi') \ , \tag{8.3.36}$$

where weight functions are defined as

$$\mathcal{S}_{B,\ell}^{({\rm V})}(k,\chi) = \sqrt{\frac{(\ell-1)!}{(\ell+1)!}} \int_\chi^\infty d\chi_S \frac{N(\chi_S)}{N_{\rm g}} \frac{j_\ell(k\chi)}{k\chi} \ , \tag{8.3.37}$$

$$\mathcal{S}_{B,\ell}^{({\rm T})}(k,\chi) = \frac{1}{2}\frac{(\ell-1)!}{(\ell+1)!}\sqrt{\frac{(\ell+2)!}{(\ell-2)!}} \left[\int_\chi^\infty d\chi_S \frac{N(\chi_S)}{N_{\rm g}} \frac{j_\ell(k\chi)}{(k\chi)^2}\right] + \frac{1}{2}\sqrt{\frac{(\ell-2)!}{(\ell+2)!}} \frac{N(\chi)}{N_{\rm g}} \left(j_\ell'(k\chi) + 2\frac{j_\ell(k\chi)}{k\chi}\right) \ . \tag{8.3.38}$$

To investigate the cosmic shear signals, we need the distribution of galaxies $N(\chi)$, which should be determined by observations. Here we assume the following form:

$$N(\chi)d\chi = N_{\rm g}\frac{3}{2}\frac{z^2}{(0.64z_{\rm m})^3} \exp\left[-\left(\frac{z}{0.64z_{\rm m}}\right)^{3/2}\right] dz \ , \tag{8.3.39}$$

where $z_{\rm m}$ is the mean redshift, and $N_{\rm g}$ is the number of galaxies per square arcminute. In our study, we assume three ongoing and forthcoming survey designs, that is, the Subaru Hyper-Suprime Cam (HSC) [174], the Square Kilometer Array (SKA) [175], the Large Synoptic Survey Telescope (LSST) [176]. Individual experimental specifications are summarized in Table. 8.1. We assume that the noise of the cosmic shear is the shot noise originated from the intrinsic shape of galaxies written as

$$N_\ell^{BB} = \frac{\left\langle \gamma_{\rm int}^2 \right\rangle}{3600 N_{\rm g} \left(180/\pi\right)^2} \ , \tag{8.3.40}$$

where $\left\langle \gamma_{\rm int}^2 \right\rangle^{1/2}$ is the root-mean square ellipticity of galaxies, which is determined about 0.3 in Ref. [177].

Note that without the dependence of the distribution of galaxies, i.e., $N(\chi) =$ const., there is the relation between the CMB lensing curl-mode and the cosmic shear B-mode power spectra as [159]

$$C_\ell^{\varpi\varpi} = 4\frac{(\ell-2)!}{(\ell+2)!}C_\ell^{BB} \ . \tag{8.3.41}$$

We use this relation in the following section to obtain the asymptotic scaling of the angular power spectra.

Before closing this section, we mention our treatment about the unequal-time power spectrum. To calculate weak lensing signals, we need to use the unequal-time power spectrum for the vector and tensor modes. For simplicity, to perform the multiple integration, we assume the case of the totally coherent model [178, 179, 93, 145] throughout this chapter. In other words, we can write the unequal-time power spectrum as $\mathcal{P}_{\rm X}(k\eta, k\eta') = \sqrt{\mathcal{P}_{\rm X}(k\eta, k\eta)\mathcal{P}_{\rm X}(k\eta', k\eta')}$. This assumption makes the computation of the angular power spectrum easy. From Eqs. (8.3.29) and (8.3.36), the unequal-time power spectrum is multiplied by the weight functions, which correspond to the spherical Bessel functions. The dominant contributions of the integrands on the angular power spectrum would be $\ell \sim k\eta$ since the spherical Bessel function $j_\ell(x)$ rapidly decays at $x > \ell$. We will show that it is sufficient to assume the totally coherent model on small scales by using the small-angle approximation, i.e., the Limber approximation. Therefore, the totally coherent model is a good approximation on small scales but not on large scales. We will discuss the detail of the effect of the totally coherent model in the next section.

8.4 Results and discussions

In this section, we present our main results and give discussions. In Fig. 8.2, we show weak lensing signals from the global texture modeled by the NLSM. We can find that the contribution to the lensing signal is dominated by the tensor mode. This is because the spherical Bessel function in Eqs. (8.3.29) and (8.3.36) projects on the angular power spectrum around $\ell \sim k\eta$ which corresponds to sub-horizon scales. In Fig. 8.1, the tensor mode has larger amplitude than the vector mode on sub-horizon scales. Therefore, the angular power spectra of the curl and B modes are dominated by the tensor mode. Moreover, the difference between the vector and tensor contributions on the lensing signal is greater at low redshift observation. Note that the CMB B-mode polarization from the tensor mode of the texture has almost

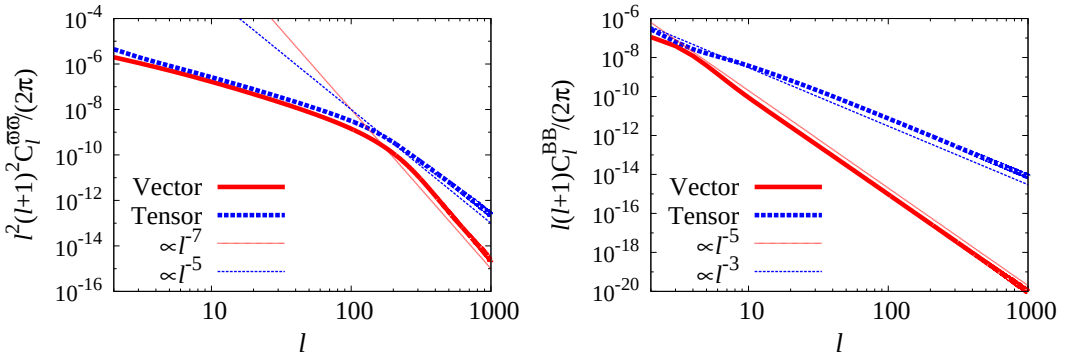

Figure.8.2 Left: The angular power spectrum of the CMB lensing curl-mode from vector and tensor modes of the texture. Right: The angular power spectrum of the cosmic shear B-mode from vector and tensor modes of the texture by assuming the observation as LSST. For the same reason in Fig. 8.1, we set the theoretical parameter set $\mathcal{A} = 1$ in both figures.

the same amplitude [97].

The CMB lensing curl-mode from the texture has a broken power at $\ell \approx 200$ which is smaller scale compared with the standard peak of the scalar lensing potential or the lensing from the primordial gravitational waves [159, 169]. This is because the peak of the power spectrum from the NLSM does not correspond to the horizon scale but slightly smaller scale due to the nonlinearity (see Fig. 8.1 or Ref. [98]). On large scales ($\ell \lesssim 200$), the power of the angular power spectra from the vector and tensor modes is proportional to ℓ^{-2}.

Moreover, we can obtain the analytic power on small scales ($\ell \gg 1$) by using the small-angle approximation as follows,

$$
\begin{aligned}
C_\ell^{(\mathrm{X})\varpi\varpi} &\propto \int_0^\infty \frac{dk}{k} \int_0^{\chi_S} k d\chi \int_0^{\chi_S} k d\chi' \mathcal{S}^{(X)}_{\varpi,\ell}(k\chi)\mathcal{S}^{(X)}_{\varpi,\ell}(k\chi')\mathcal{P}_X(k, \eta_0 - \chi, \eta_0 - \chi') \\
&\propto \frac{1}{\ell^5} \int_0^{\chi_S} d\chi \frac{1}{\chi} \mathcal{P}_{\mathrm{X}} \left(\ell(\eta_0 - \chi)\chi^{-1}, \ell(\eta_0 - \chi)\chi^{-1}\right) \ , \qquad (8.4.42)
\end{aligned}
$$

where we assume the large-ℓ limit to provide the above relation and we use the so-called Limber approximation. In the above equation, when the multipole is quite large, the contribution from the power spectrum is mainly coming from the sub-horizon power, that is, $k\eta \gg 1$. From Sec. 8.2, we find that the power spectrum on large multipoles ($\ell \gg 1$) for the vector and tensor modes is therefore proportional to $(k\eta)^{-6}$ and $(k\eta)^{-4}$, respectively. We can derive the asymptotic power of the weak lensing curl mode as $\ell^4 C_\ell^{(\mathrm{V})\varpi\varpi} \propto \ell^{-7}$ and $\ell^4 C_\ell^{(\mathrm{T})\varpi\varpi} \propto \ell^{-5}$. From Eq. (8.3.41), angular

power spectra of the CMB lensing and cosmic shear are related as $C_\ell^{\varpi\varpi} \propto \ell^{-4} C_\ell^{BB}$, the asymptotic power of the B-mode cosmic shear can be given as $\ell^2 C_\ell^{(\mathrm{V})BB} \propto \ell^{-5}$ and $\ell^2 C_\ell^{(\mathrm{T})BB} \propto \ell^{-3}$. We can see these asymptotic powers from Fig. 8.2. Note that observed lensing signal is the sum of the vector and tensor modes, i.e., $C_\ell^{(\mathrm{tot})} = C_\ell^{(\mathrm{V})} + C_\ell^{(\mathrm{T})}$.

From here, we discuss the detectability of the texture by using the weak lensing signals. In the case of the CMB lensing, we consider the noise spectrum that is due to the cosmic variance of the CMB, so called the CMB reconstruction noise, assuming a noiseless instrument following Ref. [172]. The CMB reconstruction noise mainly depends on the number of available multipoles. Throughout this chapter, we use the lensed and unlensed CMB angular power spectrum up to $\ell_{\mathrm{max}} = 3000$ when computing the reconstruction noise. On the other hand, the noise spectrum of the cosmic shear observations is determined by the shot noise given by Eq. (8.3.40).

We estimate the signal-to-noise ratio as

$$\left(\frac{\mathrm{S}}{\mathrm{N}}\right)_{<\ell} = \left[\sum_{\ell'=2}^{\ell} \left(\frac{C_{\ell'}}{\Delta C_{\ell'}}\right)^2\right]^{1/2} , \tag{8.4.43}$$

$$\Delta C_\ell = \sqrt{\frac{2}{(2\ell+1) f_{\mathrm{sky}}}} \left(C_\ell + N_\ell\right) . \tag{8.4.44}$$

In Fig. 8.3, we show the relation between the signal-to-noise ratio and the theoretical parameter ϵ_v. We can find that the ultimate experiment of the CMB lensing without including the instrumental noise can set an upper limit on the theoretical parameter related to the VEV as $\epsilon_v \sim 2.7 \times 10^{-6}$.

Constraints from the cosmic shear are much weaker than those from the CMB lensing. This is because signals of the cosmic shear are strongly suppressed on small scales. However, contrary to the CMB lensing observation, the signal-to-noise ratio of cosmic shear experiments depends on parameters of the experimental specification. Fortunately, the theoretical parameter ϵ_v changes only the amplitude of the angular power spectrum, namely, $C_\ell \propto \epsilon_v^2$. From the definition of the signal-to-noise ratio (8.4.43) and (8.4.44), the signal-to-noise ratio therefore depends on the special combination $\epsilon_v^2 N_{\mathrm{g}}$. In Fig. 8.4, we show the relation between the signal-to-noise ratio and $\epsilon_v^2 N_{\mathrm{g}}$ and the mean redshift. From this result, we can give a rough estimation of the signal-to-noise ratio as the function of $\epsilon_v^2 N_{\mathrm{g}}$ and z_{m}, such as $S/N \propto f_{\mathrm{sky}}^{1/2} \left[\epsilon_v^2 N_{\mathrm{g}}\right]^{0.2} z_{\mathrm{m}}^{0.7}$ for the cosmic shear observation. According to this estimation, in order to improve the detectability, we need to push z_{m} to higher redshift rather than adding the number of galaxies N_{g} since the signal-to-noise ratio is sensitive to the mean redshift rather

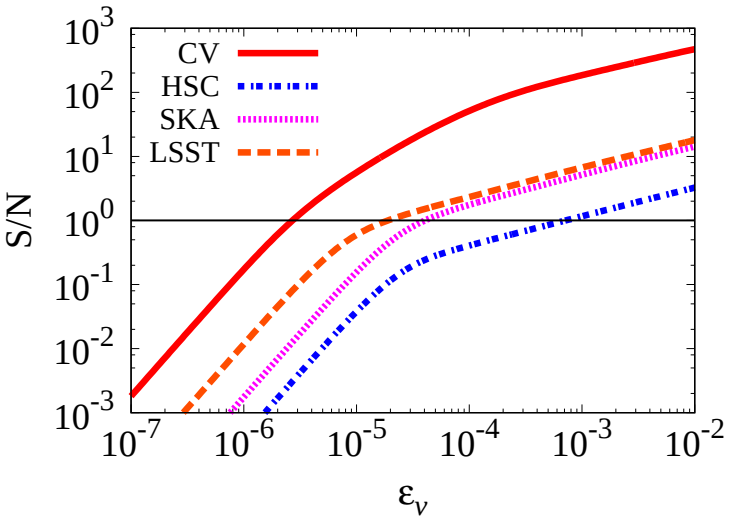

Figure.8.3 The signal-to-noise ratio by varying the theoretical parameter ϵ_v. In the case of the CMB lensing denoted as "CV" in this figure, the noise spectrum is assumed the CMB reconstruction noise [172]. In the cosmic shear case denoted as HSC, SKA, and LSST, we assume the shot noise originated from the intrinsic shape of galaxies in Eq. (8.3.40). In the case of the CMB lensing, we assume the lensing reconstruction noise without the instrumental noise, namely, the cosmic-variance limited noise denoted as CV in this figure. Moreover, for the cosmic shear experiment, we show the signal-to-noise ratio resulting from the HSC, SKA, and LSST experiments. We also show the vertical solid line which corresponds to $S/N = 1$.

than the observing number of galaxies.

Before closing this section, we discuss the validity of the assumption, that is, the totally coherent model. Under the Limber approximation presented in Eq. (8.4.42), the power spectrum on small scales is determined by the equal-time power spectrum, which is the same as the totally coherent model. Therefore, the totally coherent model is valid on small scales.

In Fig. 8.2, we can see that the Limber approximation can explain the cosmic shear B-mode on almost all scales. On the other hand, the angular power spectrum of the curl mode does not correspond to the power of the Limber approximation on large scales, i.e., $\ell \lesssim 100$. We can conclude that the totally coherent model works in the case of the cosmic shear B-mode. Contrary to this, the totally coherent model is not reliable in the case of the CMB lensing curl mode at $\ell \lesssim 100$.

Here, we show the rough estimate for the signal-to-noise ratio in the case of the CMB lensing curl mode. In the worst case, when the contribution from $\ell \lesssim 100$ on

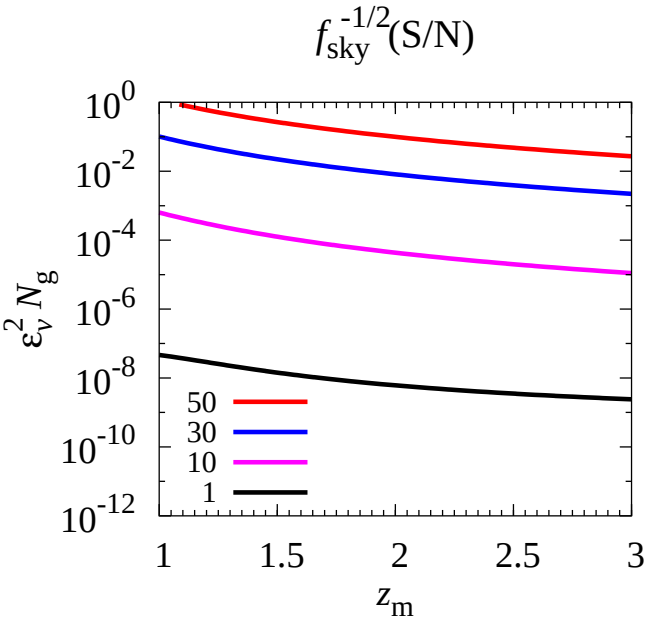

Figure.8.4 The signal-to-noise ratio with the factor $f_{\rm sky}^{-1/2}$ as the function of two parameters $\epsilon_v^2 N_{\rm g}$ and $z_{\rm m}$. This figure shows contours which corresponds to $f_{\rm sky}^{-1/2}(S/N) = 1$, 10, 30, and 50. We set the maximum multipole to estimate the signal-to-noise ratio as $\ell_{\rm max} = 1000$.

the signal-to-noise ratio is negligible, we find that ϵ_v decreases as $\epsilon_v \sim 1.8 \times 10^{-5}$. Although this value is most pessimistic constraint on the theoretical parameter of the texture by using the CMB lensing curl mode, it is comparable to the LSST case in the cosmic shear B-mode observation. Therefore, the constraint on the theoretical parameter is at least $\epsilon_v \lesssim 1.8 \times 10^{-5}$ by using the CMB lensing curl mode.

8.5 Summary

In this chapter, we investigate weak lensing effects from non-topological textures accurately governed by the non-linear sigma model. The phase transitions of the universe induce cosmological defects, e.g., monopoles, strings, or textures. These defects imprint characteristic signatures on cosmological probes such as the CMB fluctuations or the large-scale structure. We can give the constraint on cosmological defects from various observations. Moreover, we can pull information indirectly about cosmological phase transitions which would have happened in the early universe.

We can decompose weak lensing effects into two types of the signature by using the parity. The parity-odd signal in weak lensing effects is induced from only the vector and tensor modes. The dynamics of the non-topological texture is well described by the non-linear sigma model which induces not only scalar but also vector and tensor modes. In order to estimate the weak lensing signal, we need to calculate the unequal-time power spectrum for the vector and tensor modes. Throughout this chapter, to proceed the numerical calculation, we restrict the totally coherent model for the texture which gives the unequal-time power spectrum is written by the separable form. We leave to future work the consideration of any other models of the unequal-time power spectrum.

We present the CMB lensing curl-mode and cosmic shear B-mode from the non-topological texture with the large-N limit. In both observables, we newly find that the tensor mode dominates over the angular power spectrum of the curl and B modes. We estimate the signal-to-noise ratio as a function of the theoretical parameter ϵ_v. The parameter ϵ_v represents the energy scale of the VEV. In the current observations, the upper bound of ϵ_v is roughly obtained from the CMB anisotropies observed by the Planck as $\epsilon_v \lesssim 1.3 \times 10^{-5}$ [63]. Furthermore, the cosmic defects including the texture also induce the CMB spectral distortion [180]. The CMB spectral distortion constrained by the COBE FIRAS [181] also imposes the upper bound as $\epsilon_v \lesssim 1.29 \times 10^{-5}$, which is almost the same upper bound as the CMB anisotropies. Note that, if we naively convert the tension of cosmic strings into the parameter ϵ_v, ϵ_v for cosmic strings reads as $\epsilon_v \lesssim O(10^{-4})$ [63, 94]. The explicit bound depends on the kind of cosmic strings.

From our analysis, we find that the CMB lensing measurement by using the quadratic estimator without the instrumental noise would give an upper limit as $\epsilon_v \sim 2.7 \times 10^{-6}$. In the cosmic shear measurement, we give a relation between the signal-to-noise ratio and the survey design parameters. From this result, improving the mean redshift is effective for studying the non-topological texture in the cosmic shear experiment.

Part.V

Summary

In this thesis, we have investigated observable signatures of cosmic defects focusing on vector and tensor modes of cosmological perturbations. In part I, we reviewed the standard cosmology and the cosmic defects. In chapter 1, we summarized the standard cosmological model and its perturbation theory. We saw that the vector and tensor modes can not be induced in the standard cosmological perturbation theory because these modes are sourceless and only have decaying solutions. In contrast, if we have external vector and tensor sources, these modes are produced in the universe. In chapter 2, we introduced phase transitions of scalar fields due to temperature decrease of the universe and their resulting cosmological defects. In particular, we focused on the cosmic strings and textures, and we derived their equation of motions and energy momentum tensors. In this thesis, we considered cosmic strings and textures, as the sources of vector and tensor modes.

In part II, we described the magnetic fields generation on cosmological scales from cosmic strings and textures. In chapter 3, we studied magnetic fields generated by the Harrison mechanism where the relative velocity between the photon and baryon fluids in the vector perturbation plays an important role. Considering the Euler equations for the photon and baryon fluids and using the tight coupling approximation between them, we obtained the relative velocity from which we evaluated magnetic fields. In chapter 4, we discussed the generation of primordial magnetic fields from the cosmic string network according to [1]. We considered the vector perturbations from the cosmic string network by summing up the contributions from individual strings. We adopted the velocity-dependent one-scale (VOS) model for the string network model. Treating the vector perturbations from the string network as the source of the relative velocity, we estimated the magnetic fields from the cosmic string network as $B_{\rm string} \sim 10^{-25}(G\mu/10^{-6})$ Gauss at about 100Mpc scale. In chapter 5, in the same concept as in chapter 4, we estimated the primordial magnetic fields from the self-ordering scalar fields, called textures 1, according to [2]. We used the non-linear sigma model (NLSM) to represent the self-ordering scalar fields, and gave the analytical form for the scalar field dynamics. We calculated the vector perturbations from the texture to estimate the relative velocity between photon and baryon fluids. Then in the same way as in the case of the cosmic string network, the magnetic fields are produced via the Harrison mechanism, and the resulting magnetic fields we found are $B_{\rm texture} \sim 10^{-19}\epsilon_v$ Gauss at about 100 Mpc scale.

In part III, we represented the gravitational waves power spectrum from kinks on cosmic infinite strings. We introduced the primordial gravitational waves and kinks on

infinite strings in chapter 6. We showed that the quadrupole motion of cosmic infinite strings can produce the gravitational waves, especially from sharp structures called kinks. We reviewed the production, evolution, and distribution of kinks on infinite strings in chapter 6. Then we estimated the primordial gravitational waves from kinks on strings according to [3] in chapter 7. Here we calculated the gravitational wave spectrum considering the time evolution of the distribution of kinks on strings and that of the string network using the VOS model. In previous works, the gravitational wave from the infinite string network had been calculated analytically assuming the scaling law of the number of strings in the horizon based on the VOS model in matter and radiation dominated epochs separately. In this work, we numerically solved the evolution of the distribution of kinks and the evolution of the scaling law of cosmic infinite strings simultaneously. Then we obtained $\mathcal{O}(10^2)$ times larger gravitational waves comparing with the previous analytical work at some scales, because we take into account the variation of the values of strings, such as the correlation length, in the transition phase between the radiation and matter dominated epochs correctly. The resulting spectrum is $\Omega_{\rm gw}^{\rm string} \sim 10^{-8}(G\mu/10^{-6})^2$ at 10^{-8}Hz. Considering this gravitational wave signals, aLIGO, SKA and DECIGO could test the infinite cosmic strings whose densities are $G\mu > 10^{-7}$, $G\mu > 10^{-9}$ and $G\mu > 10^{-10}$, respectively.

In part IV, we studied the weak lensing signals from the self-ordering scalar fields. We considered the weak lensing signals from only the vector and tensor perturbations, that show parity odd configurations namely the CMB lensing curl mode and the cosmic shear B mode. We could estimate the CMB lensing curl mode by considering the reconstruction of the curl mode of the lensing angle from the CMB using the quadratic estimator, and the cosmic shear B mode could be obtained by decomposing the reduced shear of galaxies into the spin-weighted spherical harmonics. In chapter 8, we calculated the spectra of the CMB lensing curl mode and the cosmic shear B mode originated in the self-ordering scalar fields, and forecasted their detectability according to [4]. In this thesis, we estimated the vector and tensor perturbations from the texture described by the NLSM. Then we calculated the parity odd weak lensing signals originated in the vector and tensor perturbations which are induced by the texture. Here we found that both of the parity odd weak lensing signals are produced mainly by the power spectra of the NLSM at sub-horizon scales, and the tensor contribution is dominant. Their ℓ-dependence can be written as $\ell^4 C_{\ell,\rm V}^{\varpi\varpi} \propto \ell^{-7}$, $\ell^4 C_{\ell,\rm T}^{\varpi\varpi} \propto \ell^{-5}$ and $\ell^2 C_{\ell,\rm V}^{\rm BB} \propto \ell^{-5}$, $\ell^2 C_{\ell,\rm T}^{\rm BB} \propto \ell^{-3}$. For the case of the CMB lensing, considering the ideal experiment without the instrumental noise, we could obtain

the upper limit for the combination of the VEV and the number of scalar fields ϵ_v as $\epsilon_v \leq 2.7 \times 10^{-6}$. For the case of the cosmic shear B mode, allowing the mean redshift $z_{\rm m}$ and the combination $\epsilon_v^2 N_{\rm g}$ to vary, we obtained the signal to noise ratio contour. Fitting that contour, we found that the signal to noise ratio can be written as $S/N \propto [\epsilon_v^2 N_{\rm g}]^{0.2} z_{\rm m}^{0.7}$, and we concluded that we should push the mean redshift $z_{\rm m}$ higher rather than counting more number of galaxies to find the texture.

We hope that these observable signatures could be used in future to find evidence of the existence of cosmic defects and phase transitions that the defects were originated from.

Acknowledgement

I want to thank all the people who related with this work. At first, I would like to thank professor Naoshi Sugiyama for careful discussions and giving me opportunities to study such interesting subjects. I'm grateful to associate professor Kiyotomo Ichiki for detail discussions of each subject. I would also like to thank the members of the authors of our papers [1, 2, 3, 4], Dr. S.Kuroyanagi, Dr. D.Nitta, Dr. T.Sekiguchi, Dr. S.Saga and Ms. Y.Matsui for useful discussions. I would like to take this opportunity to thank the members of our laboratory, especially, Mr. M.Kobayashi for many detailed assistance with a lot of points. This work is supported by a Grant-in-aid for Japan Society for Promotion of Science Research under Grants No. 15J05029 (K.H.). At the end, I would like to express the deepest appreciation to my family for helping me for a lot of years.

Reference

[1] K. Horiguchi, K. Ichiki, and N. Sugiyama, *Primordial magnetic fields from the string network*, Progress of Theoretical and Experimental Physics **2016** (Aug., 2016) 083E02, [arXiv:1601.0105].

[2] K. Horiguchi, K. Ichiki, T. Sekiguchi, and N. Sugiyama, *Primordial magnetic fields from self-ordering scalar fields*, JCAP **1504** (2015), no. 04 007, [arXiv:1501.0630].

[3] Y. Matsui, K. Horiguchi, D. Nitta, and S. Kuroyanagi, *Improved calculation of the gravitational wave spectrum from kinks on infinite cosmic strings*, jcap **11** (Nov., 2016) 005, [arXiv:1605.0876].

[4] S. Saga, K. Horiguchi, and K. Ichiki, *Weak lensing from self-ordering scalar fields*, prd **95** (June, 2017) 123524, [arXiv:1612.0400].

[5] A. A. Penzias and R. W. Wilson, *A Measurement of Excess Antenna Temperature at 4080 Mc/s.*, apj **142** (July, 1965) 419–421.

[6] H. Georgi and S. L. Glashow, *Unity of All Elementary Particle Forces*, Phys. Rev. Lett. **32** (1974) 438–441.

[7] G. Ross, Grand unified theories. Frontiers in physics. Benjamin/Cummings Pub. Co., 1984.

[8] T. W. B. Kibble, *Topology of cosmic domains and strings*, Journal of Physics A Mathematical General **9** (Aug., 1976) 1387–1398.

[9] A. Friedmann, *Über die Krümmung des Raumes*, Zeitschrift fur Physik **10** (1922) 377–386.

[10] G. Lemaître, *Un Univers homogène de masse constante et de rayon croissant rendant compte de la vitesse radiale des nébuleuses extra-galactiques*, Annales de la Société Scientifique de Bruxelles **47** (1927) 49–59.

[11] A. Einstein, *Die Grundlage der allgemeinen Relativitätstheorie*, Annalen der Physik **354** (1916) 769–822.

[12] G. Gamow, *Expanding Universe and the Origin of Elements*, Physical Review

70 (Oct., 1946) 572–573.

[13] R. A. Alpher, H. Bethe, and G. Gamow, *The Origin of Chemical Elements*, Physical Review **73** (Apr., 1948) 803–804.

[14] E. Hubble, *A Relation between Distance and Radial Velocity among Extra-Galactic Nebulae*, Proceedings of the National Academy of Science **15** (Mar., 1929) 168–173.

[15] S. Perlmutter, G. Aldering, G. Goldhaber, R. A. Knop, P. Nugent, P. G. Castro, S. Deustua, S. Fabbro, A. Goobar, D. E. Groom, I. M. Hook, A. G. Kim, M. Y. Kim, J. C. Lee, N. J. Nunes, R. Pain, C. R. Pennypacker, R. Quimby, C. Lidman, R. S. Ellis, M. Irwin, R. G. McMahon, P. Ruiz-Lapuente, N. Walton, B. Schaefer, B. J. Boyle, A. V. Filippenko, T. Matheson, A. S. Fruchter, N. Panagia, H. J. M. Newberg, W. J. Couch, and T. S. C. Project, *Measurements of* Ω *and* Λ *from 42 High-Redshift Supernovae*, apj **517** (June, 1999) 565–586, [astro-ph/9812133].

[16] A. G. Riess, A. V. Filippenko, P. Challis, A. Clocchiatti, A. Diercks, P. M. Garnavich, R. L. Gilliland, C. J. Hogan, S. Jha, R. P. Kirshner, B. Leibundgut, M. M. Phillips, D. Reiss, B. P. Schmidt, R. A. Schommer, R. C. Smith, J. Spyromilio, C. Stubbs, N. B. Suntzeff, and J. Tonry, *Observational Evidence from Supernovae for an Accelerating Universe and a Cosmological Constant*, aj **116** (Sept., 1998) 1009–1038, [astro-ph/9805201].

[17] G. Hinshaw, D. N. Spergel, L. Verde, R. S. Hill, S. S. Meyer, C. Barnes, C. L. Bennett, M. Halpern, N. Jarosik, A. Kogut, E. Komatsu, M. Limon, L. Page, G. S. Tucker, J. L. Weiland, E. Wollack, and E. L. Wright, *First-Year Wilkinson Microwave Anisotropy Probe (WMAP) Observations: The Angular Power Spectrum*, apjs **148** (Sept., 2003) 135–159, [astro-ph/0302217].

[18] G. Hinshaw, D. Larson, E. Komatsu, D. N. Spergel, C. L. Bennett, J. Dunkley, M. R. Nolta, M. Halpern, R. S. Hill, N. Odegard, L. Page, K. M. Smith, J. L. Weiland, B. Gold, N. Jarosik, A. Kogut, M. Limon, S. S. Meyer, G. S. Tucker, E. Wollack, and E. L. Wright, *Nine-year Wilkinson Microwave Anisotropy Probe (WMAP) Observations: Cosmological Parameter Results*, apjs **208** (Oct., 2013) 19, [arXiv:1212.5226].

[19] Planck Collaboration, N. Aghanim, M. Arnaud, M. Ashdown, J. Aumont, C. Baccigalupi, A. J. Banday, R. B. Barreiro, J. G. Bartlett, N. Bartolo, and et al., *Planck 2015 results. XI. CMB power spectra, likelihoods, and robustness of parameters*, aap **594** (Sept., 2016) A11, [arXiv:1507.0270].

[20] **Planck** Collaboration, P. A. R. Ade et al., *Planck 2015 results. XIII. Cosmological parameters*, Astron. Astrophys. **594** (2016) A13, [arXiv:1502.0158].

[21] J. M. Stewart, *Perturbations of Friedmann-Robertson-Walker cosmological models*, Classical and Quantum Gravity **7** (July, 1990) 1169–1180.

[22] C.-P. Ma and E. Bertschinger, *Cosmological perturbation theory in the synchronous and conformal Newtonian gauges*, Astrophys.J. **455** (1995) 7–25, [astro-ph/9506072].

[23] M. Shiraishi, Probing the Early Universe with the CMB Scalar, Vector and Tensor Bispectrum. 2013.

[24] E. J. Weinberg, *Radiative Corrections as the Origin of Spontaneous Symmetry Breaking*, ArXiv High Energy Physics - Theory e-prints (July, 2005) [hep-th/0507214].

[25] J. I. Kapusta, Finite-temperature field theory. 1989.

[26] M. Laine, *Thermal phase transitions in cosmology*, ArXiv High Energy Physics - Phenomenology e-prints (Nov., 2001) [hep-ph/0111349].

[27] N. Straumann, *Cosmological Phase Transitions*, ArXiv Astrophysics e-prints (Sept., 2004) [astro-ph/0409042].

[28] A. Vilenkin, *Cosmic strings and domain walls.*, physrep **121** (1985) 263–315.

[29] V. Mukhanov, Physical Foundations of Cosmology. Cambridge Univ. Press, Cambridge, 2005.

[30] W. de Boer, *Grand unified theories and supersymmetry in particle physics and cosmology*, Progress in Particle and Nuclear Physics **33** (1994) 201–301, [hep-ph/9402266].

[31] U.-L. Pen, *Cosmic defects*, New Astronomy Reviews **45** (2001), no. 4 271 – 276. Understanding the Universe at the close of the 20th century.

[32] L. Pogosian and T. Vachaspati, *Cosmic microwave background anisotropy from wiggly strings*, prd **60** (Oct., 1999) 083504, [astro-ph/9903361].

[33] B. Carter, *Integrable equation of state for noisy cosmic string*, Phys. Rev. D **41** (Jun, 1990) 3869–3872.

[34] D. P. Bennett and F. m. c. R. Bouchet, *High-resolution simulations of cosmic-string evolution. i. network evolution*, Phys. Rev. D **41** (Apr, 1990) 2408–2433.

[35] G. Gibbons, S. Hawking, and T. Vachaspati, The Formation and evolution of

cosmic strings. Cambridge University Press, 1990.

[36] A. Vilenkin, *Effect of small-scale structure on the dynamics of cosmic strings*, Phys. Rev. D **41** (May, 1990) 3038–3040.

[37] B. Allen and E. P. S. Shellard, *Cosmic-string evolution: A numerical simulation*, Phys. Rev. Lett. **64** (Jan, 1990) 119–122.

[38] T. W. B. Kibble, *Evolution of a system of cosmic strings*, Nuclear Physics B **252** (1985) 227–244.

[39] D. P. Bennett, *Evolution of cosmic strings. ii*, Phys. Rev. D **34** (Dec, 1986) 3592–3607.

[40] C. Martins and E. Shellard, *Quantitative string evolution*, Phys.Rev. **D54** (1996) 2535–2556, [hep-ph/9602271].

[41] C. J. Martins and E. P. Shellard, *Extending the velocity-dependent one-scale string evolution model*, prd **65** (Feb., 2002) 043514, [hep-ph/0003298].

[42] T. Damour and A. Vilenkin, *Gravitational wave bursts from cusps and kinks on cosmic strings*, Phys. Rev. D **64** (Aug, 2001) 064008.

[43] A. Albrecht, R. A. Battye, and J. Robinson, *Detailed study of defect models for cosmic structure formation*, Phys. Rev. D **59** (Dec, 1998) 023508.

[44] K. Jones-Smith, L. M. Krauss, and H. Mathur, *A Nearly Scale Invariant Spectrum of Gravitational Radiation from Global Phase Transitions*, Phys.Rev.Lett. **100** (2008) 131302, [arXiv:0712.0778].

[45] E. Fenu, D. G. Figueroa, R. Durrer, and J. García-Bellido, *Gravitational waves from self-ordering scalar fields*, jcap **10** (Oct., 2009) 5, [arXiv:0908.0425].

[46] S. Saga, K. Ichiki, K. Takahashi, and N. Sugiyama, *Magnetic field spectrum at cosmological recombination revisited*, prd **91** (June, 2015) 123510, [arXiv:1504.0379].

[47] A. Lewis, *Observable primordial vector modes*, prd **70** (Aug., 2004) 043518, [astro-ph/0403583].

[48] A. Challinor and A. Lasenby, *Cosmic Microwave Background Anisotropies in the Cold Dark Matter Model: A Covariant and Gauge-invariant Approach*, apj **513** (Mar., 1999) 1–22, [astro-ph/9804301].

[49] A. Challinor, *Microwave background polarization in cosmological models*, prd **62** (Aug., 2000) 043004, [astro-ph/9911481].

[50] K. Ichiki, K. Takahashi, N. Sugiyama, H. Hanayama, and H. Ohno, *Magnetic Field Spectrum at Cosmological Recombination*, ArXiv Astrophysics e-prints (Jan., 2007) [astro-ph/0701329].

[51] T. Vachaspati, L. Pogosian, and D. Steer, *Cosmic Strings*, ArXiv e-prints (June, 2015) [arXiv:1506.0403].

[52] T. Damour and A. Vilenkin, *Gravitational Wave Bursts from Cosmic Strings*, Physical Review Letters **85** (Oct., 2000) 3761, [gr-qc/0004075].

[53] S. Kuroyanagi, K. Miyamoto, T. Sekiguchi, K. Takahashi, and J. Silk, *Forecast constraints on cosmic string parameters from gravitational wave direct detection experiments*, prd **86** (July, 2012) 023503, [arXiv:1202.3032].

[54] J. J. Blanco-Pillado, K. D. Olum, and B. Shlaer, *Number of cosmic string loops*, prd **89** (Jan., 2014) 023512, [arXiv:1309.6637].

[55] M. Kawasaki, K. Miyamoto, and K. Nakayama, *Gravitational waves from kinks on infinite cosmic strings*, Phys. Rev. **D81** (2010) 103523, [arXiv:1002.0652].

[56] K. J. Mack, D. H. Wesley, and L. J. King, *Observing cosmic string loops with gravitational lensing surveys*, prd **76** (Dec., 2007) 123515, [astro-ph/0702648].

[57] K. Kuijken, X. Siemens, and T. Vachaspati, *Microlensing by cosmic strings*, mnras **384** (Feb., 2008) 161–164, [arXiv:0707.2971].

[58] A. Avgoustidis, E. J. Copeland, A. Moss, and D. Skliros, *Fast analytic computation of cosmic string power spectra*, prd **86** (Dec., 2012) 123513, [arXiv:1209.2461].

[59] P. Bhattacharjee, *Origin and propagation of extremely high energy cosmic rays*, physrep **327** (Mar., 2000) 109–247, [astro-ph/9811011].

[60] T. Vachaspati, *Cosmic rays from cosmic strings with condensates*, prd **81** (Feb., 2010) 043531, [arXiv:0911.2655].

[61] K. Jones-Smith, H. Mathur, and T. Vachaspati, *Aharonov-Bohm radiation*, prd **81** (Feb., 2010) 043503, [arXiv:0911.0682].

[62] D. A. Steer and T. Vachaspati, *Light from cosmic strings*, prd **83** (Feb., 2011) 043528, [arXiv:1012.1998].

[63] Planck Collaboration, P. A. R. Ade, N. Aghanim, C. Armitage-Caplan, M. Arnaud, M. Ashdown, F. Atrio-Barandela, J. Aumont, C. Baccigalupi, A. J. Banday, and et al., *Planck 2013 results. XXV. Searches for cosmic strings and other topological defects*, aap **571** (Nov., 2014) A25, [arXiv:1303.5085].

[64] D. Ryu, H. Kang, J. Cho, and S. Das, *Turbulence and Magnetic Fields in the Large-Scale Structure of the Universe*, Science **320** (May, 2008) 909, [arXiv:0805.2466].

[65] C. Vogt and T. A. Ensslin, *A Bayesian view on Faraday rotation maps Seeing the magnetic power spectra in galaxy clusters*, aap **434** (Apr., 2005) 67–76, [astro-ph/0501211].

[66] A. Neronov and I. Vovk, *Evidence for Strong Extragalactic Magnetic Fields from Fermi Observations of TeV Blazars*, Science **328** (Apr., 2010) 73–, [arXiv:1006.3504].

[67] S. Bertone, C. Vogt, and T. Ensslin, *Magnetic field seeding by galactic winds*, mnras **370** (July, 2006) 319–330, [astro-ph/0604462].

[68] T. Vachaspati and A. Vilenkin, *Large-scale structure from wiggly cosmic strings*, Phys. Rev. Lett. **67** (Aug, 1991) 1057–1061.

[69] D. N. Vollick, *Cosmic string shocks, magnetic fields, and microwave anisotropies*, Phys. Rev. D **48** (Oct, 1993) 3585–3591.

[70] T. Vachaspati, *Structure of wiggly-cosmic-string wakes*, Phys. Rev. D **45** (May, 1992) 3487–3496.

[71] P. P. Avelino and E. P. S. Shellard, *Dynamical friction on cosmic string motion and magnetic field generation*, Phys. Rev. D **51** (May, 1995) 5946–5949.

[72] L. Hollenstein, C. Caprini, R. Crittenden, and R. Maartens, *Challenges for creating magnetic fields by cosmic defects*, prd **77** (Mar., 2008) 063517, [arXiv:0712.1667].

[73] "http://www.sfu.ca/~levon/cmbact.html."

[74] K. Horiguchi, K. Ichiki, T. Sekiguchi, and N. Sugiyama, *Primordial magnetic fields from self-ordering scalar fields*, jcap **4** (Apr., 2015) 7, [arXiv:1501.0630].

[75] K. Takahashi, K. Ichiki, H. Ohno, and H. Hanayama, *Magnetic Field Generation from Cosmological Perturbations*, Physical Review Letters **95** (Sept., 2005) 121301, [astro-ph/0502283].

[76] K. Takahashi, K. Ichiki, H. Ohno, H. Hanayama, and N. Sugiyama, *Generation of magnetic field from cosmological perturbations*, ArXiv Astrophysics e-prints (Jan., 2006) [astro-ph/0601243].

[77] K. Ichiki, K. Takahashi, and N. Sugiyama, *Constraint on the primordial vector mode and its magnetic field generation from seven-year Wilkinson Microwave Anisotropy Probe observations*, prd **85** (Feb., 2012) 043009, [arXiv:1112.4705].

[78] S. Saga, M. Shiraishi, K. Ichiki, and N. Sugiyama, *Generation of magnetic fields in Einstein-aether gravity*, prd **87** (May, 2013) 104025,

[arXiv:1302.4189].

[79] W. Hu and N. Sugiyama, *Anisotropies in the cosmic microwave background: an analytic approach*, apj **444** (May, 1995) 489–506, [astro-ph/9407093].

[80] M. A. Latif, D. R. G. Schleicher, and W. Schmidt, *Magnetic fields during the formation of supermassive black holes*, mnras **440** (May, 2014) 1551–1561, [arXiv:1310.3680].

[81] T. Venumadhav, A. Oklopcic, V. Gluscevic, A. Mishra, and C. M. Hirata, *A new probe of magnetic fields in the pre-reionization epoch: I. Formalism*, ArXiv e-prints (Oct., 2014) [arXiv:1410.2250].

[82] R. Durrer, *Gauge invariant cosmological perturbation theory: A General study and its application to the texture scenario of structure formation*, Fund.Cosmic Phys. **15** (1994) 209, [astro-ph/9311041].

[83] R. Durrer, A. Gangui, and M. Sakellariadou, *Doppler peaks: A Fingerprint of topological defects*, Phys.Rev.Lett. **76** (1996) 579–582, [astro-ph/9507035].

[84] R. Durrer, M. Kunz, and A. Melchiorri, *Cosmic microwave background anisotropies from scaling seeds: Global defect models*, Phys.Rev. **D59** (1999) 123005, [astro-ph/9811174].

[85] U.-L. Pen, U. Seljak, and N. Turok, *Power spectra in global defect theories of cosmic structure formation*, Phys.Rev.Lett. **79** (1997) 1611–1614, [astro-ph/9704165].

[86] J.-F. Dufaux, D. G. Figueroa, and J. García-Bellido, *Gravitational waves from Abelian gauge fields and cosmic strings at preheating*, Phys. Rev. D **82** (Oct., 2010) 083518, [arXiv:1006.0217].

[87] J. T. Giblin, Jr., L. R. Price, X. Siemens, and B. Vlcek, *Gravitational waves from global second order phase transitions*, jcap **11** (Nov., 2012) 6, [arXiv:1111.4014].

[88] D. G. Figueroa, M. Hindmarsh, and J. Urrestilla, *Exact Scale-Invariant Background of Gravitational Waves from Cosmic Defects*, Physical Review Letters **110** (Mar., 2013) 101302, [arXiv:1212.5458].

[89] C. Hill, D. Schramm, and T. Walker, *Ultra-high-energy cosmic rays from superconducting cosmic strings*, Phys. Rev. D **36** (Aug, 1987) 1007–1016.

[90] A. J. Gill and T. W. B. Kibble, *Cosmic rays from cosmic strings*, prd **50** (Sept., 1994) 3660–3665, [hep-ph/9403395].

[91] M. Pospelov, S. Pustelny, M. P. Ledbetter, D. F. J. Kimball, W. Gawlik, and D. Budker, *Detecting domain walls of axionlike models using terrestrial*

experiments, Phys. Rev. Lett. **110** (Jan, 2013) 021803.

[92] V. Stadnik, Y. and V. Flambaum, V. *Searching for topological defect dark matter via nongravitational signatures*, Phys. Rev. Lett. **113** (Oct, 2014) 151301.

[93] R. Durrer, M. Kunz, and A. Melchiorri, *Cosmic structure formation with topological defects*, Phys. Rep. **364** (June, 2002) 1–81, [astro-ph/0110348].

[94] J. Urrestilla, N. Bevis, M. Hindmarsh, and M. Kunz, *Cosmic string parameter constraints and model analysis using small scale Cosmic Microwave Background data*, jcap **12** (Dec., 2011) 021, [arXiv:1108.2730].

[95] **BICEP2 Collaboration** Collaboration, P. Ade et al., *Detection of B-Mode Polarization at Degree Angular Scales by BICEP2*, Phys.Rev.Lett. **112** (2014) 241101, [arXiv:1403.3985].

[96] L. M. Krauss, *Gravitational waves from global phase transitions*, Phys.Lett. **B284** (1992) 229–233.

[97] E. Fenu, D. G. Figueroa, R. Durrer, J. Garcia-Bellido, and M. Kunz, *Cosmic Microwave Background temperature and polarization anisotropies from the large-N limit of global defects*, arXiv:1311.3225.

[98] R. Durrer, D. G. Figueroa, and M. Kunz, *Can Self-Ordering Scalar Fields explain the BICEP2 B-mode signal?*, JCAP **1408** (2014) 029, [arXiv:1404.3855].

[99] J. Lizarraga, J. Urrestilla, D. Daverio, M. Hindmarsh, M. Kunz, et al., *Constraining topological defects with temperature and polarization anisotropies*, arXiv:1408.4126.

[100] K. L. Pandey and S. K. Sethi, *Probing Primordial Magnetic Fields Using Lyα Clouds*, apj **762** (Jan., 2013) 15, [arXiv:1210.3298].

[101] M. L. Bernet, F. Miniati, S. J. Lilly, P. P. Kronberg, and M. Dessauges-Zavadsky, *Strong magnetic fields in normal galaxies at high redshifts*, Nature **454** (2008) 302–304, [arXiv:0807.3347].

[102] **Planck Collaboration** Collaboration, P. Ade et al., *Planck 2013 results. XVI. Cosmological parameters*, Astron.Astrophys. (2014) [arXiv:1303.5076].

[103] S. Saga, M. Shiraishi, K. Ichiki, and N. Sugiyama, *Generation of magnetic fields in Einstein-Aether gravity*, Phys.Rev. **D87** (2013), no. 10 104025, [arXiv:1302.4189].

[104] T. Damour and A. Vilenkin, *Gravitational radiation from cosmic (super)strings: Bursts, stochastic background, and observational windows*,

Phys. Rev. **D71** (2005) 063510, [hep-th/0410222].

[105] X. Siemens, V. Mandic, and J. Creighton, *Gravitational wave stochastic background from cosmic (super)strings*, Phys. Rev. Lett. **98** (2007) 111101, [astro-ph/0610920].

[106] M. R. DePies and C. J. Hogan, *Stochastic Gravitational Wave Background from Light Cosmic Strings*, Phys. Rev. **D75** (2007) 125006, [astro-ph/0702335].

[107] S. Olmez, V. Mandic, and X. Siemens, *Gravitational-Wave Stochastic Background from Kinks and Cusps on Cosmic Strings*, Phys. Rev. **D81** (2010) 104028, [arXiv:1004.0890].

[108] P. Binetruy, A. Bohe, T. Hertog, and D. A. Steer, *Gravitational wave signatures from kink proliferation on cosmic (super-) strings*, Phys. Rev. **D82** (2010) 126007, [arXiv:1009.2484].

[109] S. A. Sanidas, R. A. Battye, and B. W. Stappers, *Constraints on cosmic string tension imposed by the limit on the stochastic gravitational wave background from the European Pulsar Timing Array*, Phys. Rev. **D85** (2012) 122003, [arXiv:1201.2419].

[110] S. A. Sanidas, R. A. Battye, and B. W. Stappers, *Projected constraints on the cosmic (super)string tension with future gravitational wave detection experiments*, Astrophys. J. **764** (2013) 108, [arXiv:1211.5042].

[111] P. Binetruy, A. Bohe, C. Caprini, and J.-F. Dufaux, *Cosmological Backgrounds of Gravitational Waves and eLISA/NGO: Phase Transitions, Cosmic Strings and Other Sources*, JCAP **1206** (2012) 027, [arXiv:1201.0983].

[112] S. Kuroyanagi, K. Miyamoto, T. Sekiguchi, K. Takahashi, and J. Silk, *Forecast constraints on cosmic strings from future CMB, pulsar timing and gravitational wave direct detection experiments*, Phys. Rev. **D87** (2013), no. 2 023522, [arXiv:1210.2829]. [Erratum: Phys. Rev.D87,no.6,069903(2013)].

[113] L. Sousa and P. P. Avelino, *Stochastic Gravitational Wave Background generated by Cosmic String Networks: Velocity-Dependent One-Scale model versus Scale-Invariant Evolution*, Phys. Rev. **D88** (2013), no. 2 023516, [arXiv:1304.2445].

[114] A. Einstein, *Näherungsweise Integration der Feldgleichungen der Gravitation*, Sitzungsberichte der Königlich Preußischen Akademie der Wissenschaften (Berlin), Seite 688-696. (1916).

[115] A. Einstein, *Über Gravitationswellen*, Sitzungsberichte der Königlich

Preußischen Akademie der Wissenschaften (Berlin), Seite 154-167. (1918).

[116] A. Vilenkin, *Gravitational radiation from cosmic strings*, Phys. Lett. **107B** (1981) 47–50.

[117] E. J. Copeland and T. W. B. Kibble, *Kinks and small-scale structure on cosmic strings*, Phys. Rev. **D80** (2009) 123523, [arXiv:0909.1960].

[118] T. W. B. Kibble and E. J. Copeland, *Evolution of small scale structure on cosmic strings*, Phys. Scripta **T36** (1991) 153–166.

[119] A. Albrecht and N. Turok, *Evolution of cosmic string networks*, prd **40** (Aug., 1989) 973–1001.

[120] D. P. Bennett and F. R. Bouchet, *Cosmic string evolution*, Phys. Rev. Lett. **63** (1989) 2776.

[121] J. P. W. Verbiest et al., *The International Pulsar Timing Array: First Data Release*, Mon. Not. Roy. Astron. Soc. **458** (2016), no. 2 1267–1288, [arXiv:1602.0364].

[122] G. Janssen et al., *Gravitational wave astronomy with the SKA*, PoS **AASKA14** (2015) 037, [arXiv:1501.0012].

[123] P. Amaro-Seoane et al., *eLISA/NGO: Astrophysics and cosmology in the gravitational-wave millihertz regime*, GW Notes **6** (2013) 4–110, [arXiv:1201.3621].

[124] P. Amaro-Seoane et al., *Low-frequency gravitational-wave science with eLISA/NGO*, Class. Quant. Grav. **29** (2012) 124016, [arXiv:1202.0839].

[125] N. Seto, S. Kawamura, and T. Nakamura, *Possibility of direct measurement of the acceleration of the universe using 0.1-Hz band laser interferometer gravitational wave antenna in space*, Phys. Rev. Lett. **87** (2001) 221103, [astro-ph/0108011].

[126] S. Kawamura et al., *The Japanese space gravitational wave antenna: DECIGO*, Class. Quant. Grav. **28** (2011) 094011.

[127] **LIGO Scientific** Collaboration, G. M. Harry, *Advanced LIGO: The next generation of gravitational wave detectors*, Class. Quant. Grav. **27** (2010) 084006.

[128] T. Accadia et al., *Status of the Virgo project*, Class. Quant. Grav. **28** (2011) 114002.

[129] **KAGRA** Collaboration, K. Somiya, *Detector configuration of KAGRA: The Japanese cryogenic gravitational-wave detector*, Class. Quant. Grav. **29** (2012) 124007, [arXiv:1111.7185].

[130] C. J. Hogan and M. J. Rees, *Gravitational interactions of cosmic strings*, Nature **311** (1984) 109–113.

[131] M. Sakellariadou, *Gravitational waves emitted from infinite strings*, Phys. Rev. **D42** (1990) 354–360. [Erratum: Phys. Rev.D43,4150(1991)].

[132] R. R. Caldwell and B. Allen, *Cosmological constraints on cosmic string gravitational radiation*, Phys. Rev. **D45** (1992) 3447–3468.

[133] R. R. Caldwell, R. A. Battye, and E. P. S. Shellard, *Relic gravitational waves from cosmic strings: Updated constraints and opportunities for detection*, Phys. Rev. **D54** (1996) 7146–7152, [astro-ph/9607130].

[134] D. P. Bennett and F. R. Bouchet, *Evidence for a Scaling Solution in Cosmic String Evolution*, Phys. Rev. Lett. **60** (1988) 257.

[135] D. P. Bennett and F. R. Bouchet, *High resolution simulations of cosmic string evolution. 1. Network evolution*, Phys. Rev. **D41** (1990) 2408.

[136] B. Allen and E. P. S. Shellard, *Cosmic string evolution: a numerical simulation*, Phys. Rev. Lett. **64** (1990) 119–122.

[137] G. R. Vincent, M. Hindmarsh, and M. Sakellariadou, *Scaling and small scale structure in cosmic string networks*, Phys. Rev. **D56** (1997) 637–646, [astro-ph/9612135].

[138] V. Vanchurin, K. D. Olum, and A. Vilenkin, *Scaling of cosmic string loops*, Phys. Rev. **D74** (2006) 063527, [gr-qc/0511159].

[139] C. Ringeval, M. Sakellariadou, and F. Bouchet, *Cosmological evolution of cosmic string loops*, JCAP **0702** (2007) 023, [astro-ph/0511646].

[140] C. J. A. P. Martins and E. P. S. Shellard, *Fractal properties and small-scale structure of cosmic string networks*, Phys. Rev. **D73** (2006) 043515, [astro-ph/0511792].

[141] C. J. A. P. Martins and E. P. S. Shellard, *Extending the velocity dependent one scale string evolution model*, Phys. Rev. **D65** (2002) 043514, [hep-ph/0003298].

[142] D. Austin, E. J. Copeland, and T. W. B. Kibble, *Evolution of cosmic string configurations*, Phys. Rev. **D48** (1993) 5594–5627, [hep-ph/9307325].

[143] L. Sousa and P. P. Avelino, *Probing Cosmic Superstrings with Gravitational Waves*, Phys. Rev. **D94** (2016), no. 6 063529, [arXiv:1606.0558].

[144] M. B. Hindmarsh and T. W. B. Kibble, *Cosmic strings*, Rept. Prog. Phys. **58** (1995) 477–562, [hep-ph/9411342].

[145] D. Yamauchi, T. Namikawa, and A. Taruya, *Weak lensing generated by vector*

perturbations and detectability of cosmic strings, JCAP **1210** (2012) 030, [arXiv:1205.2139].

[146] D. Yamauchi, K. Takahashi, Y. Sendouda, and C.-M. Yoo, *Weak lensing of CMB by cosmic (super-)strings*, Phys. Rev. **D85** (2012) 103515, [arXiv:1110.0556].

[147] T. Namikawa, D. Yamauchi, and A. Taruya, *Constraining cosmic string parameters with curl mode of CMB lensing*, Phys. Rev. **D88** (2013), no. 8 083525, [arXiv:1308.6068].

[148] N. Turok, *Global texture as the origin of cosmic structure*, Phys. Rev. Lett. **63** (Dec, 1989) 2625–2628.

[149] N. Turok and D. N. Spergel, *Scaling solution for cosmological σ models at large N*, Phys. Rev. Lett. **66** (Jun, 1991) 3093–3096.

[150] M. Kunz and R. Durrer, *Microwave background anisotropies induced by global scalar fields: The Large N limit*, Phys. Rev. **D55** (1997) R4516–R4520, [astro-ph/9612202].

[151] D. N. Spergel, N. Turok, W. H. Press, and B. S. Ryden, *Global texture as the origin of large scale structure: numerical simulations of evolution*, Phys. Rev. **D43** (1991) 1038–1046.

[152] R. Durrer, M. Kunz, C. Lineweaver, and M. Sakellariadou, *Cosmic microwave background anisotropies from scaling seeds: Fit to observational data*, Phys. Rev. Lett. **79** (1997) 5198–5201, [astro-ph/9706215].

[153] J. Garcia-Bellido, R. Durrer, E. Fenu, D. G. Figueroa, and M. Kunz, *The local B-polarization of the CMB: a very sensitive probe of cosmic defects*, Phys. Lett. **B695** (2011) 26–29, [arXiv:1003.0299].

[154] D. G. Figueroa, M. Hindmarsh, and J. Urrestilla, *Exact Scale-Invariant Background of Gravitational Waves from Cosmic Defects*, Phys. Rev. Lett. **110** (2013), no. 10 101302, [arXiv:1212.5458].

[155] M. Bartelmann and P. Schneider, *Weak gravitational lensing*, Phys. Rept. **340** (2001) 291–472, [astro-ph/9912508].

[156] A. Lewis and A. Challinor, *Weak gravitational lensing of the cmb*, Phys. Rept. **429** (2006) 1–65, [astro-ph/0601594].

[157] A. Stebbins, *Weak lensing on the celestial sphere*, astro-ph/9609149.

[158] C. M. Hirata and U. Seljak, *Reconstruction of lensing from the cosmic microwave background polarization*, Phys. Rev. **D68** (2003) 083002, [astro-ph/0306354].

[159] D. Yamauchi, T. Namikawa, and A. Taruya, *Full-sky formulae for weak lensing power spectra from total angular momentum method*, JCAP **1308** (2013) 051, [arXiv:1305.3348].

[160] **Planck** Collaboration, P. A. R. Ade et al., *Planck 2015 results. XV. Gravitational lensing*, arXiv:1502.0159.

[161] M. Kilbinger et al., *CFHTLenS: Combined probe cosmological model comparison using 2D weak gravitational lensing*, Mon. Not. Roy. Astron. Soc. **430** (2013) 2200–2220, [arXiv:1212.3338].

[162] J. Benjamin et al., *CFHTLenS tomographic weak lensing: Quantifying accurate redshift distributions*, Mon. Not. Roy. Astron. Soc. **431** (2013) 1547, [arXiv:1212.3327].

[163] F. Simpson et al., *CFHTLenS: Testing the Laws of Gravity with Tomographic Weak Lensing and Redshift Space Distortions*, Mon. Not. Roy. Astron. Soc. **429** (2013) 2249, [arXiv:1212.3339].

[164] **DES** Collaboration, T. Abbott et al., *Cosmology from cosmic shear with Dark Energy Survey Science Verification data*, Phys. Rev. **D94** (2016), no. 2 022001, [arXiv:1507.0555].

[165] **DES** Collaboration, M. R. Becker et al., *Cosmic shear measurements with Dark Energy Survey Science Verification data*, Phys. Rev. **D94** (2016), no. 2 022002, [arXiv:1507.0559].

[166] C. Li and A. Cooray, *Weak Lensing of the Cosmic Microwave Background by Foreground Gravitational Waves*, Phys. Rev. **D74** (2006) 023521, [astro-ph/0604179].

[167] S. Dodelson, E. Rozo, and A. Stebbins, *Primordial gravity waves and weak lensing*, Phys. Rev. Lett. **91** (2003) 021301, [astro-ph/0301177].

[168] D. Sarkar, P. Serra, A. Cooray, K. Ichiki, and D. Baumann, *Cosmic shear from scalar-induced gravitational waves*, Phys. Rev. **D77** (2008) 103515, [arXiv:0803.1490].

[169] S. Saga, D. Yamauchi, and K. Ichiki, *Weak lensing induced by second-order vector mode*, Phys. Rev. **D92** (2015), no. 6 063533, [arXiv:1505.0277].

[170] S. Saga, *Observable cosmological vector mode in the dark ages*, arXiv:1607.0397.

[171] A. Cooray, M. Kamionkowski, and R. R. Caldwell, *Cosmic shear of the microwave background: The Curl diagnostic*, Phys. Rev. **D71** (2005) 123527, [astro-ph/0503002].

[172] T. Namikawa, D. Yamauchi, and A. Taruya, *Full-sky lensing reconstruction of gradient and curl modes from CMB maps*, JCAP **1201** (2012) 007, [arXiv:1110.1718].

[173] S. Seitz, P. Schneider, and J. Ehlers, *Light propagation in arbitrary space-times and the gravitational lens approximation*, Class. Quant. Grav. **11** (1994) 2345–2374, [astro-ph/9403056].

[174] HSC collaboration, *Hyper Suprime-Cam Design Review*, .

[175] M. L. Brown et al., *Weak gravitational lensing with the Square Kilometre Array*, PoS **AASKA14** (2015) 023, [arXiv:1501.0382].

[176] LSST Science Collaboration, P. A. Abell, J. Allison, S. F. Anderson, J. R. Andrew, J. R. P. Angel, L. Armus, D. Arnett, S. J. Asztalos, T. S. Axelrod, and et al., *LSST Science Book, Version 2.0*, ArXiv e-prints (Dec., 2009) [arXiv:0912.0201].

[177] G. Bernstein and M. Jarvis, *Shapes and shears, stars and smears: optimal measurements for weak lensing*, Astron.J. **123** (2002) 583–618, [astro-ph/0107431].

[178] J. Magueijo, A. Albrecht, P. Ferreira, and D. Coulson, *The Structure of Doppler peaks induced by active perturbations*, Phys. Rev. **D54** (1996) 3727–3744, [astro-ph/9605047].

[179] R. Durrer and M. Sakellariadou, *Microwave background anisotropies from scaling seed perturbations*, Phys. Rev. **D56** (1997) 4480–4493, [astro-ph/9702028].

[180] M. A. Amin and D. Grin, *Probing early-universe phase transitions with CMB spectral distortions*, Phys. Rev. **D90** (2014), no. 8 083529, [arXiv:1405.1039].

[181] J. C. Mather, E. S. Cheng, D. A. Cottingham, R. E. Eplee, Jr., D. J. Fixsen, T. Hewagama, R. B. Isaacman, K. A. Jensen, S. S. Meyer, P. D. Noerdlinger, S. M. Read, L. P. Rosen, R. A. Shafer, E. L. Wright, C. L. Bennett, N. W. Boggess, M. G. Hauser, T. Kelsall, S. H. Moseley, Jr., R. F. Silverberg, G. F. Smoot, R. Weiss, and D. T. Wilkinson, *Measurement of the cosmic microwave background spectrum by the COBE FIRAS instrument*, apj **420** (Jan., 1994) 439–444.